©Copyright 2020
Elliot L Claveau

Axial Evolution of a Sheared-Flow-Stabilized Z Pinch

Elliot L Claveau

A dissertation
submitted in partial fulfillment of the
requirements for the degree of

Doctor of Philosophy

University of Washington

2020

Reading Committee:

Uri Shumlak, Chair

Brian A Nelson

Justin M Little

Program Authorized to Offer Degree:
Aeronautics and Astronautics

University of Washington

Abstract

Axial Evolution of a Sheared-Flow-Stabilized Z Pinch

Elliot L Claveau

Chair of the Supervisory Committee:
Professor Uri Shumlak
Aeronautics and Astronautics

The Fusion Z-pinch Experiment (FuZE) is a sheared-flow-stabilized Z pinch based on the ZaP and ZaP-HD experiments. The FuZE device generates neutron-producing, 50-cm-long Z pinches formed from plasma accelerated through coaxial electrodes. The Z pinches are sustained between a nose cone at the tip of the plasma gun and an end wall at the end of the assembly region flux conserver. The end wall geometry is modified from a central hole to a spoked design and it is found that plasma exhaust is limited, but can be increased by increasing the ratio of ram and thermal pressures to the magnetic field pressure. The limited plasma exhaust results in a stagnation wave in the assembly region, increasing the plasma axial current and changing the shear flow profiles from a hollow to a peaked velocity distribution. The instantaneous neutron scaling with pinch current is investigated and it is found that the scaling corresponds to an adiabatic pinch where linear density increases with axial current. Lastly, the termination of plasma acceleration is found to be triggered by a blow-by instability starting at the insulator located at the breech end of the coaxial accelerator.

TABLE OF CONTENTS

LIST OF FIGURES

ACKNOWLEDGMENTS

This work would not have been possible without the guidance, trust, and patience of Professor Uri Shumlak. I would also like to acknowledge the key role that my colleagues played in keeping me sane and in challenging me to become a better scientist. Thank you also to my community in Seattle and in Québec for the support and understanding along this long journey. I would like to acknowledge the support received from the Natural Sciences and Engineering Research Council of Canada (NSERC).

Chapter 1

INTRODUCTION

In the middle of the twentieth century, nuclear fusion power plants were believed to be within arm's reach. The plasma equilibrium provided by Z pinches promised to offer confinement and scaling with a configuration attainable through simple engineering [1]. A current passing through a plasma located between two electrodes compresses the plasma to temperatures and densities where atoms fuses. Above a temperature and density threshold, the nuclear fusion reactions generate more energy than it is required to drive the current, therefore creating a power plant which the only waste is in the form of stable helium and the required fuel is abundantly available in the ocean, as deuterium, and soil, as lithium.

However, it was found experimentally [2] and theoretically [3] that this simple configuration is unstable; any perturbation breaks down the plasma in a matter of nanoseconds. Z pinches were then abandoned to the profit of more stable equilibria involving externally applied magnetic fields. One of these configurations, the tokamak, is now the main avenue for fusion research, in part motivated by early encouraging results [4]. Today, ITER is the largest nuclear fusion project and is planned to start operation in 2025, with deuterium-tritium operation starting in 2035. ITER will be demonstrating the production of net fusion gain for the first time using a tokamak. However, the project is presently estimated to have a final cost in the excess of 20 billion dollars. A less expensive configuration is needed to make the cost and timeline of nuclear fusion attainable.

In 1995, Shumlak & Hartman [5] proved that it was possible to stabilize Z pinches using sheared flow. Then, through the ZaP experiment [6], stability was observed and correlated with the presence of sheared flow. The idea of using a Z pinch as a nuclear fusion reactor became possible again and the Fusion Z-pinch Experiment (FuZE) was designed.

The Z pinch relies on a radial equilibrium provided by the $J \times B$ force. Contrary to a static Z pinch, the sheared-flow-stabilized Z pinch has a large axial velocity. The pinch lifetime is also longer than the flow through times. Previous studies on ZaP [7] and ZaP-HD [8] showed sheared flow profiles changing over time. This velocity profile evolution could be influenced by the presence of an end wall. The consequence of this axial evolution could influence the yield of a Z pinch as the linear density increases. Previous studies [9] also showed the different acceleration mechanisms fundamental to the Z-pinch sustainment. The events taking place in the coaxial accelerator eventually reach the Z pinch, influencing its plasma parameters and stability.

This dissertation is divided as follows: in Chap. 2, plasma exhaust is shown to be limited through the end wall. This leads to the formation of a stagnation wave described in Chap. 3. Then, neutron scaling with pinch current is investigated in Chap. 4 and it is shown to be consistent with an adiabatic scaling with increased linear density. Lastly, Chap. 5 shows how the axial acceleration of plasma is terminated by a blow-by event triggered by the depletion of the neutral gas supply.

All of these findings are helping pave the way to designing a net-gain fusion reactor core based on the sheared-flow-stabilized Z pinch [10], which would enable relatively inexpensive, compact, and modular nuclear fusion-based power plants.

1.1 Z-pinch equilibrium

Z pinches present several advantages compared with confinement methods relying on applied magnetic fields. For example, thanks to the absence of magnetic field coils, there is no limit to the intensity of the magnetic field, as opposed to configurations that require external superconducting coils. This characteristic allows for a straightforward scaling related to the current flowing in the pinch. This section describes this scaling and issues related to its stability.

1.1.1 Bennett relation

The Z-pinch equilibrium is derived from the magnetohydrodynamic (MHD) force balance. This model assumes that the particles are distributed according to a Maxwellian distribution, that the plasma is globally charge neutral and that the electrons respond immediately to any perturbation. The MHD momentum equation is

$$\rho\left(\frac{\partial}{\partial t}+\boldsymbol{v}\cdot\nabla\right)\boldsymbol{v}=\boldsymbol{J}\times\boldsymbol{B}-\nabla p, \tag{1.1}$$

where ρ is the mass density, $\boldsymbol{v}$ is the fluid velocity, $\boldsymbol{J}$ is the current density, $\boldsymbol{B}$ is the magnetic field, and p is the plasma pressure. In a Z pinch, the current is purely axial, that is, only in the $\hat{z}$ direction. Ampère's law applied to a purely axial current will generate a purely azimuthal magnetic field, as shown in the following equations

$$\nabla\times\boldsymbol{B}=\mu_0\boldsymbol{J} \tag{1.2}$$

$$-\frac{1}{r}\frac{d\left(rB_\theta\right)}{dr}=\mu_0 J_z \tag{1.3}$$

where μ_0 is the vacuum permeability. The azimuthal direction is identified by the subscript θ and the axial direction by z. Using Eq. (1.3) and assuming a steady state plasma without any radial velocity, Eq. (1.1) becomes

$$\frac{dp}{dr}=-\frac{B_\theta}{\mu_0 r}\frac{d\left(rB_\theta\right)}{dr} \tag{1.4}$$

Rearranging the terms leads to a force balance form,

$$\frac{d}{dr}\left(p(r)+\frac{B_\theta^2(r)}{2\mu_0}\right)+\frac{B_\theta^2(r)}{\mu_0 r}=0 \tag{1.5}$$

where the plasma pressure p is balanced by the term associated with the magnetic field pressure $\frac{B_\theta^2(r)}{2\mu_0}$ and the magnetic tension force $\frac{B_\theta^2(r)}{\mu_0 r}$ arising from the curvature of the field around the axis. For a quasi-neutral plasma, $n_e=Zn_i$ where Z is the ionization state, the pressure is defined as

$$p=n_i k_B T_i+n_e k_B T_e=n_i k_B\left(T_i(r)+ZT_e\right) \tag{1.6}$$

where T_i and T_e are the ion and electron temperature, respectively. A linear ion number density is defined as

$$N_i = \int_0^a \int_0^{2\pi} n_i r d\theta dr \tag{1.7}$$

where a is the pinch radius and where the density is assumed to fall to zero beyond that radius. Assuming that $T = T_e = T_i$, the average temperature $\langle T \rangle$ is defined as

$$\langle T \rangle = \frac{1}{\pi a^2} \int_0^a \int_0^{2\pi} T r d\theta dr \tag{1.8}$$

Integrating the force balance relation, Eq. (1.5), over the plasma volume and using Eq. (1.6), Eq. (1.7) and Eq. (1.8), the Bennett relation for Z pinches is obtained. [11].

$$(1 + Z) N_i k_B \langle T \rangle = \frac{\mu_0 I^2}{8\pi} \tag{1.9}$$

1.1.2 Scaling relations

Manipulating Eq. (1.9), the scaling relations between the temperature, density, and current are obtained. The subscripts 1 and 2 refer to two different states of the same plasma.

$$\frac{T_2}{T_1} = \left(\frac{I_2}{I_1}\right)^2 \frac{N_1}{N_2}. \tag{1.10}$$

If no heat is exchanged between the system and its surroundings, the adiabatic approximation can be used [7],

$$\frac{d}{dt}\left(\frac{p}{n^\gamma}\right) = 0 \tag{1.11}$$

where γ is the ratio of specific heat. Based on this approximation, two additional scaling relations are derived using Eqs. (1.9) and (1.11),

$$0 = \frac{d}{dt}\left(\frac{(1 + Z)\, kT}{n^{\gamma - 1}}\right). \tag{1.12}$$

This last equation relates density with temperature. Using Eq. (1.10), an equation relating density and current is derived.

$$\frac{n_2}{n_1} = \left(\frac{T_2}{T_1}\right)^{\frac{1}{\gamma-1}} = \left(\frac{I_2}{I_1}\right)^{\frac{2}{\gamma-1}} \left(\frac{N_1}{N_2}\right)^{\frac{1}{\gamma-1}} \tag{1.13}$$

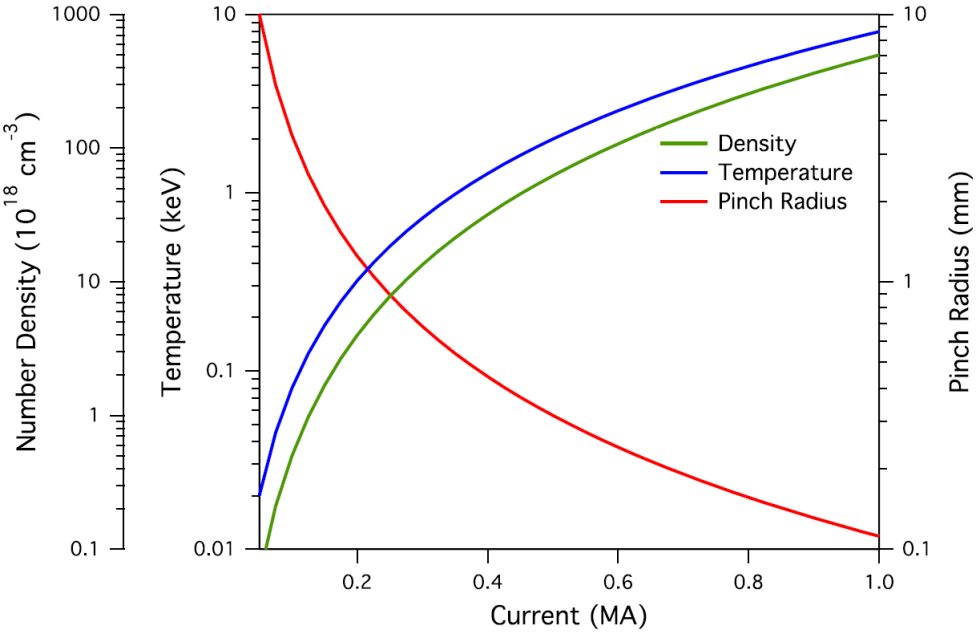

Figure 1.1: Adiabatic scaling of density, temperature and radius of a 50 kA, 20 eV and 10 mm Z pinch [8].

Lastly, a relation is obtained by assuming that all the plasma is contained within the pinch radius a and that it is uniformly distributed. Using Eq. (1.9) with $N = n\pi a^2$ and substituting the temperature and density with Eq. (1.10) and Eq. (1.13) respectively

$$\frac{a_2}{a_1} = \left(\frac{I_1}{I_2}\right)^{\frac{1}{\gamma-1}} \left(\frac{N_2}{N_1}\right)^{\frac{\gamma}{2(\gamma-1)}} \tag{1.14}$$

With a constant number of particles per unit length, that is, $N_1 = N_2$, the temperature, density, and radius depend solely on pinch current. Eqs. (1.10), (1.13), (1.14) are illustrated in Fig. 1.1 for a 50 kA, 20 eV and 10 mm radius Z pinch.

1.1.3 Sheared flow stabilization

The scaling of temperature and density with current is very attractive for a confinement concept. However, static Z pinches are MHD unstable. The first two instability modes are

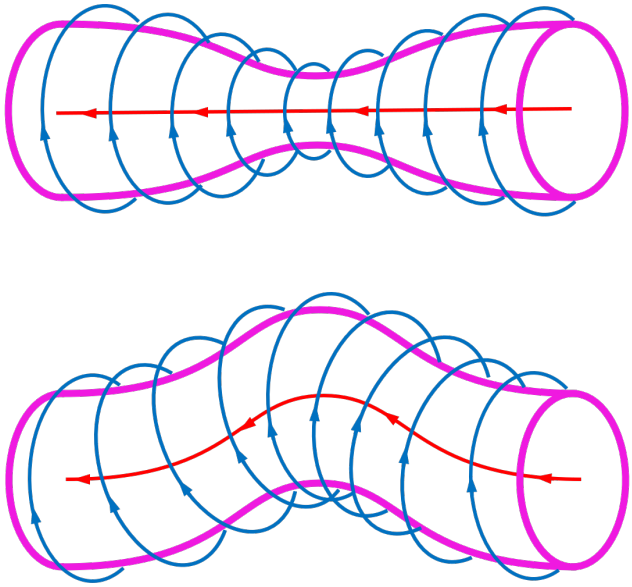

Figure 1.2: Schematic of the sausage (m=0) and kink (m=1) instabilities present in a pure Z pinch. The magnetic field is represented by the blue azimuthal arrows while the pinch current is represented by the red axial arrows.

illustrated in Fig. 1.2. From the energy principle [12] applied to the MHD equations, the $m = 0$ "sausage" mode can be stabilized using a gradual enough pressure gradient

$$-\frac{d\ln p}{d\ln r} \leq \frac{4\gamma}{2+\gamma\beta} \tag{1.15}$$

where $\beta = 2\mu_0 p/B^2$. However, no possible pressure profile can stabilize the m=1 mode in a pure Z pinch. That is, a static Z pinch is always "kink" unstable. It is possible to use sheared flow profiles to stabilize Z pinches [5]. An axial flow does not influence radial force balance and all the Z-pinch scaling relations are still valid. The ideal MHD equations are linearized and the differential equations for radial displacement are numerically solved. It is then found that the Z pinch can be stable, even when a conducting wall is infinitely far, if a minimum shear threshold is exceeded,

$$\frac{dv_z}{dr} \geq 0.1kV_A, \tag{1.16}$$

where k is the axial wave number and V_A is the Alfvén speed, $V_A = B_\theta/\sqrt{\mu_0 \rho}$. The present way to create sheared flow in a Z pinch is linked to coaxial accelerators, which are reviewed in the next section.

1.2 Previous work on coaxial accelerators

A coaxial plasma accelerator (or plasma gun) is a device that uses two concentric cylinders to accelerate plasma via the Lorentz force. A voltage is applied between the cylinders, resulting in a radial current, therefore accelerating the plasma into the downstream section. Plasma accelerators have a variety of applications; the principle is used for astrophysical jet formation in laboratory settings [13] as well as the formation of spheromaks [14]. The concept was first introduced by J. Marshall [15] as a way to accelerate plasma in a stable manner [16]. This section focuses on results related to shaped plasma accelerator, plasma foci and magnetoplasmadynamic thrusters which use the coaxial electrode configuration. These concepts have been studied extensively and their geometry and working principle are similar to the present machine, thus motivating their studies.

1.2.1 Shaped plasma accelerators

Shaped coaxial accelerators are characterized by a chamber that is initially evacuated. Gas or plasma is injected at the breech end of the accelerator and is accelerated by the $J \times B$ force. Investigation on shaped electrode has been conducted by Morozov [17] and, more recently, the HyperV team [18]. It was shown that the geometry plays a key role in the radial uniformity of acceleration and in preventing the blow-by instability. Moreover, Morozov developed models explaining the impact of shaping on the current attachment dynamics.

1.2.2 Plasma focus

Plasma focus machines were independently developed by Mather [19] in the United States and Filippov [20] in the Soviet Union. Mather type foci are characterized by a long acceleration

region and a low aspect ratio while Filippov type foci are characterized by a short acceleration region and a high aspect ratio. In both cases, the chamber is initially filled with gas at several Torrs of pressure.

Plasma focus devices are optimized for neutron production. The production of neutrons has been found to scale with $\propto I^4$ [21], I being the discharge current. The mechanism for neutron production is linked to the necking of the column due to the m=0 mode. The interruption of the plasma column induces a large electric field which in turn accelerates ions. This mechanism has been found to be strongly dependent on kinetic effects and cannot be fully resolved using MHD theory [22]. Moreover, there is a strong dependence on the polarity of the inner electrode. Specifically, the neutron yield is much higher when the inner electrode is positively charged with respect to the outer electrode. In general, plasma focus devices have a sharp transition from the inner electrode to the assembly region. A hollow inner electrode is also used. It has been found, across multiple geometries and order of magnitudes of energies, that a drive parameter S stays constant for neutron optimized devices [23]. This drive parameter is defined by

$$S = \frac{I_p}{a\sqrt{\rho}} \tag{1.17}$$

where I_p is the peak discharge current, a is the anode radius and ρ is the ambient gas density.

Experiments using different inner electrode shapes have been performed. A tapered and a hemispherical inner electrode were compared with a flat one and optimized for soft X-ray production [24]. It was found that the soft X-ray emission was optimized for the flat profile. The results from the hemispherical and tapered geometry lead to similar yield. It was theorized that the final diameter was the leading parameter for soft X-ray production. Moreover, the shaped (hemispherical, tapered) electrode led to more hard X-ray production, mainly coming from the anode surface.

Zakaullah et al. [25] observed a strong effect of the anode shape on the performance of their low power plasma focus. They found that the tapered electrode lead to the highest X-ray emission. These X-rays were coming principally from the tip of the anode.

Bhuyan et al. [26] compared a hollow, hemispherical and solid anode. It was found that the hemispherical electrode produced the greatest X-ray energy. However, the energy was concentrated on the electrode surface while the X-rays from the hollow and flat electrode were coming from the pinch.

1.2.3 Magnetoplasmadynamic thrusters

Magnetoplasmadynamic (MPD) thrusters use a coaxial design to accelerate plasma in steady state. They have an increased efficiency with increased power and are therefore studied for application in the 100 kW range [27]. Studies related to MPD thrusters are aiming to optimize the different variables for maximum thrust.

An MPD thruster can have an externally applied axial magnetic field. Thrusters without any applied magnetic fields are referred as "self-field thrusters".

Numerical simulation using 2D MHD codes have been performed on various MPD geometries [28–31]. The length of the inner electrode and the shape of the outer electrode have been shown to significantly impact the current distribution in the accelerator region. Moreover, the results were also shown to be closely affected by the assumption taken on the resistivity model and the neutral gas interactions. The model for collisions can also have an important impact on the accuracy of the simulation. The current distribution is important as it dictates the magnitude and direction of the force in the accelerator.

1.3 The ZaP, ZaP-HD and FuZE experiments

The Fusion Z-pinch Experiment, FuZE, is similar to the ZaP and ZaP-HD machines. The results of these predecessor experiments are first described. Cross sections of the different experiments are illustrated in Fig. 1.4. Then, the design of FuZE is described.

1.3.1 ZaP and ZaP-HD

In 2001, evidence of stabilization of the Z pinch was found and sheared flow was measured through spectroscopy [6]. The presence of sheared flow was correlated with the presence of

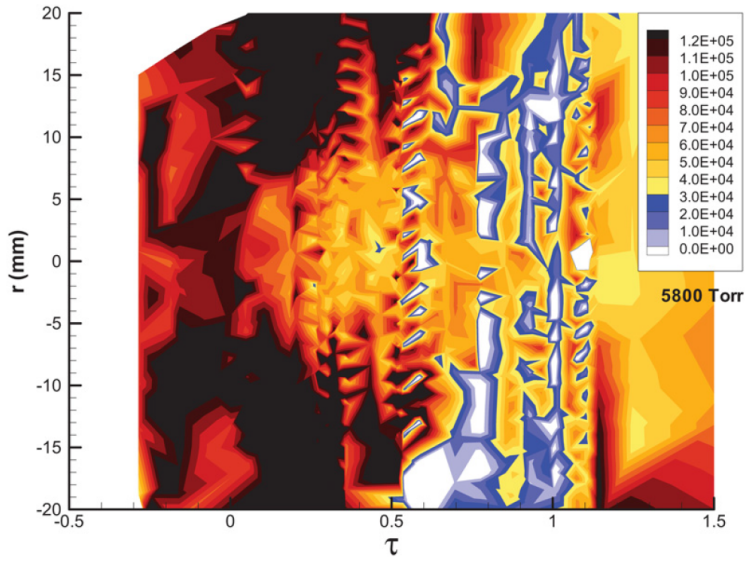

Figure 1.3: Velocity at different radii and different times in the pinch evolution from [32]. Sheared flow is present between $\tau = 0$ and $\tau = 1$. $\tau = 0$ and $\tau = 1$ correspond to the first and last time where stability is observed in the magnetic field data.

a stable Z pinch. Measurements of sheared flow compared to measurements of stability is illustrated in Fig. 1.3. ZaP operated with a total plasma current of up to 480 kA, a pinch radius of 1 cm, a density $n_e = 2 \times 10^{16}$ cm^{-3} and a temperature $T_e = 75$ eV.

ZaP-HD aimed to increase ZaP parameters by introducing a third electrode. The cross section of the machine is illustrated in the middle of Fig. 1.4. This electrode would isolate the acceleration phase and the compression phase, therefore attaining higher current in the pinch. A pinch radius of 0.3 cm, density of 2×10^{17} cm^{-3}, and peak temperature of $T_e = 1$ keV were achieved [8]. However, this geometry led to arcing across the middle (red) and outer (blue) electrode, which limited the machine performance.

1.3.2 FuZE design and operation

The FuZE machine uses the same electrode diameters and acceleration region length as ZaP. The gas valves are also located at the same azimuthal and axial locations. It uses the

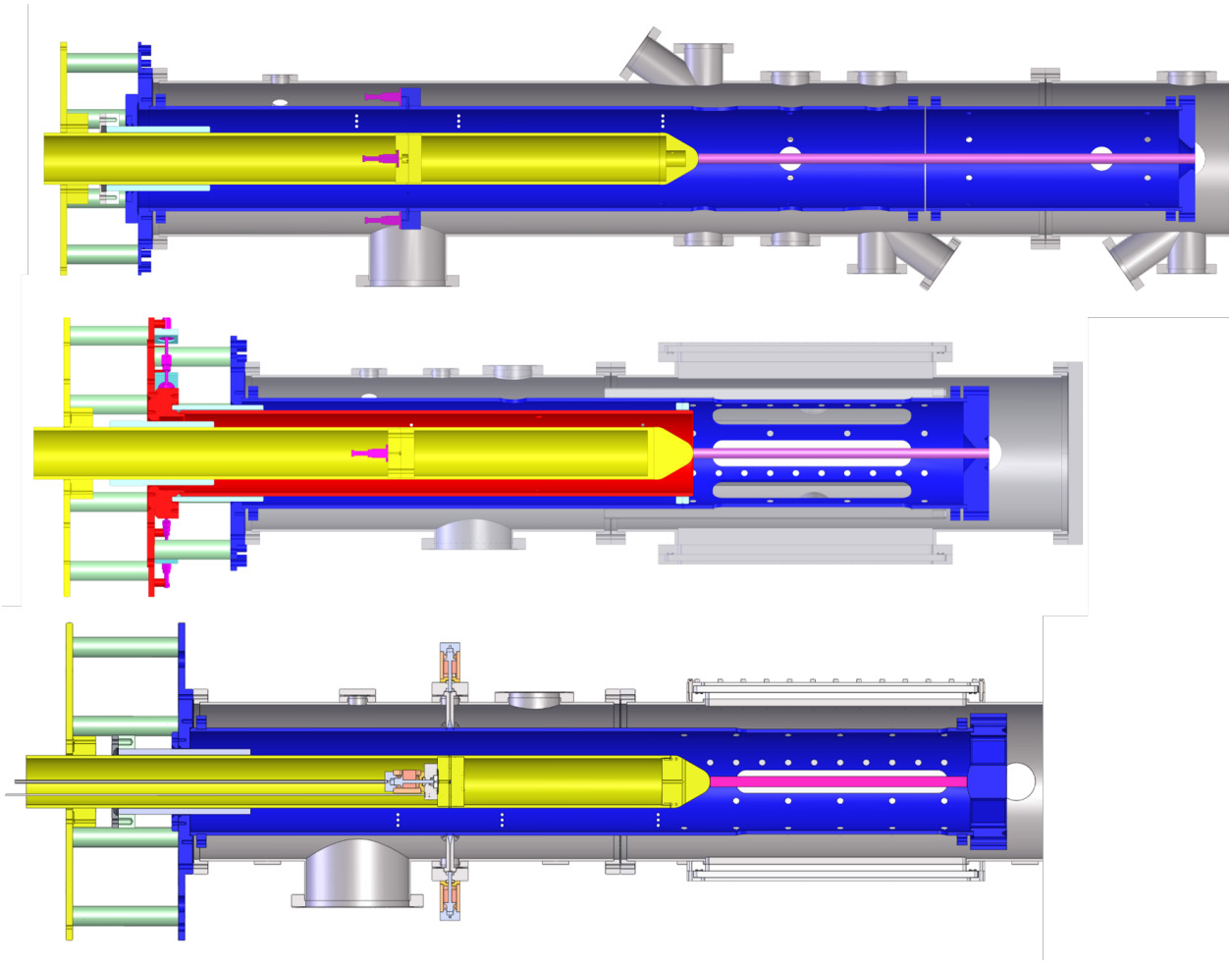

Figure 1.4: ZaP (top), ZaP-HD (middle) and FuZE (bottom). The outer electrode is represented in blue and the inner electrode is represented in yellow. In ZaP-HD, the middle electrode is identified in red.

same assembly region geometry, that is the same pinch length, as ZaP-HD. Fig. 1.5 shows a schematic of the FuZE experiment with the main components identified. The geometry of the end wall and the nose cone was changed. The results from these experimental campaigns are shown in Chap. 2 and Appx. B.

The addition of a surge tank to the FuZE experiment enables the formation of a new plasma pulse approximately every 3 minutes. The surge tank lowers the peak chamber pressure seen by the pump after each plasma pulse, enabling the turbopump to run continuously connected to the chamber. This high repetition rate makes it possible to collect large data sets and, for example, reduce the pulse to pulse variation effects from the analysis.

While the geometry of FuZE is similar to ZaP, the former's power supply is much more capable. FuZE uses 12 independently controlled 830 µF capacitors connected to thyristor switches, capable of charging to 8 kV for a total bank energy of 320 kJ compared to the 100 kJ of ZaP. FuZE also uses faster gas valves capable of injecting more neutral gas inside the coaxial accelerator.

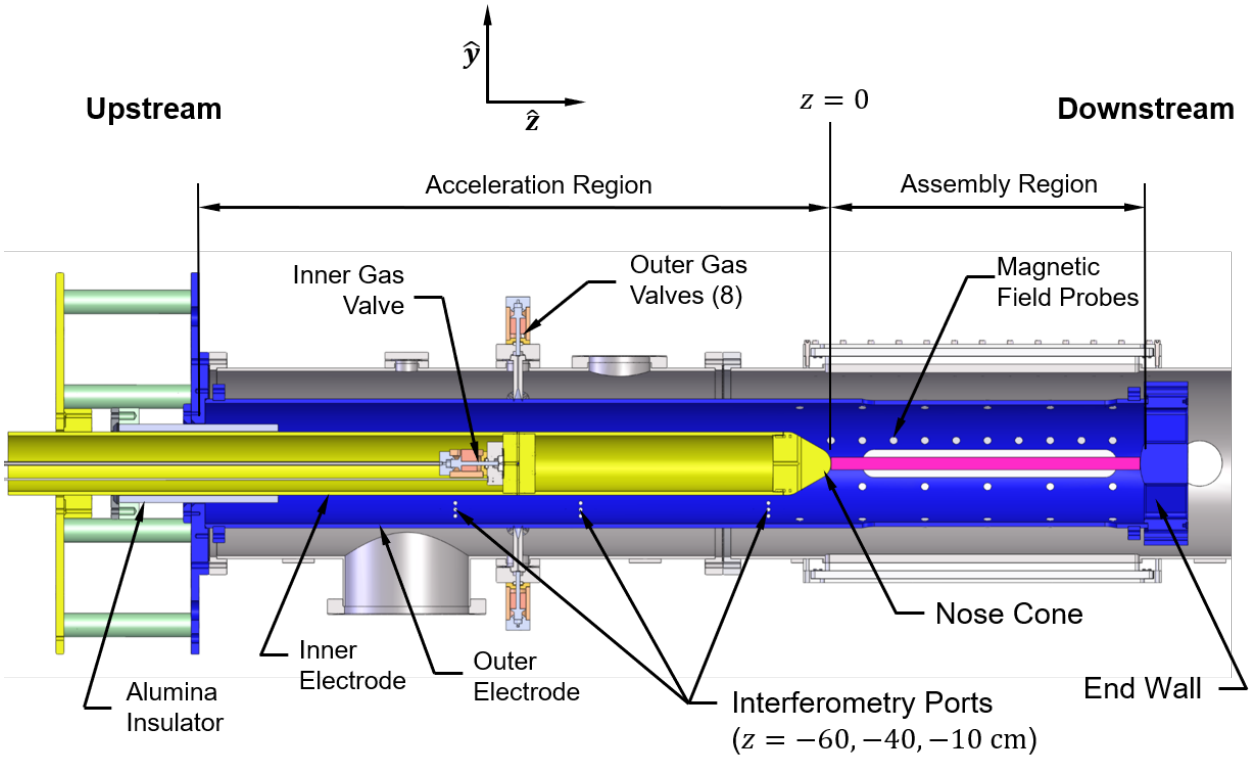

Figure 1.5: Section view of the FuZE machine identifying the main machine components and regions. The plasma is accelerated from the coaxial accelerator (upstream) to the assembly region (downstream) toward the end wall.

1.4 Diagnostics

This section describes the main diagnostics used for the results presented in this thesis. In particular, the magnetic field, temperature and velocity measurements and analysis methods are shown. The aforementioned diagnostics are used in a way specific to the FuZE experiment and are not described elsewhere. An overview of density, visible light emission, and neutron detector measurements is also provided.

1.4.1 Magnetic mode data

Plasma stability is quantified using magnetic field probe data. Azimuthal probe signals are decomposed into Fourier components where the data is assumed to be

$$B_\theta(\theta) = \sum_{j=0,m} a_j \cos(j\theta) + \sum_{j=1,m} b_j \sin(j\theta). \tag{1.18}$$

A simplification of the magnetic field is obtained using only the first two terms of the Fourier series

$$B_\theta(\theta) = a_0 + a_1 \cos(\theta) + b_1 \sin(\theta), \tag{1.19}$$

$$m_0 = a_0, \tag{1.20}$$

$$m_1 = \sqrt{a_1^2 + b_1^2}, \tag{1.21}$$

$$\phi = \arctan(b_1, a_1), \tag{1.22}$$

where m_0 is the average magnetic field computed at one axial location, m_1 is the centroid of the magnetic field at that location, and ϕ is the phase angle of the centroid. This is directly related to the magnitude and position of the current through Ampère's law. A useful metric is the normalized m_1 data, defined by

$$m_{1,norm} = \frac{m_1}{m_0}. \tag{1.23}$$

The value of the normalized m_1 quantify how far the current is off axis. A continuous period of normalized m_1 value below a threshold of 0.2 is called a quiescent period.

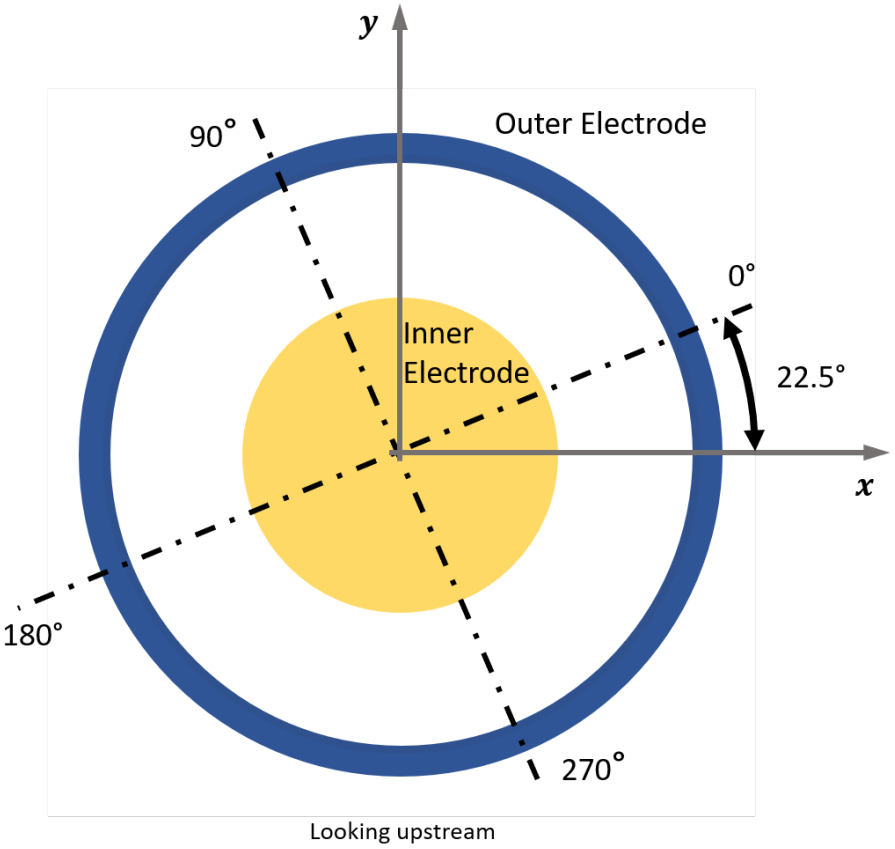

Figure 1.6: Coordinate system of the FuZE machine looking upstream. The magnetic field probes "0°" is actually positioned 22.5° from the horizontal xz plane.

The current centroid displacement is related to the normalized mode data by [9]

$$\Delta r = \frac{R_w}{2}\frac{m_1}{m_0} \tag{1.24}$$

where R_w is the radius of the outer electrode. The radial displacement together with the phase angle ϕ fully locates the current centroid in the Z pinch. The coordinate system of the experiment is shown in Fig. 1.6.

Throughout this document, the axial current is used instead of the azimuthal magnetic field. The two are related by Ampère's law by

$$I_z = \frac{\mu_0 B_\theta}{2\pi R_w}. \tag{1.25}$$

The magnetic field is measured at 94 locations in FuZE. Two linear arrays of probes placed every 5 cm are located from $z = -95$ cm to $z = 45$ cm, where $z = 0$ cm marks the location of the tip of the nose cone. Additionally, azimuthal arrays of 8 probes are located every 10 cm between $z = -5$ cm and $z = 45$ cm. The location of the probes is shown in Fig. 1.7.

In order to simultaneously look at the time resolved and spatially resolved axial current information obtained from the magnetic field probes, contour maps are created. An example contour map is shown in Fig. 1.8.

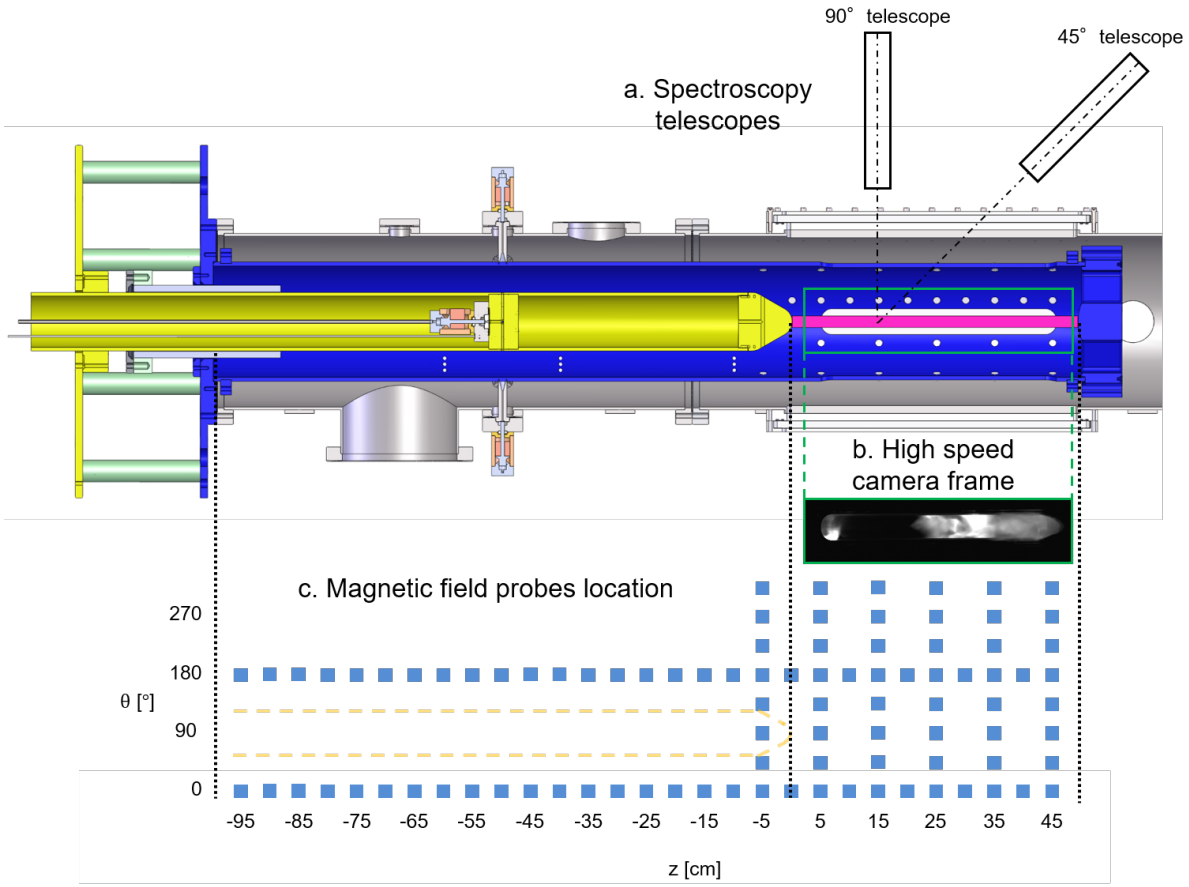

Figure 1.7: (a) Location of the 90° and 45° telescopes both imaging the $z = 15$ cm location. The telescopes can be translated to record data from other axial locations. (b) Frame from the Kirana 05M Ultra-Fast Framing Camera showing visible light emission from the assembly region. The outline of the outer electrode diagnostics access slot is visible. (c) Location of the 94 magnetic field probes (blue squares).

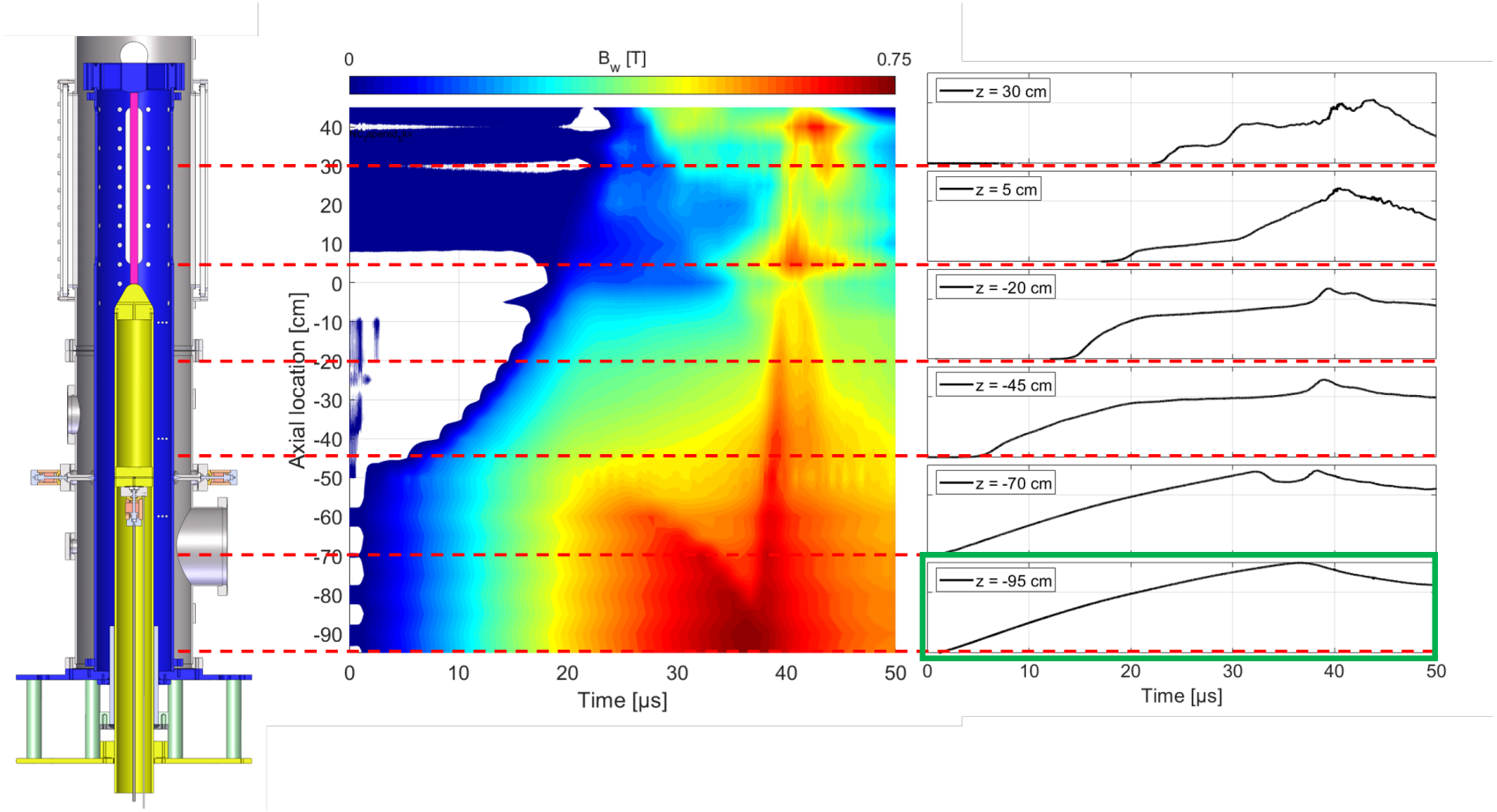

Figure 1.8: Magnetic contour map (center) with the machine to scale (left) and selected magnetic field traces (right) corresponding to the axial locations indicated by the red dashed lines. The trace in the green box is used to normalize every axial location to generate the contour map seen in Fig. 2.6.

1.4.2 Velocity and temperature measurements

Light emission is recorded by a spectrometer through 20 fiber-optic chords. 10 chords are connected through a telescope oriented 90 degrees from the Z-pinch axis and 10 chords are recorded through a telescope oriented 45 degrees from the axis, pointed upstream at the chamber. Each bundle of 10 chords spans a total to 3.76 cm. The telescopes are schematically shown in Fig. 1.7.

The main lines used for Doppler spectroscopy are the carbon III and carbon V lines as they normally appear far from other lines, helping with interpreting the data. The plasma ion temperature is obtained from the Doppler broadening of the CIII and CV emission lines [33]. The temperature is calculated from

$$T_i = \sqrt{\frac{m_i c^2 \left(\Delta\lambda_D\right)^2}{8 \ln 2 \lambda_0^2 e}} \tag{1.26}$$

where m_i is the ion mass, c is the speed of light, e is the elementary charge, λ_0 is the nominal wavelength of the ion at temperature T_i, where the temperature is given in eV. $\Delta\lambda_D$ is the full width half max of the fitted emission after accounting for the instrument function with

$$\Delta\lambda_D = \sqrt{\left(\Delta\lambda_{FWHM}\right)^2 - \left(\Delta\lambda_A\right)^2} \tag{1.27}$$

where $\Delta\lambda_A$ is the spectrometer instrument function and $\Delta\lambda_{FWHM}$ is the full width half max of raw the emission.

Pressure broadening is assumed to be negligible compared to the Doppler effect. A previous study [34] looked into fitting the emission profiles with Lorentzian profiles. A similar analysis could be carried out on the FuZE data. However, the advantage of the method could be limited on FuZE by the low signal-to-noise ratio of some pulses and the plasma parameters that are in a region where the stark effect is negligible compared to the Doppler effect.

The plasma ion axial velocity is also obtained by measuring the Doppler shift of the center wavelength with

$$v_{i,z} = c \left(\frac{\lambda_F}{\lambda_0} - 1\right) \frac{1}{\cos\left(\pi/4\right)} \tag{1.28}$$

The center wavelength of the Gaussian fit is indicated by λ_F. The $1/\cos(\pi/4)$ factor is specific to the measurement of axial velocity from an oblique telescope angled at 45°.

The measurement process is indicated in Fig. 1.9. First, the intensified Charge Coupled Device (ICCD) image is binned into 20 separate chords, each corresponding to one optical fiber chord. The light intensity is summed and averaged within each bin. Fig. 1.9 shows the process for chord 13. A fitting routine finds the best Gaussian to the profile associated with the CIII (229.7 nm) line. For the CV lines (227.1 nm, 227.7 nm, and 227.8 nm), a sum of three Gaussians is used for the fitting routine using

$$a_1 e^{-((x-\lambda_F)/w)^2} + a_2 e^{-((x-\lambda_F-0.634)/w)^2} + a_3 e^{-((x-\lambda_F-0.701)/w)^2} \tag{1.29}$$

where the factors a are the amplitude of each Gaussian and the parameter w is related to the full width half max (FWHM) by

$$\Delta\lambda_{FWHM} = 2\sqrt{\ln 2}w \tag{1.30}$$

1.4.3 Density measurements

Time resolved line integrated density is obtained using an eight chord, heterodyne, quadrature, helium-neon (He-Ne) interferometer [35]. The chords are positioned to measure the density in the accelerator as well as in the assembly region. At the later stages of the experimental campaign, the quality of the assembly region windows degraded, and it was no longer possible to obtain usable density traces in that region. The interferometer system is also susceptible to electromagnetic noise and the signal sometimes degrade throughout the course of one pulse.

1.4.4 Light emission

Figure 1.7 shows visible light emission frames taken from a Kirana 05M Ultra-Fast Framing Camera at 500,000 frames per second. In a pure hydrogen plasma, the H-alpha line (656 nm) dominates the light intensity in the visible range. It is therefore possible that most of the

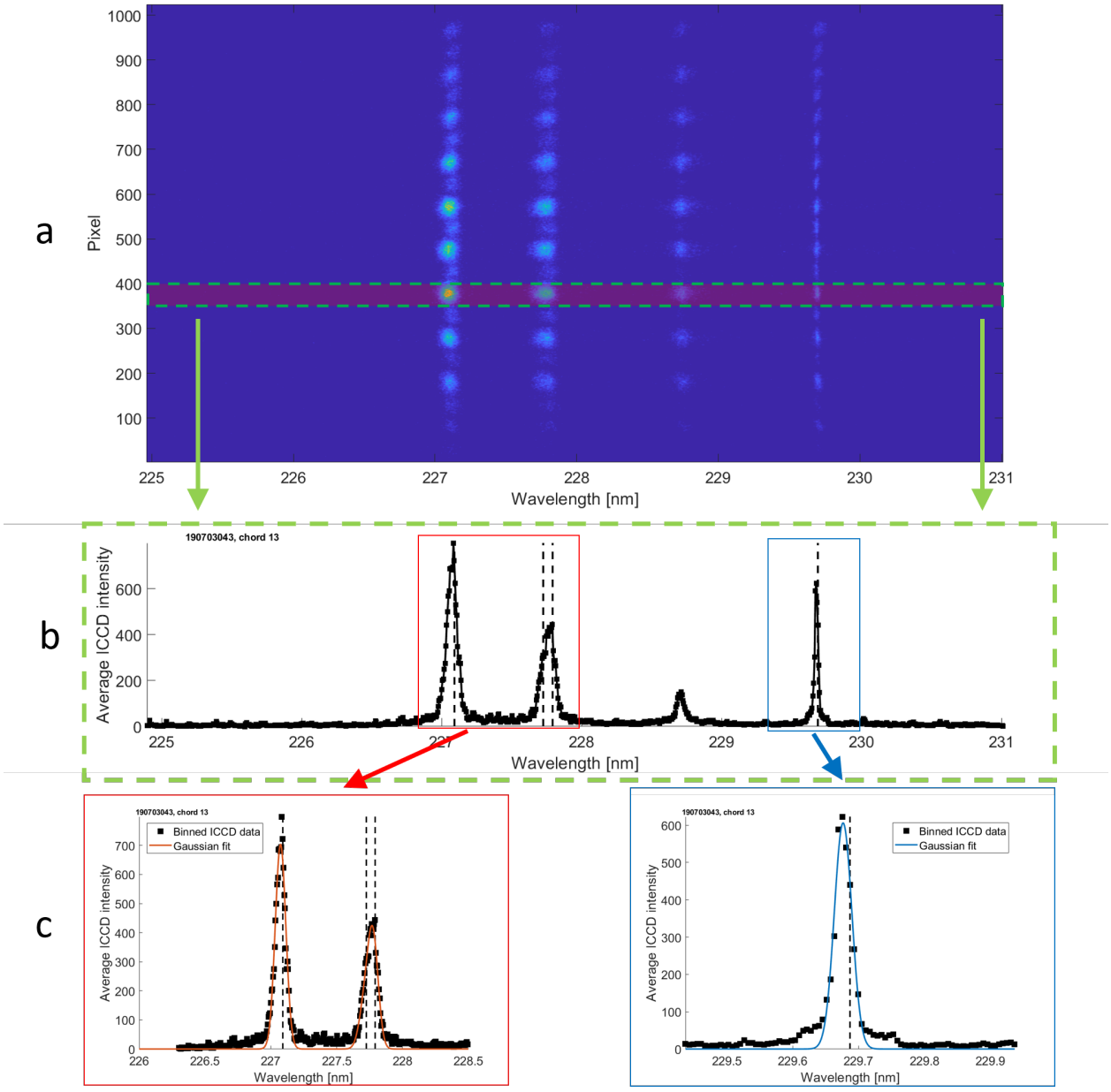

Figure 1.9: Fitting process to obtain plasma ion temperature and ion velocity from Doppler broadening and Doppler shift. The image recorded on the spectrometer ICCD (a) is divided into 20 chords. Each chord is binned over a fixed pixel width (b). (c) The CV triplet (red) is fitted with three Gaussians according to Eq. (1.29) and the CIII line (blue) is fitted to one Gaussian.

light emitted comes from plasma outside the Z-pinch core, where the temperature is low enough to allow the hydrogen recombination events to take place.

1.4.5 Neutron measurements

Neutrons are measured through plastic scintillator detectors using a pulse counting method. These detectors provide temporal resolution and can provide spatial resolution of the neutron flux if multiple detectors are used. Details of the diagnostic implementation on FuZE are found in [36].

Chapter 2

PLASMA EXHAUST IN A SHEARED-FLOW-STABILIZED Z PINCH

Plasmas relevant to nuclear fusion and space propulsion can be described by the ideal magnetohydrodynamics (MHD) equations which predict that plasma is frozen into the magnetic flux [37]. In space propulsion, thrust is only achieved if plasma escapes the source. However, magnetic fields tied to external electrodes can prevent plasma exhaust as the plasma follows the divergence-free field.

In order for a plasma to escape a magnetic field, non-ideal MHD processes must exist in the system. First, plasma resistivity can be sufficiently high to allow diffusion of magnetic field to take place on a fast enough time scale [38]. Second, plasma can demagnetize if the Larmor radius becomes sufficiently large compared to the scale length of the system [39, 40]. These two phenomena are studied extensively in the context of magnetic nozzle research. Third, flux can escape if the magnetic field reconnects outside of the flux-conserving region [41]. However, for all the aforementioned effects to take place, a plasma trapped within a flux-conserving region has to first break free of the confining forces.

This chapter focuses on how plasma exhaust can be achieved by changing the ratio of plasma ram and thermal pressures to magnetic pressure at the partially open boundary of a flux conserver. Specifically, plasma properties from multiple pulses are analyzed from FuZE to assess how the flux conserver boundary geometry affects the plasma exhaust.

The flux conserver boundary is provided by the outer electrode end wall located 50 cm downstream of the end of the coaxial acceleration region, illustrated in Fig. 2.1. The end wall provides a fixed return current path from the outer electrode, trapping the magnetic flux in the pinch assembly region. For plasma to escape the flux conserver region, it has to first

overcome the magnetic forces at the end wall, and subsequently detach from the magnetic field, or the magnetic field has to escape.

This chapter analyzes the Z-pinch current and plasma density measured from two different end wall geometries: a "central hole" end wall and a "spoked" end wall. The end wall is shown to affect the plasma current when the device is operated at high bank energy and high gas injection. The plasma magnetic Reynolds number is high enough such that ideal MHD should properly describe the plasma dynamic. However, a model shows that increasing the plasma ram and thermal pressures relative to the magnetic pressure leads to exhaust as plasma overcomes the magnetic tension at the end wall spokes. The conditions for which increased plasma exhaust is predicted are satisfied experimentally in the high bank energy conditions.

This chapter first presents the measured plasma current and plasma density in the assembly region and their evolution with the end wall geometry change. Then, the magnetic Reynolds number is calculated. An equilibrium model at the end wall is presented and the results are used to show that the increase in plasma ram and thermal pressures to the magnetic pressure corresponds to an increase in plasma exhaust.

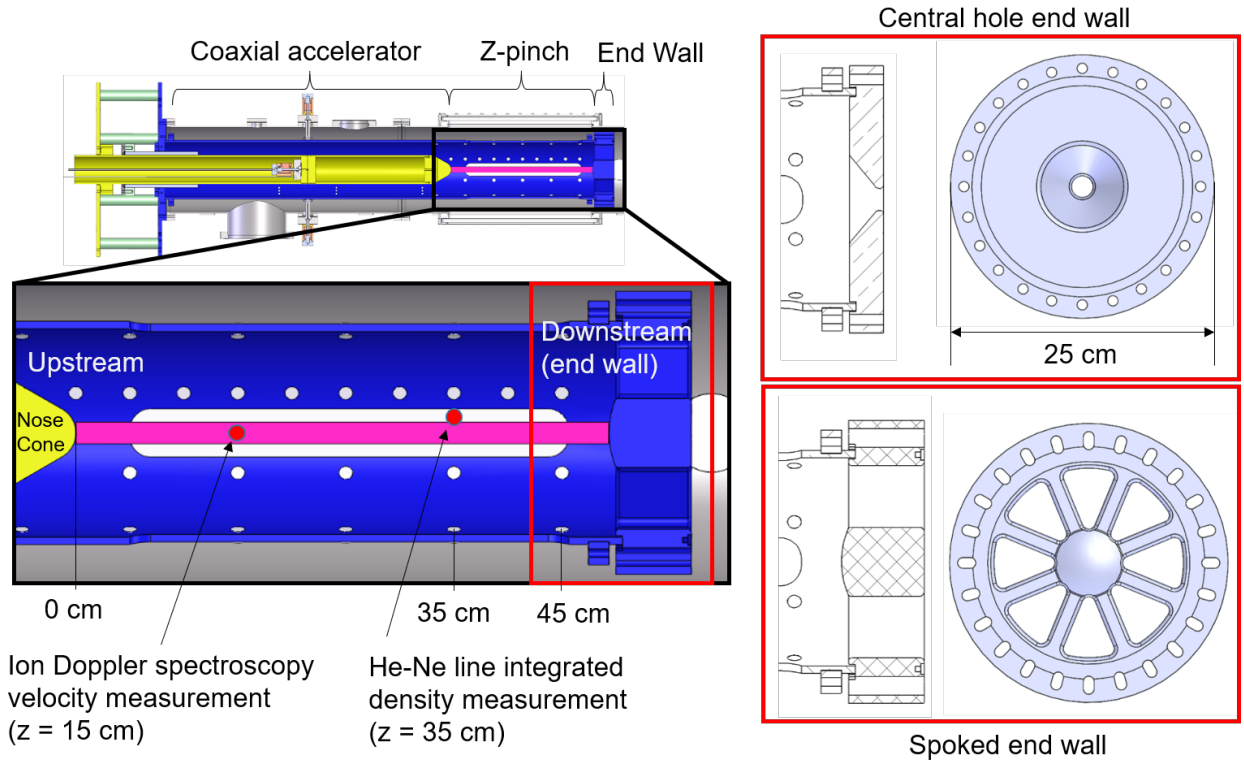

Figure 2.1: Cross section of the FuZE machine. The flux conserver is identified in blue. The main diagnostic locations are identified: the axial velocity measurement computed from ion Doppler spectroscopy located at 15 cm, the electron density measurement from the He-Ne interferometer, located at 35 cm, and the pinch current measurements from the magnetic field probe arrays located at every 5 cm. The two end wall designs are also identified: the central hole end wall and the spoked end wall. The magnetic field probes are embedded in the wall of the flux conserver and are identifiable by the white circles.

2.1 Plasma parameters evolution

This section compares the plasma current and density between end wall designs. The current measurement is the closest plasma diagnostic to the end wall and therefore shows the largest sensitivity to the geometry change. The density is used to compute the plasma ram and thermal pressures while the current is used to compute the magnetic field pressure which are the parameters that determine plasma exhaust, as shown in Sec. 2.2. The location of the different diagnostics are shown in Fig. 2.1.

The central hole end wall has a 2 cm diameter exit located on the axis that opens a total of 1.1% of the end wall area. This design was used on the ZaP and ZaP-HD experiments as well as the initial FuZE experiment. The spoked end wall has 8 openings creating a ratio of end wall open area of 68.1%. The spoked geometry was chosen to maximize the open area while maintaining the structural integrity of the end wall necessary to sustain the electromagnetic forces.

The line-integrated density is measured at 35 cm, 1 cm above the pinch axis. This axial location also has an azimuthal array of magnetic field probes measuring the pinch current. Finally, axial plasma velocity and ion temperature are obtained from ion Doppler spectroscopy at 15 cm.

Two operating conditions are tested. The first operating condition uses a low neutral gas mass through a single gas valve and a low bank energy of 80 kJ, obtained from a 4 kV charge voltage. This will be referred as "Case 1". Current and density data for Case 1 are shown in Fig. 2.2a and Fig. 2.3a respectively. The second operating condition is chosen to be similar to the neutron producing conditions used in Ref. [42]. These conditions use higher neutral gas mass injected through 5 valves and a higher bank energy of 125 kJ, obtained from a charge voltage of 5 kV. This set of pulses will be referred as "Case 2". Current and density data for Case 2 are shown in Fig. 2.2b and Fig. 2.3b respectively. The gas used is a mixture of 95% H_2 and 5% CH_4 by pressure. The CH_4 is added as a diagnostic impurity to produce the CIII and CV lines used for spectroscopic analysis. Between 15 and 20 pulses were taken for

each condition to collect enough data for ion Doppler spectroscopy and to limit effects from pulse to pulse variation. The set of plasma pulses is repeated after changing the end wall. A set of pulses for Case 1 and a set for Case 2 is performed for each end wall configuration, for a total of four sets.

Pinch current is measured at $z = 45$ cm through azimuthal arrays of eight magnetic field probes. Each plot in Fig. 2.2 shows the average current at 45 cm as well as a region encompassing one standard deviation above and below the average value, computed from the plasma pulses produced with the same experimental settings. For Case 2, the current at all axial locations between 0 and 35 cm agree to within one standard deviation for the two end wall configurations. However, the current at 45 cm exhibits a greater change between end wall designs compared to all other axial locations. For Case 1, the current stays within one standard deviation for all axial locations, including at 45 cm. This indicates a change in plasma behavior that results from the end wall geometry in Case 2.

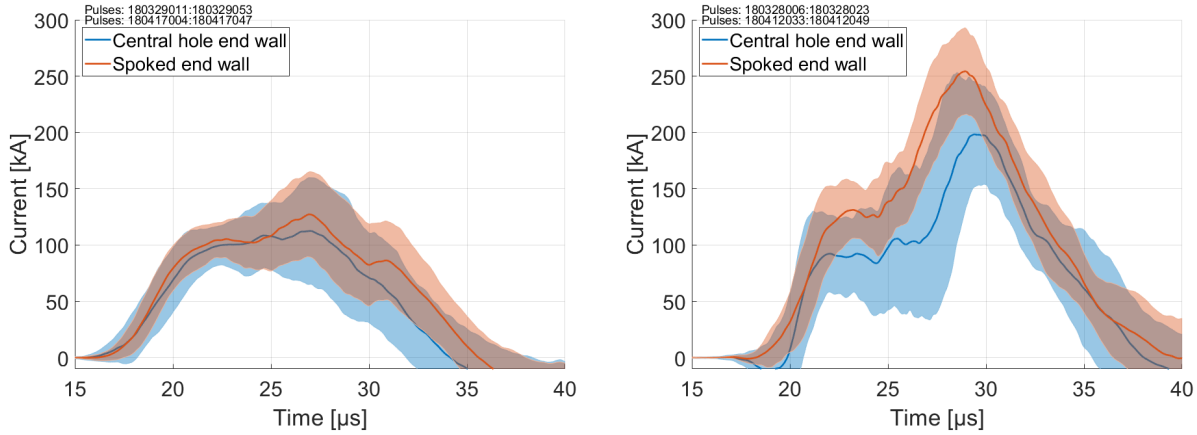

(a) (b)

Figure 2.2: Mean (line) and standard deviation (shaded area) of pinch current at 45 cm for the central hole (blue) and spoked (red) end wall for (a) Case 1 and (b) Case 2. Case 2 deviates by approximately one standard deviation at this axial location between the two end walls while Case 1 exhibits the same behavior as the other axial locations.The pulse-to-pulse variation arises from slight variations in the initial gas injection of each pulse.

Density data are obtained from a He-Ne interferometry system [35]. Figure 2.3 compares

the central hole end wall density signal from all the pulses from Case 1 and all the pulses from Case 2. The location of the line-integrated density measurement is indicated in Fig. 2.1. The average assembly region density is obtained by dividing the line integrated density by the path length of the interferometer chord inside the assembly region. The path length is 19.2 cm. The density is measured at $z = 35$ cm, which is coincident with the eight-probe magnetic field measurement array closest to the end wall with an optically accessible path. The initial density for Case 1 is about 0.5×10^{21} m^{-3} while the initial density for Case 2 is 5.0×10^{21} m^{-3}. The temporal evolution of density is not affected by the end wall change for any of the run conditions.

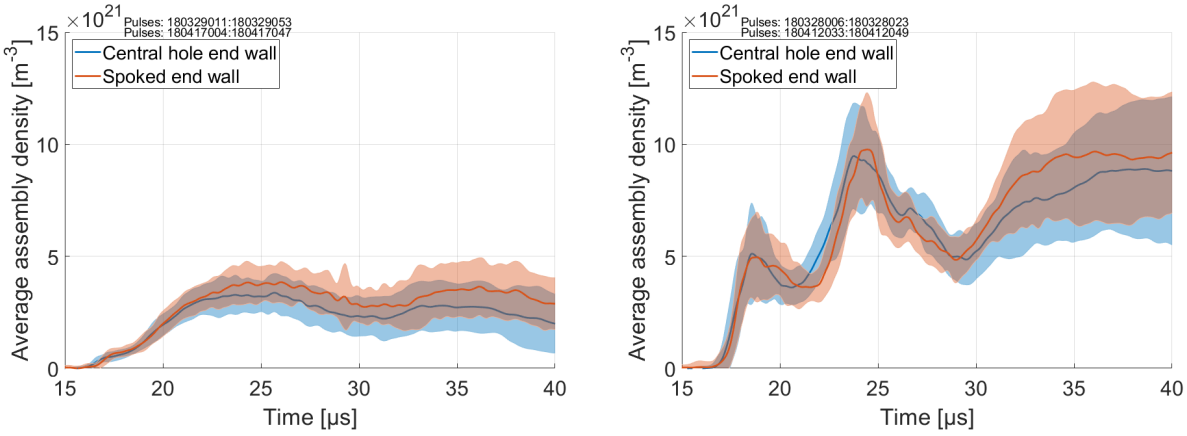

Figure 2.3: Density signal for (a) Case 1 and (b) Case 2, both for the central hole and spoked end walls. Both end walls lead to a similar temporal evolution of density, as illustrated by the overlap of the traces. Case 2 has an initial density that is an order of magnitude greater than Case 1. The pulse-to-pulse variation arises from slight variations in the initial gas injection of each pulse.

Current data were collected downstream of the end wall. A Rogowski coil is embedded in the downstream face of the end wall and measures the current leaving the assembly region through the end wall spokes. Figure 2.4 shows that a signal is only present when current is measured at 45 cm, the most downstream probe array. The Rogowski current is both positive and negative and has a large pulse to pulse variability. Moreover, its magnitude is

approximately 60 times lower than the current just upstream of the end wall.

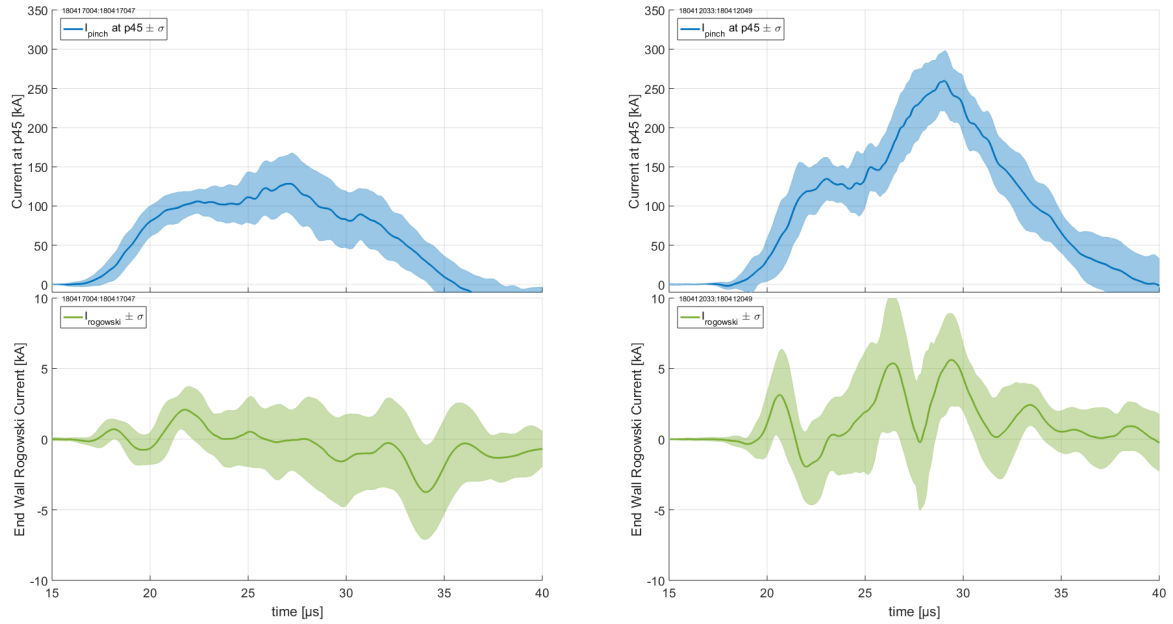

(a) (b)

Figure 2.4: Mean (line) and standard deviation (shaded area) of pinch current at 45 cm for the spoked end wall configuration, and end wall rogowski current (green) for the 4 kV conditions (a) and the 5 kV conditions (b). The current leaving the end wall is ~ 60 times lower than the current just upstream and is highly variable between plasma pulses.

Figure 2.6 shows contours of the Z-pinch current for Case 2 where the region of higher current propagates from the end wall to the acceleration region, in a direction opposite to the plasma flow coming from the coaxial accelerator. The slope of the propagation is steeper for the center hole than for the spoked design downstream of 40 cm, suggesting an effect of the end wall geometry change on the current propagation.

Velocity profiles are recorded at 15 cm through ion Doppler spectroscopy [6, 43] using a telescope angled at 45 degrees with respect to the z axis and measuring CIII impurities emission (229.7 nm). The spectrometer records spectra through 20 chords spanning a total of 3.88 cm perpendicular to the pinch axis. One 0.5 µs exposure is recorded per pulse for the ion Doppler spectroscopy analysis. Velocities and temperatures are averaged across multiple

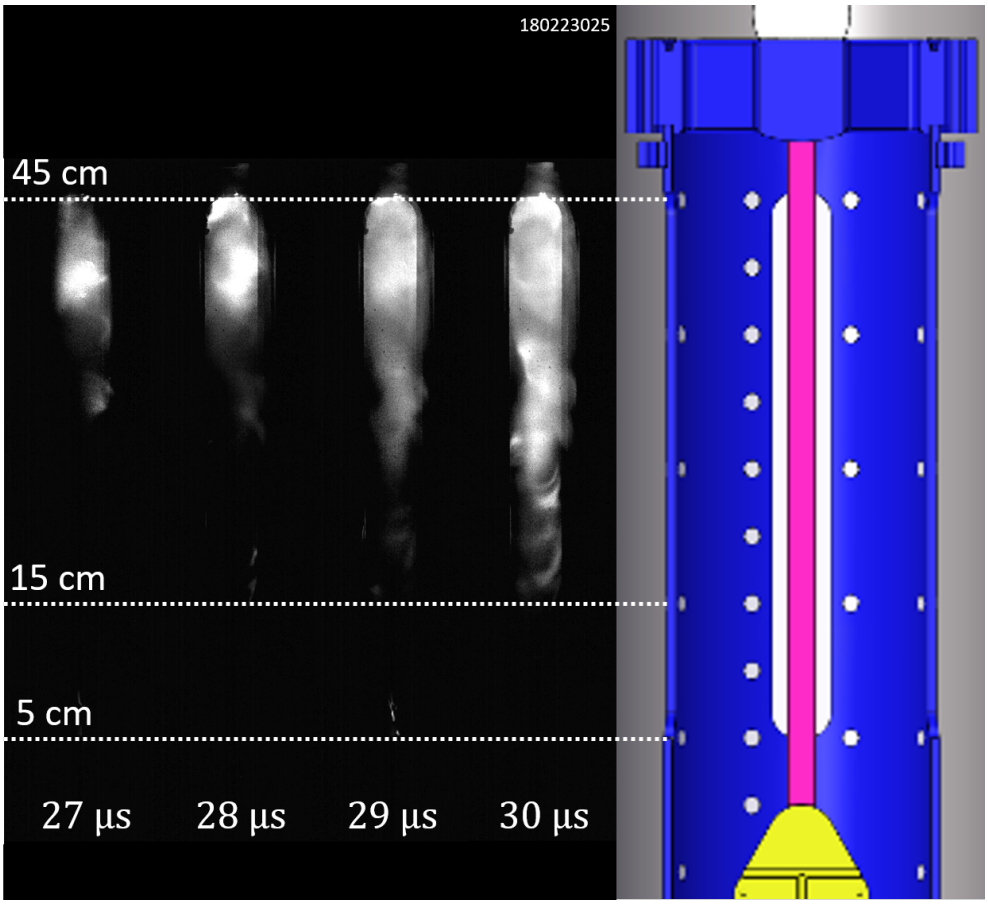

Figure 2.5: Four consecutive frames, separated by 1 µs interval, from a high speed camera showing visible light emission starting at the downstream section of the experiment and propagating toward the accelerator.

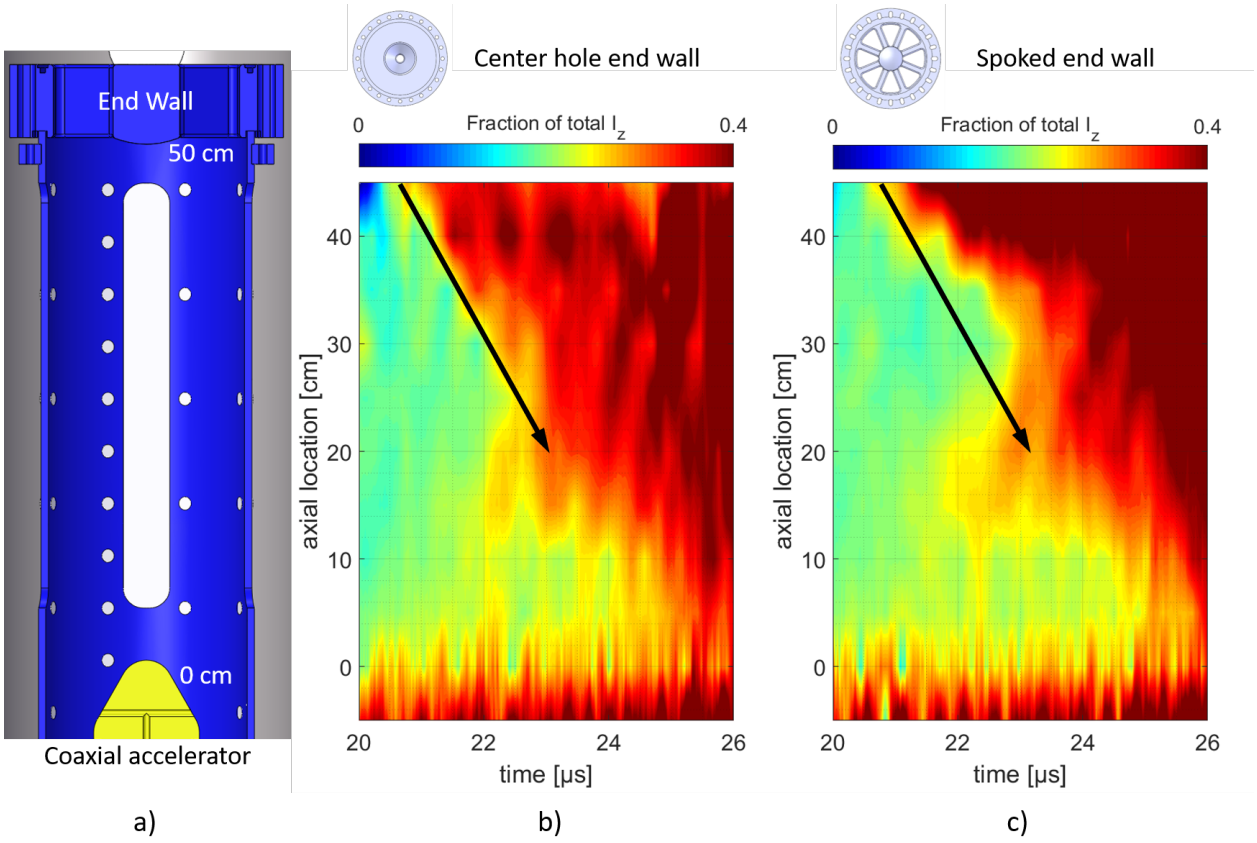

Figure 2.6: (a) Z-pinch assembly region to scale with (b,c) contours between 0% and 40% of the total plasma current at the 5 kV charge voltage throughout the Z-pinch assembly region for (b) the center hole end wall and (c) the spoked end wall. The backward propagating structure is indicated by the arrow and is evident from the high current edge starting at 45 cm and propagating upstream. The slope of the backward propagating wave is steeper for the center hole end wall near 40 cm.

pulses. No significant difference is found between the two end walls for the CIII velocities and temperature. Average velocities of 110 km/s and 140 km/s are calculated using the Doppler shift of the CIII line for Case 1 and Case 2, respectively. An average assembly region temperature of 80 eV is calculated from the Doppler broadening of the CIII lines in both cases.

2.2 Analysis of the end wall equilibrium

In both cases, no change is apparent from the measured properties upstream of 40 cm, including the density signals shown in Fig. 2.3. For Case 1, the current traces stay within a standard deviation across all axial locations between end wall configurations, showing that the geometry change has little effect on the upstream plasma. However, for Case 2, the current traces close to the end wall exhibit a change as illustrated by Fig. 2.2 b.

This section shows that the plasma is linked to the magnetic flux such that it should not escape the assembly region flux conserver under ideal MHD. However, we also show that the equilibrium at the end wall will let plasma escape when the plasma thermal and ram pressures increase relative to the magnetic pressure. Finally, the ratio of ram and thermal pressures to magnetic pressure, β_{ram}, is calculated and we show that it is much greater for Case 2 where an upstream current change is detected compared to Case 1 where the currents remain unchanged.

2.2.1 Frozen in flux condition

The magnetic Reynolds number, Rm, quantifies the relative importance between advective effects and resistive diffusion effects. For a plasma where advection dominates, resistivity can be neglected and ideal MHD applies. In a flux conserver, an ideal MHD plasma is frozen in flux and no particles can escape the region. The magnetic Reynolds number is given by

$$Rm = \frac{\mu_0 v a}{\eta} \tag{2.1}$$

where η is the plasma resistivity, μ_0 is the vacuum permeability, a is the scale length of the system, and v is the characteristic speed. The end wall thickness of 7.6 cm is the distance that the plasma has to travel in order to be outside the volume of the flux conserver and is chosen to be the scale length a. v is chosen to be the plasma velocity, which is approximately 110 km/s for Case 1 and 140 km/s for Case 2.

In SI units, the perpendicular Spitzer resistivity [44] for hydrogen is

$$\eta = 5 \times 10^{-5} \ln\Lambda / T_e^{3/2} \ [\Omega \cdot \mathrm{m}] \tag{2.2}$$

where T_e is the electron temperature in eV and $\ln\Lambda$ is the Coulomb logarithm. The magnitude only depends on the plasma temperature as $\ln\Lambda$ is nearly constant for a large range of densities and temperatures. A value of $\ln\Lambda = 17$ is used for the Coulomb logarithm. The average background plasma temperature in the assembly region will be lower than the peak Z-pinch temperature, which is approximately 1 keV for Case 1 [42]. The lower bound for the plasma temperature is obtained from Doppler broadening of CIII impurities. The CIII impurity wavelength is associated with colder ions [45], characteristic of the background, off-axis, plasma. The resulting range of magnetic Reynolds numbers is shown in Fig. 2.7.

At the lowest estimated temperature, the magnetic Reynolds number is still well above unity, supporting the frozen-in flux condition. The resistivity of the plasma at 20 eV is comparable to the resistivity of the spoked end wall, made of graphite. The resistive diffusion time scale, $\tau = \mu_0 L^2/\eta$, is on the order of 500 μs, much longer than the 40 μs time span of interest shown in the current and density data of Fig. 2.2 and Fig. 2.3. Therefore, we can assume that the magnetic field is frozen to the plasma and that the end wall acts as a perfectly conducting boundary.

The end wall closes the flux conserver, providing the return current path. Consequently, as shown by the previous calculation, no plasma is allowed to escape the assembly region as long as an end wall providing electrical continuity is present, independent of its open area. The frozen in flux condition explains why no large difference is found along most of the Z-pinch length between the two end wall configurations. Both end walls provide equivalent

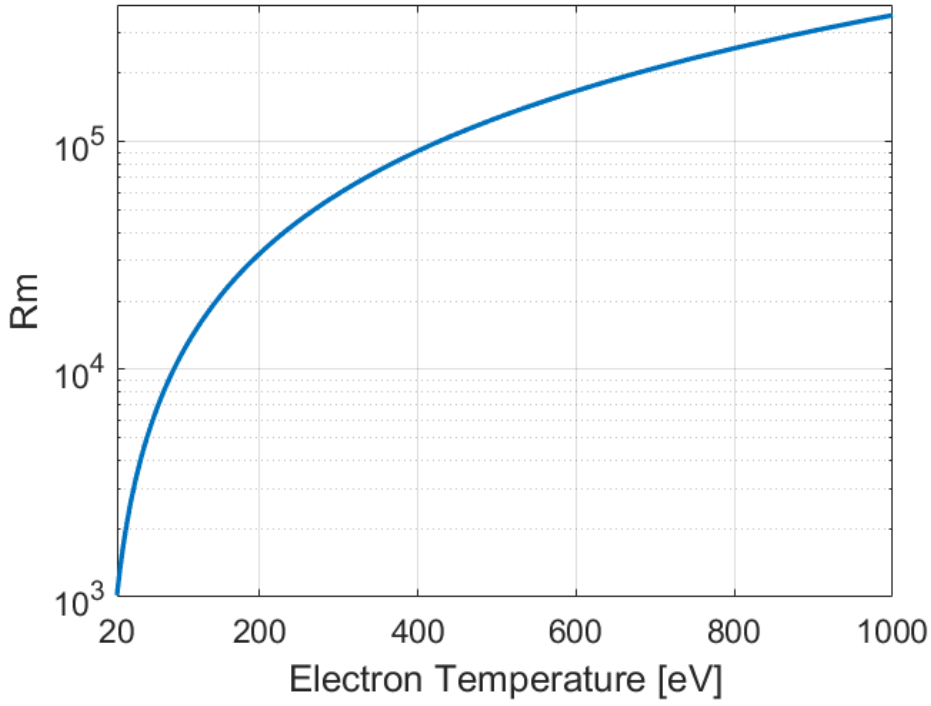

Figure 2.7: Magnetic Reynolds number for a 110 km/s characteristic velocity and a resistivity calculated from temperatures between 20 eV and 1000 eV. The Reynolds number is well above 1 for all calculated resistivity, confirming that the magnetic field behavior is dominated by advection instead of resistive diffusion.

boundary conditions for the magnetic field. However, data taken just upstream of the end wall for Case 2, shown in Fig. 2.2b, suggest an effect from the geometry change. This effect could be due to plasma ram and thermal pressures exceeding the magnetic pressure, leading to plasma exhaust and expansion beyond the end wall where non-ideal MHD effects can take place.

2.2.2 Variable end wall transparency

As shown in the previous section, the plasma and the magnetic flux are linked. The end wall needs to act as a barrier to the plasma flow as well as the return current path, conserving

both the magnetic flux and the plasma. To do so, the plasma must be in force balance at the end wall. The ratio of ram pressure and thermal pressure over the magnetic pressure at the end wall is defined as

$$\beta_{ram} = \frac{\rho_0 v_{z,0}^2 + p_0}{B_0^2/2\mu_0} \tag{2.3}$$

where $\rho_0, v_{z,0}, p_0$ and B_0 are the plasma parameters at the upstream face of the end wall.

The following sections show that more plasma can pass through the spoked end wall as β_{ram} increases. Case 2 has a higher β_{ram} compared to Case 1, leading to an increased transparency which explains the difference in plasma current observed in Fig. 2.2 for Case 2.

Plasma equilibrium model at the spoked end wall

We can represent the spoked end wall as a configuration of purely radial current and a pressure varying along the z axis. The plasma is confined by the end wall spokes, preventing the azimuthal magnetic field from freely expanding. The interaction of the plasma with the end wall spokes is similar to magnetic draping of the solar wind as it interacts with planets [46]. In particular, the orientation of the magnetic field relative to the obstacle is important [47]. The radial end wall spokes are perpendicular to the azimuthal magnetic field, as shown in Fig. 2.8. Using the steady state MHD momentum equation, Ampère's law, and assuming that $\vec{v} = v_z\hat{z}$, we get the following force balance equation.

$$\nabla\left(\rho v_z^2\right) + \nabla p + \nabla\left(\frac{B^2}{2\mu_0}\right) = \frac{1}{\mu_0}\vec{B}\cdot\nabla\vec{B} \tag{2.4}$$

In Eq. (2.4), ρ is the plasma density and v_z is the plasma axial velocity. At the midpoint between two adjacent spokes, the plasma pressure as well as the magnetic pressure gradients are directed to expand the plasma out of the flux conserver while only the magnetic tension holds it in equilibrium. The directions of the forces at the inter-spoke midpoint are indicated in Fig. 2.8. At the midpoint, the terms of the LHS all contribute to the plasma exhaust while only the term on the RHS provides confinement. In this configuration, the confinement is

provided by the magnetic curvature while the outward forces come from the ram pressure, the thermal pressure, and the magnetic field pressure.

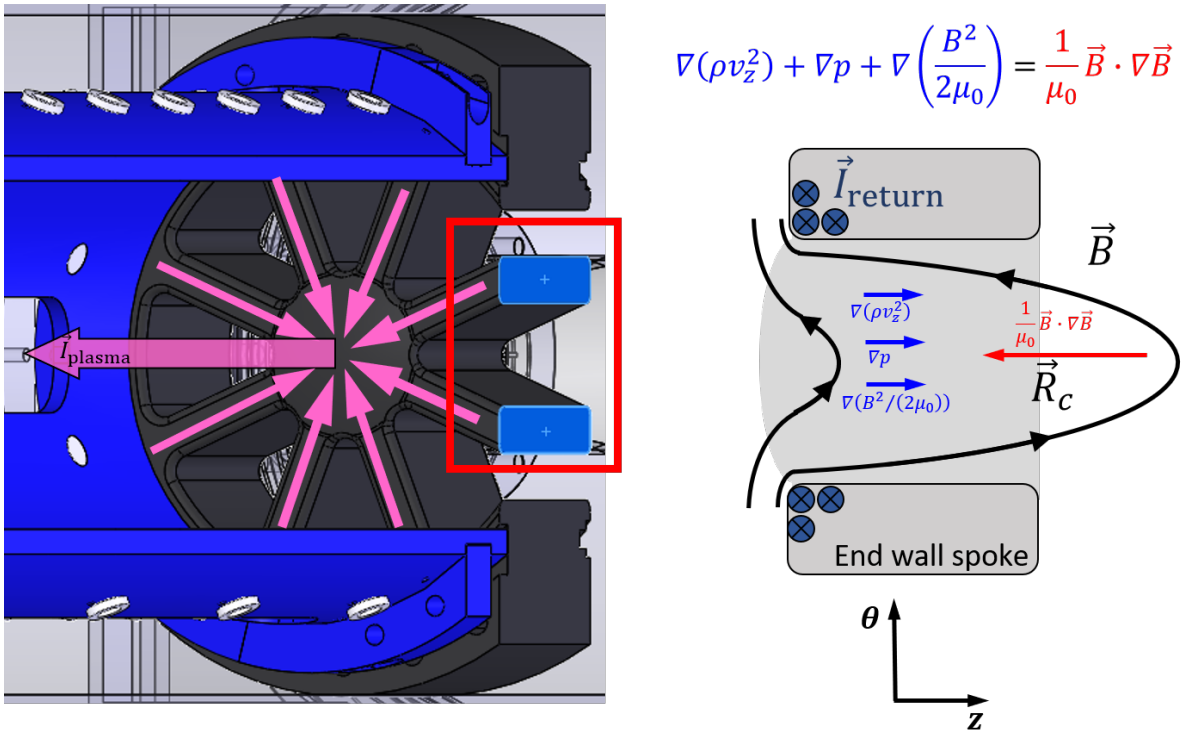

Figure 2.8: Representation of the plasma equilibrium at the midpoint between two adjacent spokes. The magnetic pressure, thermal pressure and ram pressure are balanced by the magnetic tension.

The forces at the spoke mid point are expressed as the following equation

$$\frac{d}{dz}\left(\rho v_z^2 + p\right) + \frac{d}{dz}\left(\frac{B^2}{2\mu_0}\right) = -\frac{B^2}{\mu_0 R} \tag{2.5}$$

where R is the radius of curvature and every parameter varies as a function of the axial distance z. Rearranging Eq. (2.5), we find an expression for the radius of curvature necessary to obtain force balance at the end wall.

$$R(z) = -\frac{B^2/\mu_0}{\frac{d}{dz}\left(\rho v_z^2 + p\right) + \frac{d}{dz}\left(\frac{B^2}{2\mu_0}\right)} \tag{2.6}$$

In a vacuum, the radius of curvature R can expand infinitely, providing a progressively weaker confinement force. A plasma with a small radius of curvature will keep expanding due to the sum of ram, thermal, and magnetic pressures. At the spoked end wall, the conducting spokes act as a barrier through which the magnetic field cannot expand. As such, the radius of curvature between the spokes throughout the end wall depth, EW_{depth}, is limited by the spoke spacing, D_{spoke}. Any small radius of curvature will therefore expand until it reaches the conducting end wall spokes.

From Sec. 2.2.1, the magnetic flux is frozen in the plasma. The magnetic field must decrease with the plasma density and as a consequence, the plasma pressure must reach zero at the same location as the magnetic field pressure. Therefore, the total plasma pressure and the magnetic field pressure are assumed to follow the same profile, that is $\frac{B^2}{2\mu_0} \propto f(z)$ and $\rho v_z^2 + p \propto f(z)$. Equation (2.6) now becomes

$$R(z) = -\frac{2}{\beta_{ram} + 1} \frac{f(z)}{df(z)/dz} \tag{2.7}$$

One particular profile that satisfies Eq. (2.7) is

$$f(z) = \exp\left(\frac{-z}{L}\right) \tag{2.8}$$

where L is the scale length of the profile, determining the e-folding distance. The profile from Eq. (2.8) is chosen because it removes the dependence on axial distance z from the radius R. Equation (2.7) now becomes

$$R = \frac{2L}{\beta_{ram} + 1} \tag{2.9}$$

As β_{ram} increases, the required radius for equilibrium decreases. We can rearrange Eq. (2.9) using the condition that $R \geq D_{spoke}/2$. This radius represents the largest semicircle that can fit between the end wall spokes, as illustrated in Fig. 2.9.

$$L \geq \frac{D_{spoke}\,(\beta_{ram} + 1)}{4} \tag{2.10}$$

Equation (2.10) dictates the smallest possible e-folding distance as a function of β_{ram}. From the spoked end wall geometry, we know that the maximum spoke gap is $D_{spoke} = 4.7$ cm. As the e-folding distance L decreases, more plasma is confined within the end wall thickness. Figure 2.9 shows two plasma profiles with different e-folding distances as well as the corresponding end wall and magnetic field geometries associated with the model.

With Eqs. (2.8) and (2.10) using $z = EW_{depth} = 1.5D_{spoke}$, an end wall transparency is calculated and illustrated in Fig. 2.10 as a function of β_{ram}. The end wall transparency quantifies the ratio of plasma density at the downstream edge over the plasma density at the upstream edge of the end wall. It is the fraction of plasma that escaped the flux conserving region to expand beyond the end wall.

$$\text{transparency} = \exp\left(\frac{-6}{\beta_{ram}+1}\right) \tag{2.11}$$

Figure 2.10 shows that as β_{ram} increases, the fraction of the profile that will be confined reduces. That is, more plasma can exhaust through the end wall. Increasing β_{ram} increases the e-folding distance L necessary for equilibrium, as shown in Eq. (2.10). As the end wall has a finite thickness, a longer e-folding distance L means that a smaller fraction of the profile will be confined through the end wall depth.

Even in the case of a very low value of β_{ram}, plasma is still expected to escape the assembly region as the configuration described by Eq. (2.6) is susceptible to interchange instabilities due to bad curvature at the spoke midpoint.

Observed increase in β_{ram} for Case 2

As shown in the previous section, a larger value of β_{ram} leads to an increase in plasma exhaust. Figure 2.11 compares the value of β_{ram} for the spoked end wall. From Section 2.1, a total temperature of 80 eV is used in both cases and velocities of 110 km/s and 140 km/s are used for Case 1 and Case 2 respectively. The plasma density ρ in Eq. (2.3) is obtained from the density measurements at 35 cm, averaged over the assembly region area, shown in

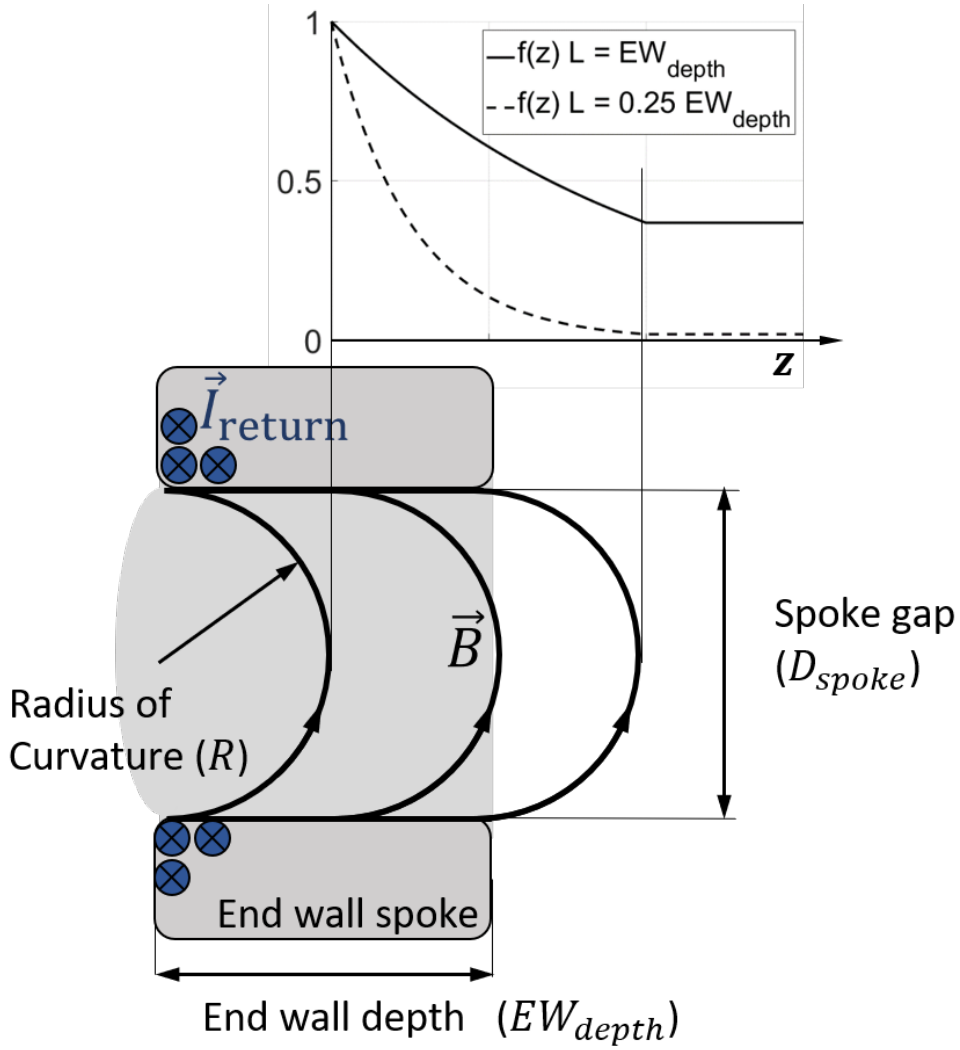

Figure 2.9: Plasma profile described by Eq. (2.8) with representative magnetic field lines through the end wall depth. A profile with a smaller e-folding distance L will confine more plasma through the end wall depth than a profile with a larger e-folding distance. A steeper plasma profile (smaller L) can be held in force balance when β_{ram} is lower.

Fig. 2.3a and 2.3b.

The value of β_{ram} is much larger for Case 2 than for Case 1 before approximately 27 µs. For example, according to Eq. (2.11) and Fig. 2.10, an increase in β_{ram} from approximately $\beta_{ram} = 3$ at 20 µs for Case 1 to $\beta_{ram} = 15$ at 20 µs for Case 2 leads to a 3-fold increase in

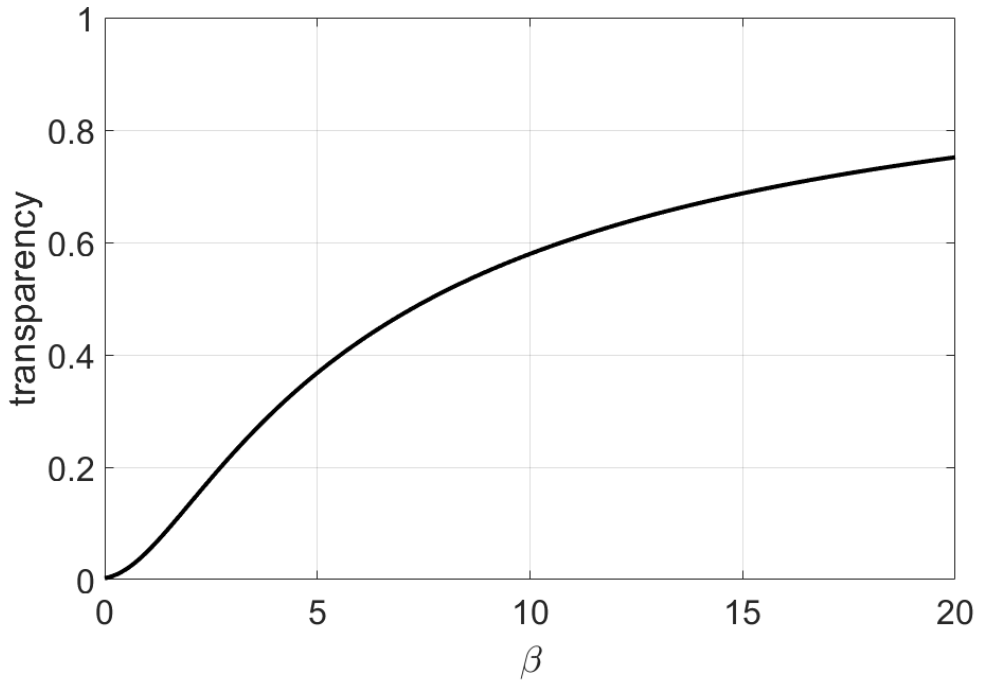

Figure 2.10: End wall transparency as a function of β_{ram}. As β_{ram} increases, less plasma can be confined in the axial extent of the end wall.

end wall transparency.

In Fig. 2.2, the current for Case 2 is different after the end wall change, while the current for Case 1 remains unchanged. The difference between Case 1 and Case 2 is the value of β_{ram}. While the end wall geometry changed in both cases, the increase in pinch current is only observed for Case 2. Both cases share the same end wall geometric parameters, and only the plasma parameters have been changed. In particular, the value of plasma density, axial velocity, and magnetic field are different for Case 2 such that its value of β_{ram} is initially much higher.

Equation (2.11) shows that an increase in β_{ram} should be increasing the plasma exhaust through the spoked end wall. The larger β_{ram} values for Case 2 leads to a larger plasma exhaust as a consequence of Eq. (2.11). Therefore, the observed change in axial current for

Case 2 is linked to the increased plasma exhaust.

Greater compression of the plasma produces higher measured current due to the magnetic field being frozen-in. Plasma compression increases with ram and thermal pressures, therefore increasing the measured current for the operating conditions with higher β_{ram}.

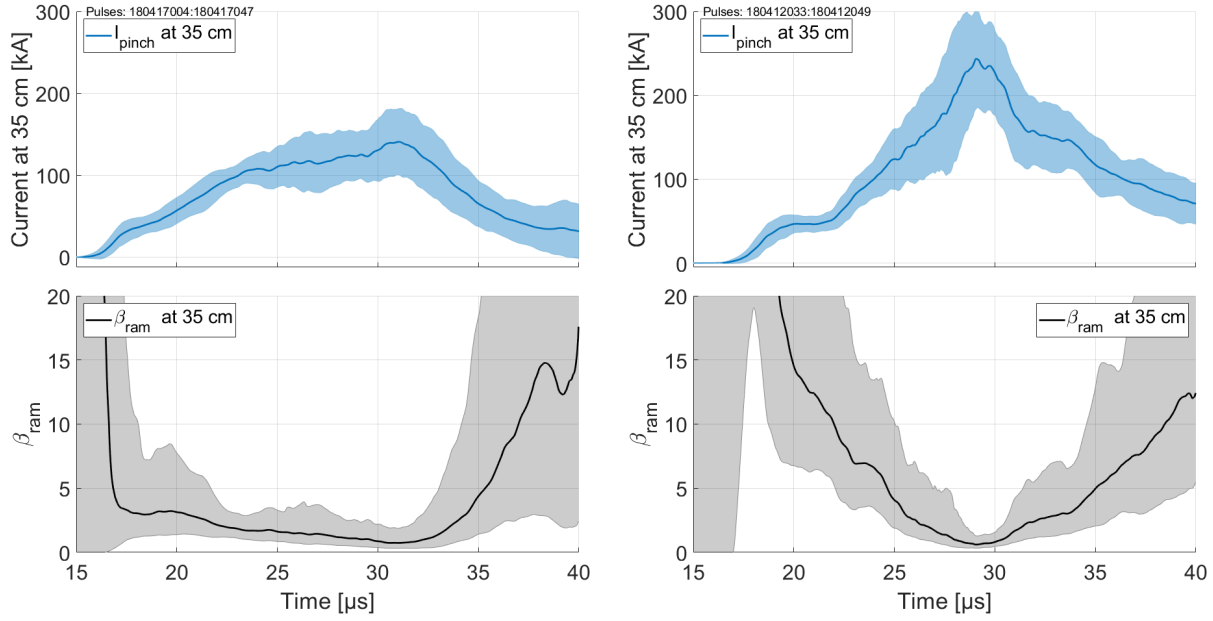

(a) (b)

Figure 2.11: β_{ram} calculated from the density signal at its corresponding current for Case 1 (a) and Case 2 (b), both for the spoked end wall. The plot shows, from top to bottom, the current 35 cm downstream of the nose cone and the calculated $\beta_{ram} = \frac{\rho_0 v_{z,0}^2 + p_0}{B_0^2/2\mu_0}$ obtained from the average and standard deviation signals of the current and density. Plasma velocities are measured from Doppler shifts of CIII lines as described in Sec. 2.1 and produce average values of 110 km/s and 140 km/s for Case 1 and Case 2, respectively. A temperature of 80 eV is used for the calculation of the thermal pressure.

2.3 Conclusion

The end wall acts as the downstream boundary of the flux conserver on FuZE. The open area increased 60-fold after changing the end wall to a spoked design. No apparent increase

in plasma exhaust is observed for Case 1, but an increase is shown to occur for Case 2. We show that the plasma is frozen to the magnetic flux and therefore the geometry change should have had minimal effect. However, we also show how the confinement at the end wall pass plasma when β_{ram} increases. The plasma that passes the end wall can then expand beyond the flux conserver where diffusion, detachment, or magnetic reconnection can take place.

It is found that the charge voltage condition that exhibits enhanced plasma exhaust also has a much higher initial value of beta compared to the condition without enhanced exhaust. We conclude that plasma exhaust can be achieved by increasing the plasma beta inside the flux conserver. In FuZE, this could be achieved by increasing the plasma density or bulk velocity. Increased plasma exhaust can also be achieved by maximizing the space between the fixed conducting path of the flux conserver, allowing for a larger magnetic radius of curvature R. On the end wall, this would translate into using larger spoke spacing and narrower spokes.

Chapter 3

PLASMA STAGNATION IN THE ASSEMBLY REGION

Chapter 2 showed that plasma was not freely passing through the end wall. Even with the spoked design, the end wall can act as a solid obstacle when β_{ram} is low enough. This leads to plasma piling up against the downstream end of the assembly region. This pileup is seen through high speed camera images in Fig. 2.5 where light propagates from the end wall to the nose cone. Moreover, the magnetic field contours of Fig. 2.6 show a high current region propagating against the direction of plasma flow coming from the accelerator. In this chapter, the reflected plasma wave is treated as a one-dimensional plasma shock. The plasma properties upstream and downstream of the stagnation wave are shown to be described by the Rankine-Hugoniot relations.

Moreover, measurements of peaked sheared flow profiles are shown to be related to the presence of stagnated plasma. Peaked sheared flow profiles can be formed by the viscous interaction of plasma with its surrounding. However, this chapter shows that the plasma perpendicular viscosity calculated from Braginskii cannot alone account for the scale length of the measured peaked profiles. Finally, limitations of this approach are presented by analyzing the line integrated density measurements and showing the apparent contradiction between the shock relations and the Z-pinch radial force balance. This leads to the conclusion that the line integrated density measurement mainly measures background plasma density and is not significantly influenced by the Z-pinch core density.

3.1 Velocity, current, density, and temperature measurements at $z = 15$ cm

This section presents data recorded at $z = 15$ cm where current, density, and velocity data are collected. Velocity from ion Doppler spectroscopy are recorded from the 45-degree telescope.

Figure 3.1 shows the current, velocity, and signal intensity for the set of pulses referred as "Case 2" in Chap. 2. The velocities are calculated from the Doppler shift of CIII (229.7 nm) and CV (227.1 nm, 227.7 nm, and 227.8 nm) impurity lines measured at $z = 15$ cm.

Initially, the CV signal intensity is too low to successfully fit a profile to it. Then, as current increases and as the Z-pinch plasma gets hotter, CV signal starts to appear, and velocities are calculated from the resulting fit. The CV velocity is on the same order as the initial CIII velocity. However, the velocity signal obtained from the CIII impurity falls to a value approaching zero as the current keeps increasing.

The difference between the CV and CIII signal after 25 µs indicates that the spectrometer measures simultaneously moving and stagnated plasma. CV requires more energy to ionize than CIII and is therefore associated with hotter plasma [45]. The CV emission is assumed to be located close to the axis in the center of the Z pinch, while the CIII emission is assumed to be coming from the cooler background plasma farther from the axis. The simultaneous measurements of moving CV impurities and static CIII impurities indicate that only the outer portion of the plasma is stagnating while the Z-pinch core keeps flowing.

The Gaussian fitting routine used to obtain the velocity in Fig. 3.1 is also used to calculate temperatures from the Doppler broadening of the impurity lines in Fig. 3.2. This temperature calculation is skewed toward an upper bound as the measurement of plasma populations moving at different velocities during the spectrometer exposure is interpreted as an artificially high temperature. The CIII velocities calculated from the measurements after 25 µs have low absolute values and their associated temperatures are representative of the stagnated plasma. This lower velocity group is identified by the red box in Fig. 3.2.

Figure 3.3 shows the contour of the magnetic field in the assembly region. This figure is the non-normalized version of Fig. 2.6 (c). The stagnation wave speed is estimated from the linear fits of the magnetic field contours between 30% and 50% of the maximum field. The estimated wave speed is $v_w = 104 \pm 14$ km/s.

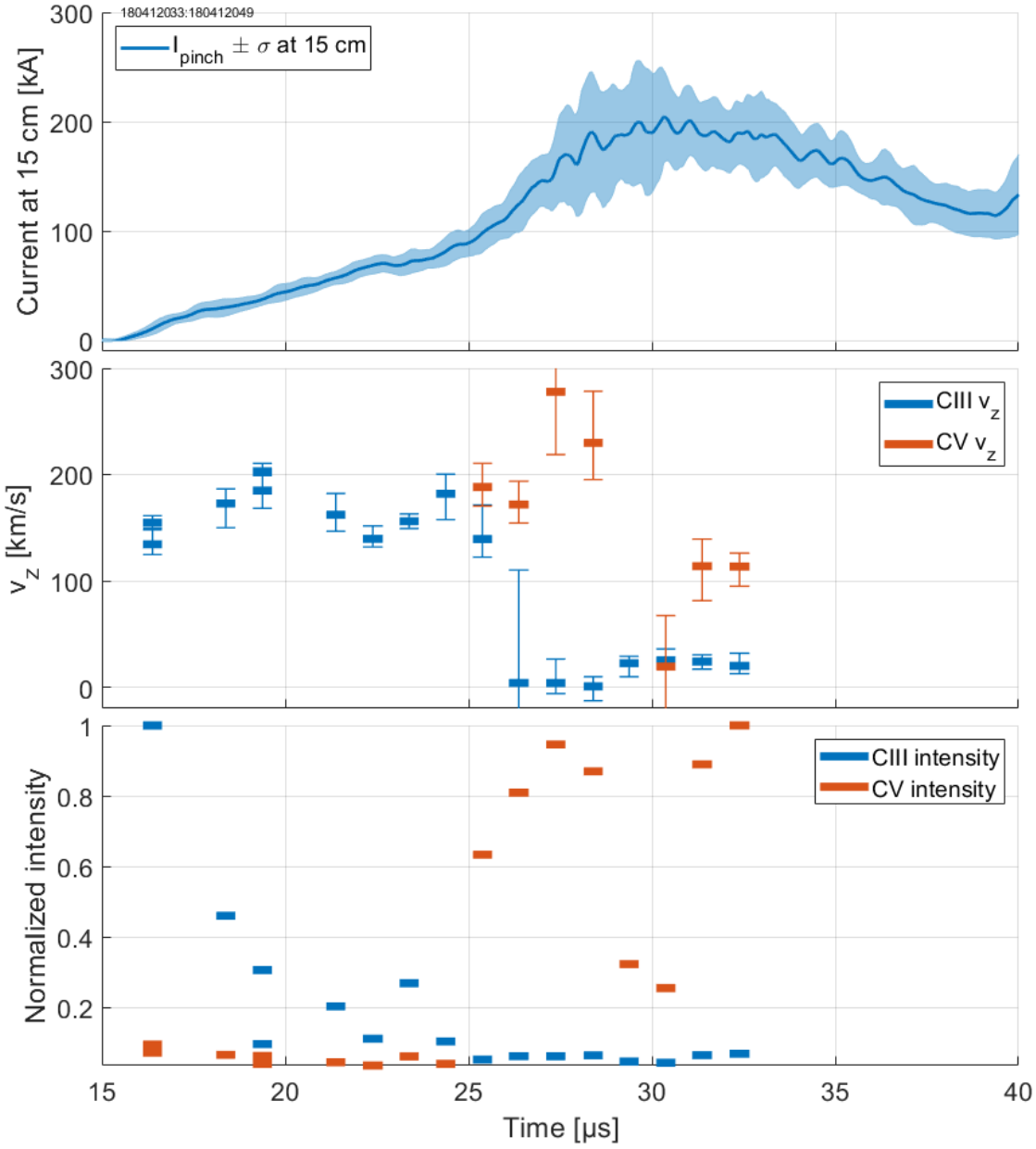

Figure 3.1: Plasma current, axial velocity, and signal intensity measured 15 cm downstream of the nose cone. The error bars on the velocity signal indicate the variation in the calculated fit between the 20 chords used to compute the average. The width of the velocity and intensity signal represent the 0.5 µs ICCD exposure. The CV signal (red) only reaches a sufficiently high intensity after 25 µs for the fitting route to properly calculate a velocity. The average velocity of the CIII before the stagnation is 162 ± 11 km/s.

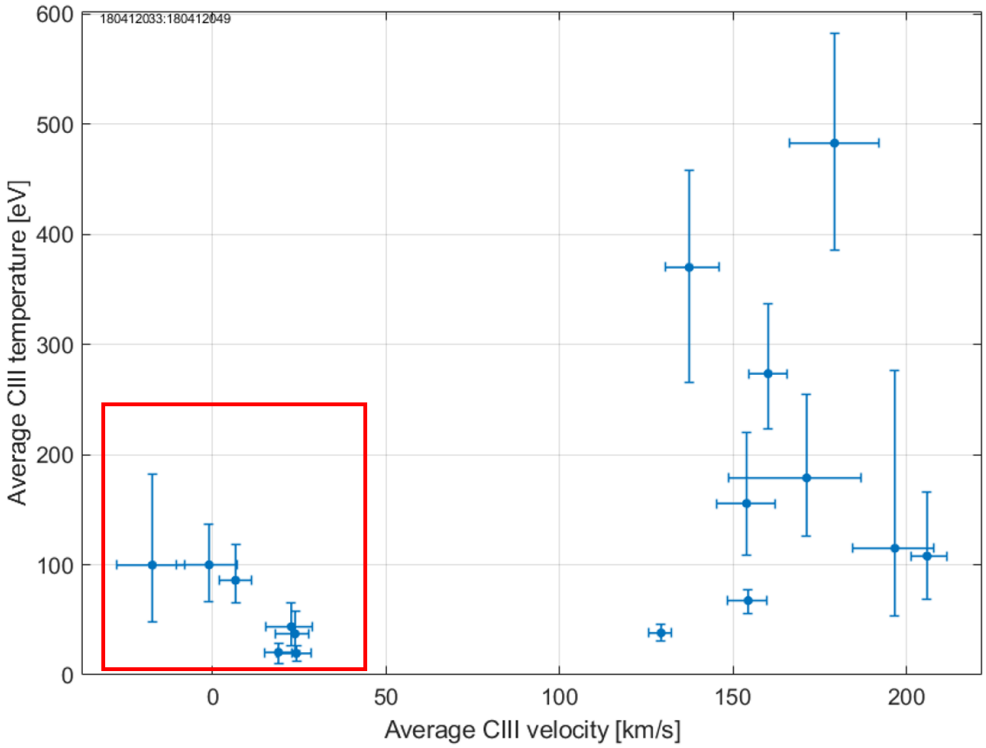

Figure 3.2: Temperatures calculated from Doppler broadening of CIII impurities as a function of the corresponding axial velocities calculated from the Doppler shift of CIII impurities. The spectroscopy data used are the same as Fig. 3.1. The low velocity group is identified by a red box and its average temperature is 58 ± 36 eV.

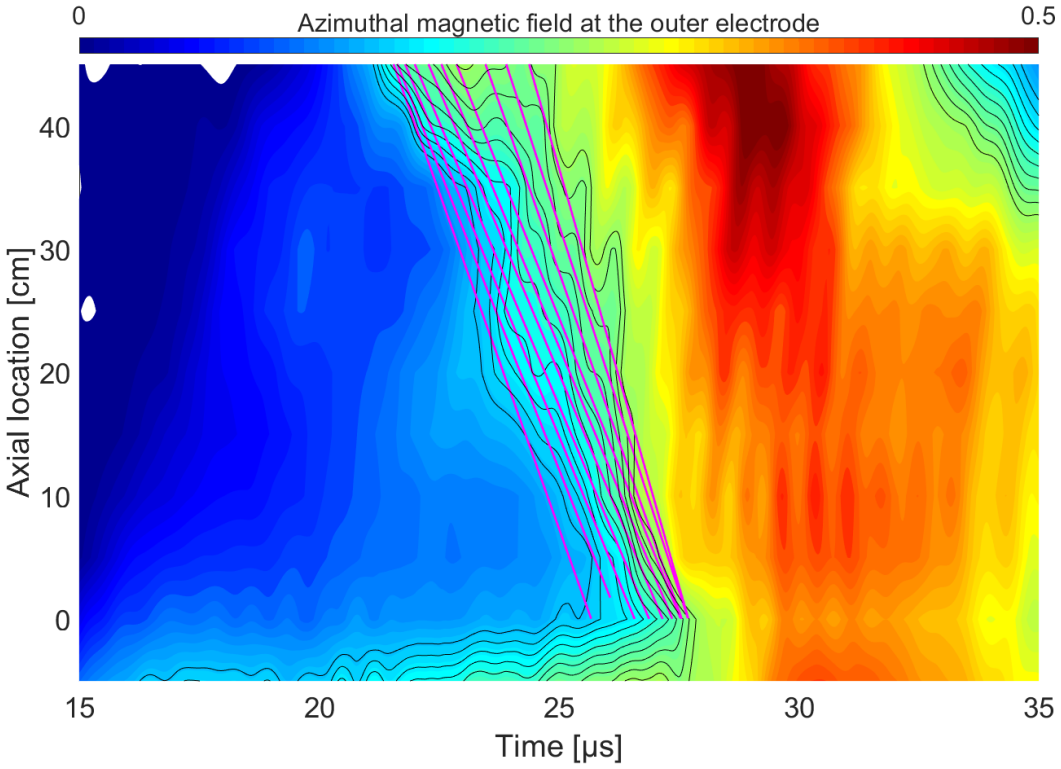

Figure 3.3: Contour of the magnetic field at the wall and linear fit of the contours (black lines) between 30% and 50% of the maximum magnetic field. The wave speed is calculated from the average and standard deviation of all the linear fits (magenta lines), leading to $v_w = 104 \pm 14$ km/s

.

3.2 The pinch assembly region as a 1D plasma shock tube

In past experiments [48, 49], coaxial accelerators have been successfully analyzed a 1D systems using the Rankine-Hugoniot relations. In a coaxial accelerator, the direction of flow (z) is perpendicular to the direction of the magnetic field (θ). In those systems, the MHD equations become analogous to the fluid Rankine-Hugoniot relations where the energy addition comes from the stored electrical energy instead of the chemical energy released by combustion.

Reflection of plasma was observed in early coaxial accelerator experiments [50]. In FuZE, the reflected plasma is seen in the magnetic field signal, shown in Fig. 3.3. The reflected plasma travels upstream from the end wall and its propagating velocity, v_w, is tracked by the slope of the magnetic contours. This wave is interpreted as a stagnation wave. In the frame of reference of the wave traveling at v_w, conservation relations are used, and the wave is treated as a shock. A schematic of the shock is shown in Fig. 3.4 in the shock reference frame.

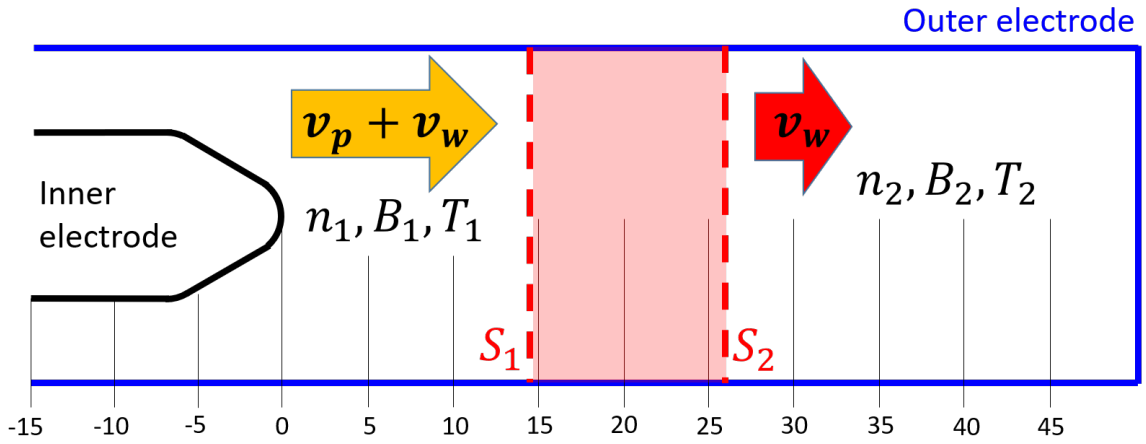

Figure 3.4: Velocities in the reference frame of the traveling stagnation wave, changing the plasma properties from the upstream (1) to the downstream (2) conditions.

Assuming that the wave leaves the plasma stagnated in the lab frame of reference, the

mass conservation relation across the shock leads to

$$(v_p + v_w)n_1 = v_w n_2 \tag{3.1}$$

$$\frac{n_2}{n_1} = \frac{v_p+v_w}{v_w} \tag{3.2}$$

where v_p is the upstream plasma velocity, n is the plasma number density, and subscripts 1 and 2 refer to upstream and downstream quantities, respectively. The ratio of downstream to upstream density, n_2/n_1, defines a compression ratio that is function only of the upstream plasma velocity and the wave velocity. If the magnetic field is frozen in flux throughout the assembly region and the shock is exactly perpendicular to the magnetic field, the magnetic field is also expected to scale with the density [51], that is

$$\frac{B_2}{B_1} = \frac{n_2}{n_1} \tag{3.3}$$

Using the conservative form of the momentum equation, the energy equation, and mass conservation in 1D, the Rankine-Hugoniot jump condition is obtained. Assuming that no energy is added in the reflecting plasma, the governing equation for the shock becomes

$$\frac{p_2^*}{p_1^*} = \frac{\frac{\gamma+1}{\gamma-1} - \frac{n_1}{n_2}}{\left(\frac{\gamma+1}{\gamma-1}\right)\frac{n_1}{n_2} - 1} \tag{3.4}$$

where γ is the ratio of heat capacities and p^* is the sum of thermal and magnetic pressures $p^* = nk_bT + B^2/2\mu_0$ where T is the plasma temperature, B is the magnetic field, and μ_0 is the permeability of free space. The Rankine-Hugoniot jump condition for a compressive shock is shown in Fig. 3.5.

The Rankine-Hugoniot relations predict an upper limit to the compression of an infinitely strong shock. This limit is given by

$$\frac{n_2}{n_1} \leq \frac{\gamma+1}{\gamma-1} \tag{3.5}$$

For a plasma with $\gamma = 5/3$, the maximum compression of an infinitely strong shock is $n_2/n_1 = 4$.

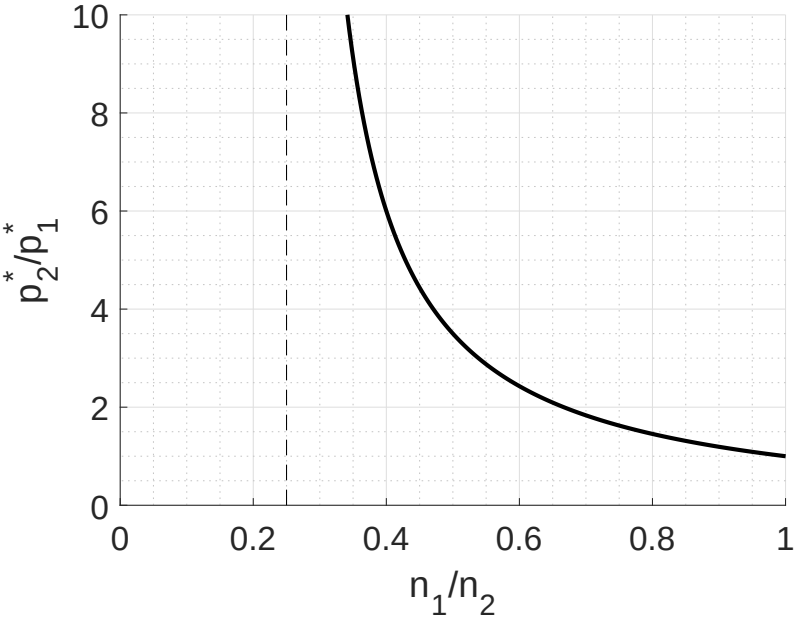

Figure 3.5: Rankine-Hugoniot jump condition for a plasma with $p^* = nkT + B^2/2\mu_0$ and no energy addition. The dashed line represents the infinitely strong shock case of $\rho_1/\rho_2 = 0.25$ for $\gamma = 5/3$.

The experiment size is limited, and it is useful to determine the expected scale length of the shock. In a collisionless process, the length at which the plasma properties change from state 1 to state 2 is dependent on the shorter scale between the electron inertial length (L_e) or the magnetic Reynolds length (L_m) [52], defined as

$$L_e = c/\omega_{pe} \tag{3.6}$$

$$L_m = \frac{\eta}{V_{ms}\mu_0} \tag{3.7}$$

where c is the speed of light, ω_{pe} is the electron plasma frequency, η is the plasma resistivity, and V_{ms} is the magnetosonic speed.

In a collisional shock, the shock scale length is given by the ion-ion collision mean free path [53], which is given by

$$\lambda_{mfp} = \frac{v_p}{\tau_{ii}} \tag{3.8}$$

where τ_{ii} is the ion-ion collision time and v_p is the plasma velocity. The collision frequency is given by

$$\tau_{ii} = 1 \times 10^{-12} n T_i^{-3/2} \tag{3.9}$$

where T_i is the ion temperature in eV and n is the plasma number density.

3.2.1 Experimental plasma parameters obtained from a stagnation wave

Using Eq. (3.2) and Eq. (3.4), the downstream stagnated plasma temperature is obtained as a function of the assumed upstream temperature. The results are shown in Fig. 3.6. From these results, the upstream plasma temperature has an upper bound of around 55 eV and a lower bound approaching 0 eV.

The compression ratio obtained from Eq. (3.2) is compared with the expected compression ratio from Eq. (3.3). Fig. 3.7 shows the magnetic field compression ratio as a function of the time at which the field reaches the downstream wave properties, B_2. The time at which the upstream magnetic field B_1 is taken is set to 25 µs based on the last time where finite

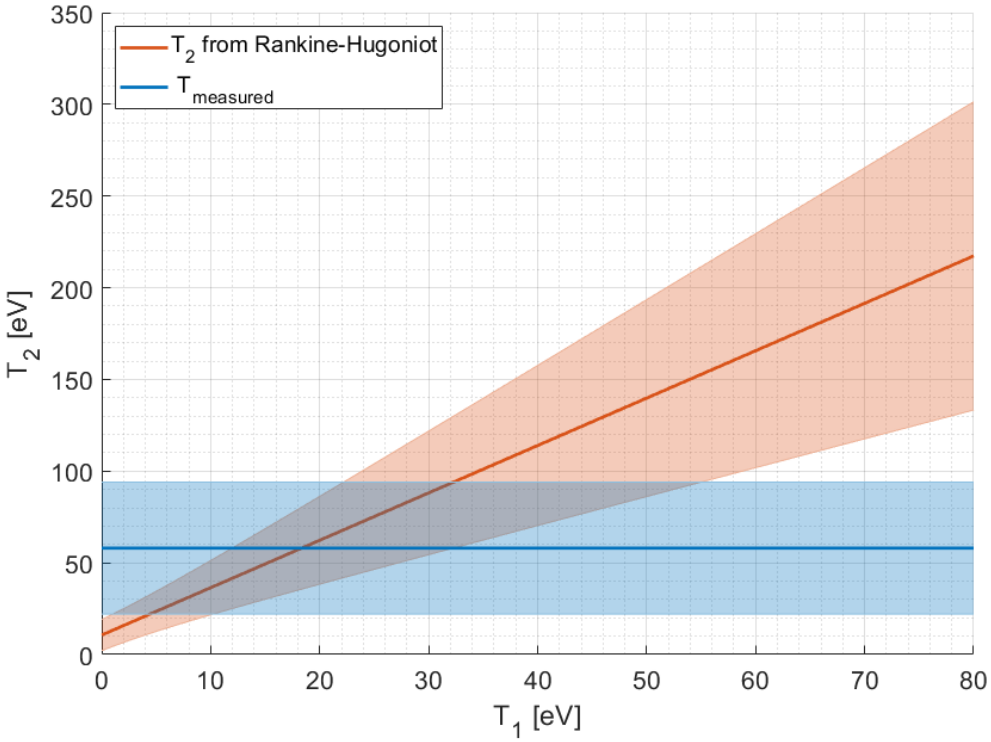

Figure 3.6: Stagnated temperature obtained from the Rankine-Hugoniot relations (red) as a function of upstream plasma temperature. The average temperature of plasma in the low velocity group of Fig. 3.2 is shown in blue.

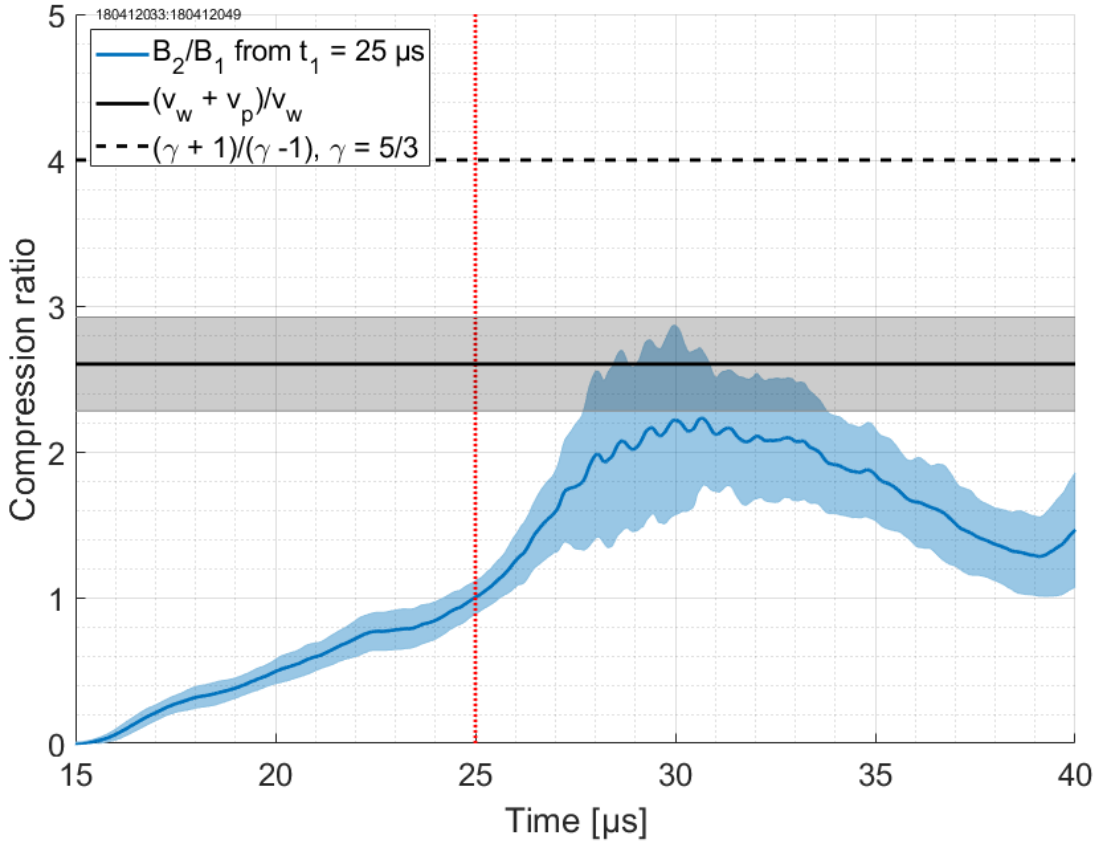

Figure 3.7: Magnetic field compression ratio (blue) as a function of timing of the downstream properties. The compression ratio obtained from Eq. (3.2) is shown in gray while the maximum compression ratio for $\gamma = 5/3$ from Eq. (3.5) is shown by the dashed line. The calculated density compression ratio is 2.6 ± 0.3.

CIII velocities are recorded in Fig. 3.1. Figure 3.3 also shows that the first magnetic field contours traveling toward the nose cone intersect $z = 15$ cm at approximately $t_{B_1} = 25\,\mu$s.

The calculated compression ratio and its error are shown by the gray region in Fig. 3.7. The maximum compression ratio of 4 for $\gamma = 5/3$ is shown by the dashed line. The first time the magnetic field compression ratio reaches the density compression ratio is at approximately $t_{B_2} = 28\,\mu$s.

Using this time and the measured wave speed, a minimum shock scale length is calculated

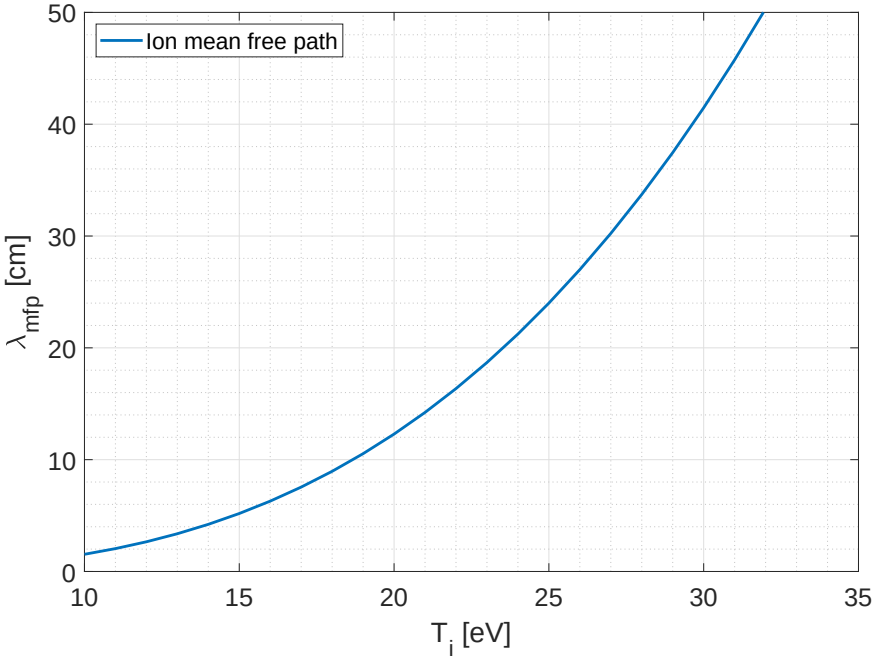

Figure 3.8: Ion mean free path for a plasma between 10 eV and 35 eV and an average density of $5 \times 10^{21}\mathrm{m}^{-3}$.

from

$$L_{shock} = v_w \left(t_{B_2} - t_{B_1}\right) \tag{3.10}$$

From Eq. (3.10), the minimum shock scale length is 27 cm. This scale length is much larger than the calculated electron skin depth or magnetic Reynolds length. However, it corresponds to the ion mean free path as shown in Fig. 3.8 for a 26 eV plasma with an average density corresponding to the measured line integrated density. This temperature is consistent with the calculated upstream and downstream temperatures of Fig. 3.6.

3.2.2 Sheared flow impacted by stagnated plasma

Previous studies on ZaP [7] and ZaP-HD [8] showed a Z-pinch sheared flow profile evolving from an initially "hollow" to a "peaked" velocity profile. A hollow profile is characterized by higher plasma axial velocity on the edge compared to the core of the pinch while a peaked

profile has a higher core velocity compared to the edge. The hollow profiles are seen in the early times and they eventually evolved to become peaked. The Z pinch can remain stable as long as shear is present, independent of its direction.

In FuZE, hollow profiles are observed at the beginning of a pulse while peaked profiles are measured toward the end, in agreement with the ZaP and ZaP-HD experiments. A hollow velocity profile is shown in Fig. 3.9 and a peaked velocity profile is shown in Fig. 3.10. Later in the pulse, it is possible to observe a transition between the flowing hot Z-pinch core to the colder stagnated off-axis plasma. This transition is shown in Fig. 3.11. The transition scale length is approximately 2 cm.

The presence of a transition between the Z-pinch plasma and the outer slower plasma suggests that the axial stagnation could be causing the peaked velocity shear profiles. The scale length of the transition and the expected scale length arising from the viscous drag between the Z-pinch core and the outer plasma are compared. This comparison demonstrates that viscous forces do not play a role in the formation of those shear profiles.

Viscosity perpendicular to a magnetic and perpendicular to a temperature gradient is given by [54]

$$\mu = n_i T_i \tau_i \frac{4.8\left(\omega_{ci}\tau_i\right)^2 + 2.23}{16\left(\omega_{ci}\tau_i\right)^4 + 16.12\left(\omega_{ci}\tau_i\right)^2 + 2.33} \tag{3.11}$$

where n_i is the ion number density, T_i is the ion temperature, τ_i is the ion collision time, and ω_{ci} is the ion cyclotron frequency.

A shear length scale is obtained by solving the viscous diffusion equation in cylindrical coordinates and approximating the derivatives with

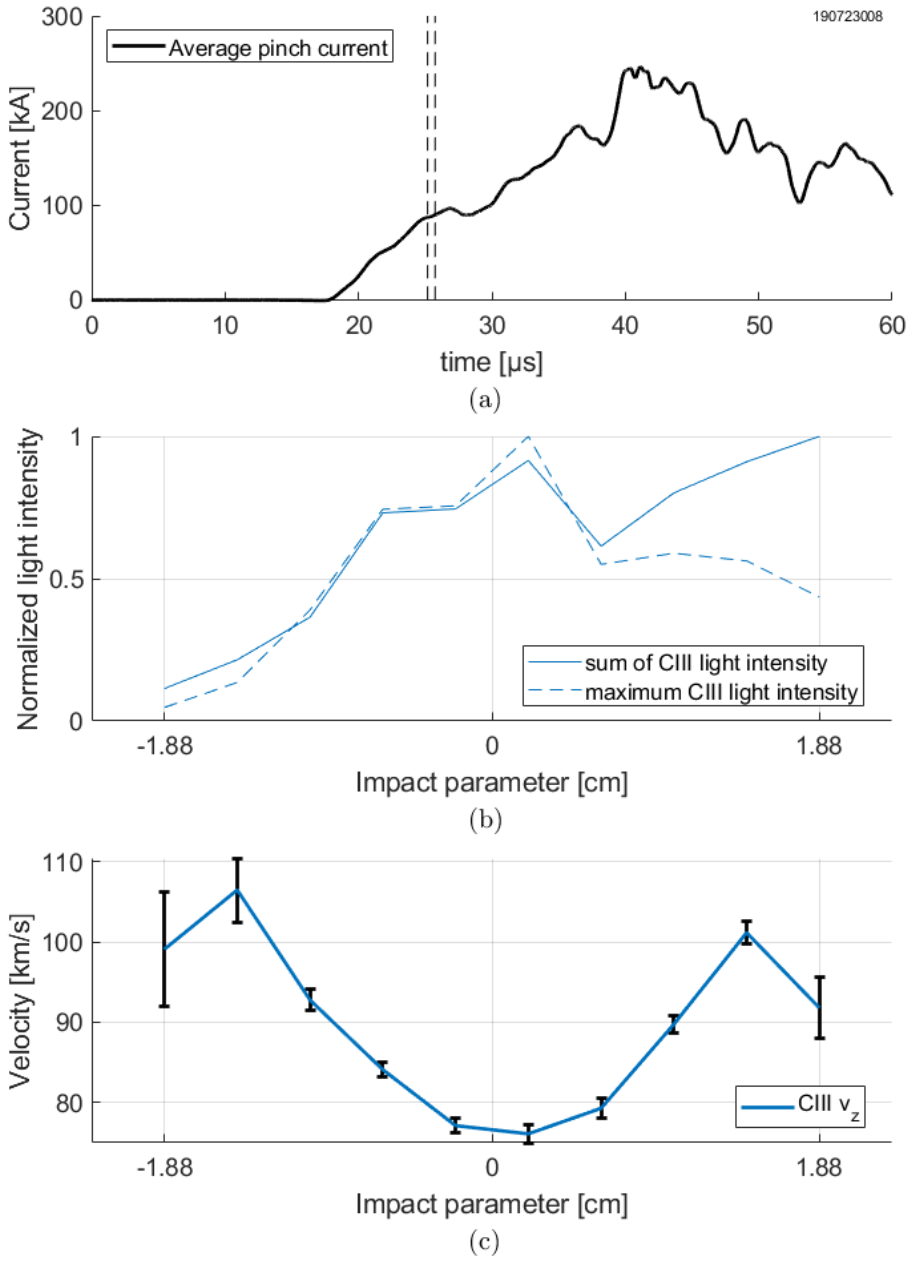

Figure 3.9: (a) Average Z-pinch current between z = 0 and 35 cm with the ICCD exposure identified by the vertical dashed lines. (b) Normalized light intensity recorded by the ICCD as a function of impact parameter using the total light intensity and the maximum recorded light intensity (dashed line). (c) Axial velocity as a function of impact parameter with error bars associated with fitting a Gaussian to the CIII 229.7 nm impurity line. The velocity profile shows a hollow velocity profile where sheared flow, dv_z/d_r, is positive through most of the pinch radius. The light intensity suggests a pinch centered around the minimum axial velocity.

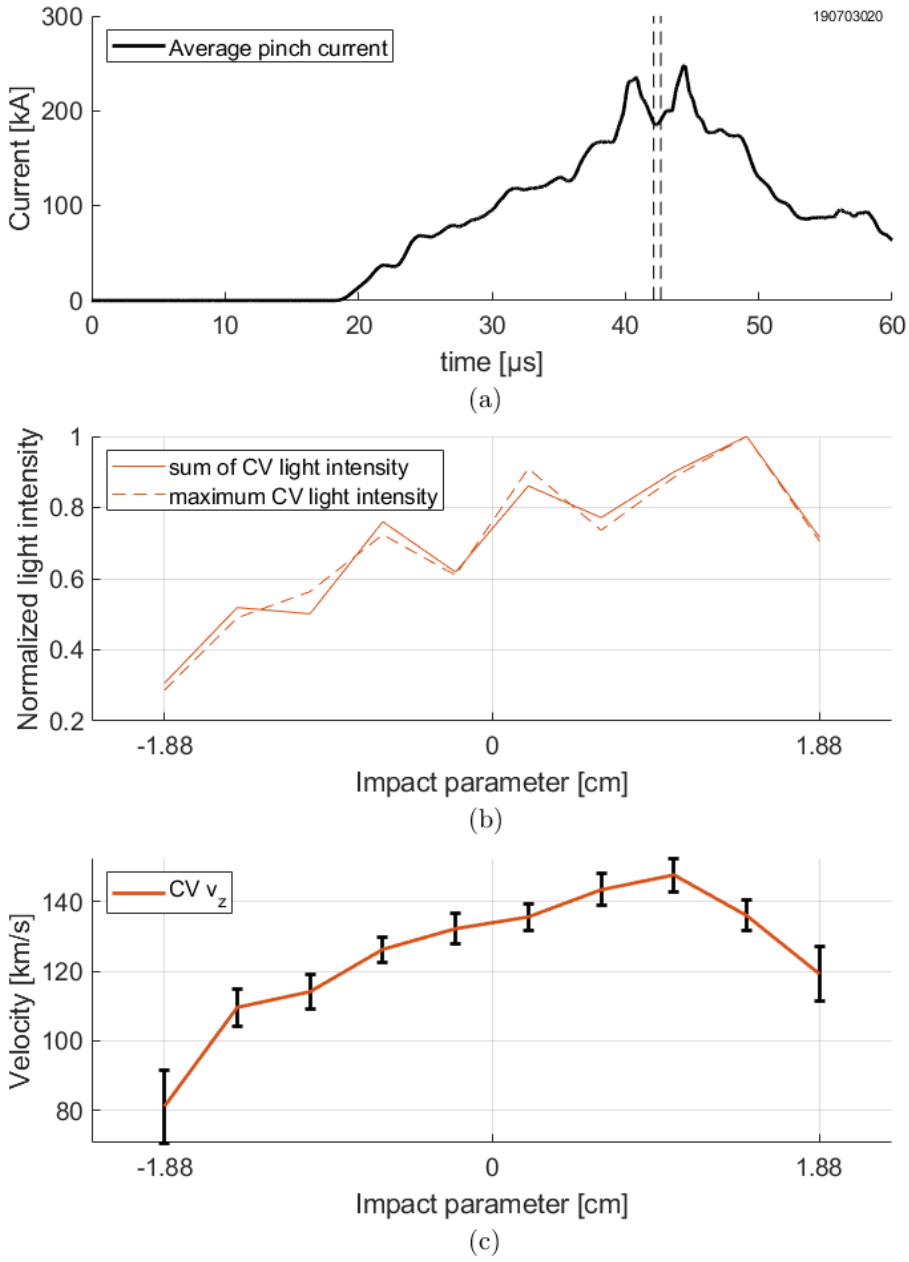

Figure 3.10: (a) Average Z-pinch current between z = 0 and 35 cm with the ICCD exposure identified by the vertical dashed lines. (b) Normalized light intensity recorded by the ICCD as a function of impact parameter using the total light intensity and the maximum recorded light intensity (dashed line). (c) Axial velocity as a function of impact parameter with error bars associated with fitting Gaussian curves to the CV impurity lines (227.1 nm, 227.7 nm, and 227.8 nm). The velocity profile shows a peaked velocity profile where sheared flow, dv_z/d_r, is negative through most of the pinch radius. The light intensity suggests a pinch centered around the maximum axial velocity.

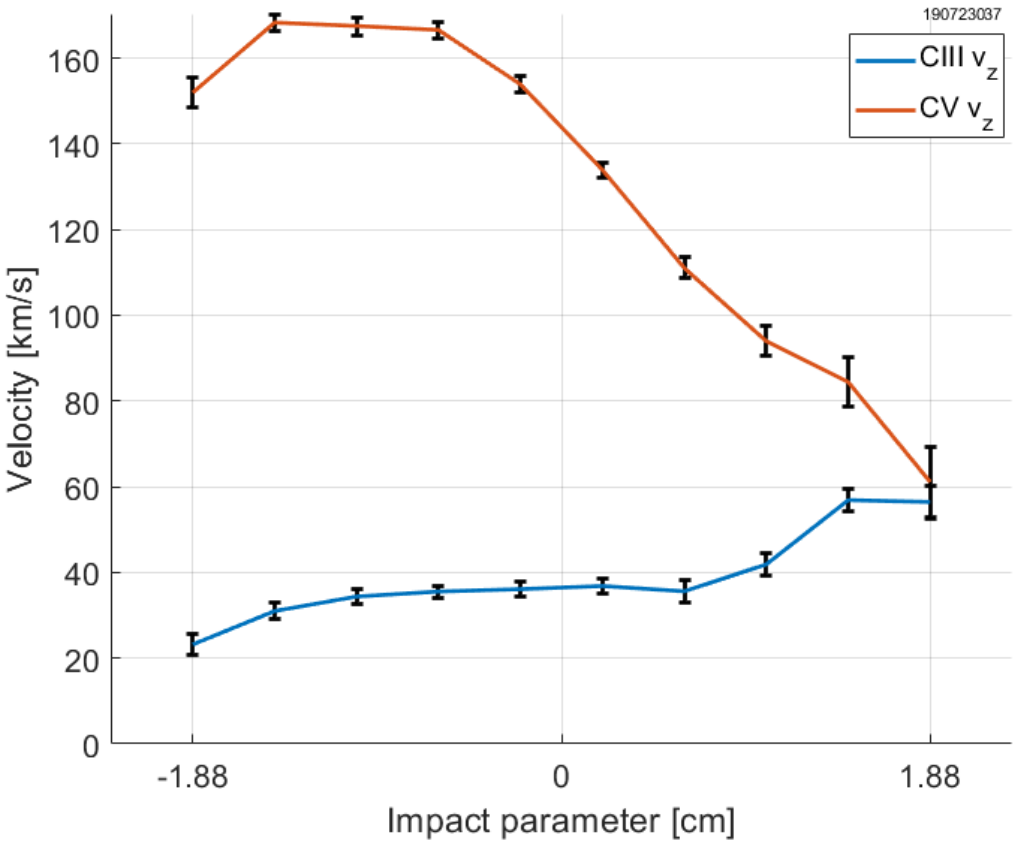

Figure 3.11: Axial velocity obtained from the Doppler shift of the (blue) CIII 229.7 nm impurity line and (red) the CV impurity lines (227.1 nm, 227.7 nm, and 227.8 nm). The CIII line is associated with colder, off-axis plasma while the CV lines are associated with hotter plasma present in the core of the Z pinch. The core plasma velocity is shown to meet the edge plasma velocity over a scale length of approximately 2 cm. The spectra are taken at $z = 25$ cm.

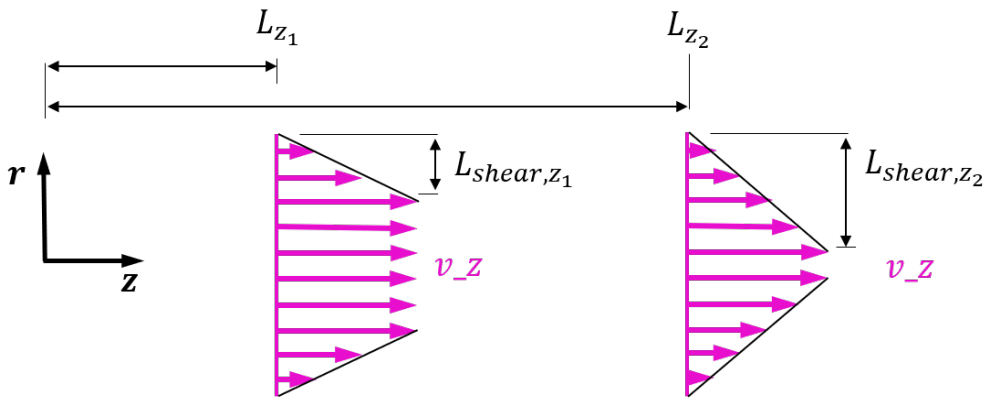

Figure 3.12: Shear scale length L_{shear} at two axial locations, L_{z_1} and L_{z_2}, with plasma velocity v_z. The shear scale length increases as the axial location increases. The distance required to reach a shear scale length depends on the plasma viscosity μ.

$$v_{z,0} = 0 \tag{3.12}$$

$$t_0 = 0 \tag{3.13}$$

$$\partial v_z = \Delta v_z = v_z - v_{z,0} = v_z \tag{3.14}$$

$$\partial t = \Delta t = t - t_0 = t \tag{3.15}$$

$$\partial r = \Delta r = r_{v_z} - r_{v_{z,0}} = L_{shear} \tag{3.16}$$

where $v_{z,0}$ is the stagnated velocity, t_0 is the time the shear forces start being applied, and $r_{v_{z,0}}$ is the radius at which the plasma has $v_{z,0}$ velocity, that is the radius at which plasma stagnates. L_{shear} is defined as the shear length scale. The time variable t is defined in terms of axial velocity v_z and axial location L_z with

$$t = \frac{L_z}{v_z} \tag{3.17}$$

The shear length scale, L_{shear}, then becomes [8]

$$L_{shear} = \sqrt{\frac{\mu L_z}{m_i n_i v_z}} \tag{3.18}$$

L_{shear} is the length in the radial direction over which the velocity goes from v_z to 0. The scale lengths L_{shear} and L_z are schematically shown in Fig. 3.12. A large shear scale length L_{shear} needs a long axial length L_z to develop. The axial location L_z at which the plasma reaches a specific shear scale length L_{shear} at a radius r depends on the plasma density and the plasma viscosity μ given by Eq. (3.11).

The velocity shear profile of Fig. 3.11 has a shear scale length of approximately 2 cm. The shear profile is recorded at $z = 25$ cm where the pinch current is approximately 200 kA. Using the line integrated density of $1 \times 10^{21}\mathrm{m}^{-2}$ as shown in Fig. 3.14 and a pinch radius of 1 cm, the shear scale length is calculated. A Bennett profile is assumed for the magnetic field. The density and temperature profiles are calculated from the radial force balance, assuming they both follow the same profile. The equilibrium analysis is similar to the analysis presented in Appendix A. The expected shear scale length from viscosity is then calculated as a function of the distance from the pinch axis, r. The results are shown in Fig. 3.13.

Figure 3.13 shows that viscosity is not a significant factor in creating the peaked sheared flow profile observed after the plasma has stagnated against the end wall. However, seeing the flow profile gradually reach the stagnated colder plasma suggests that plasma stagnation plays a role in the formation of the peaked sheared flow profiles. This flow profile, however, is not the result of a viscous interaction calculated using the viscosity from Eq. (3.11) because the calculated shear length scales of Fig. 3.13 are much lower than the measured scale length of 2 cm.

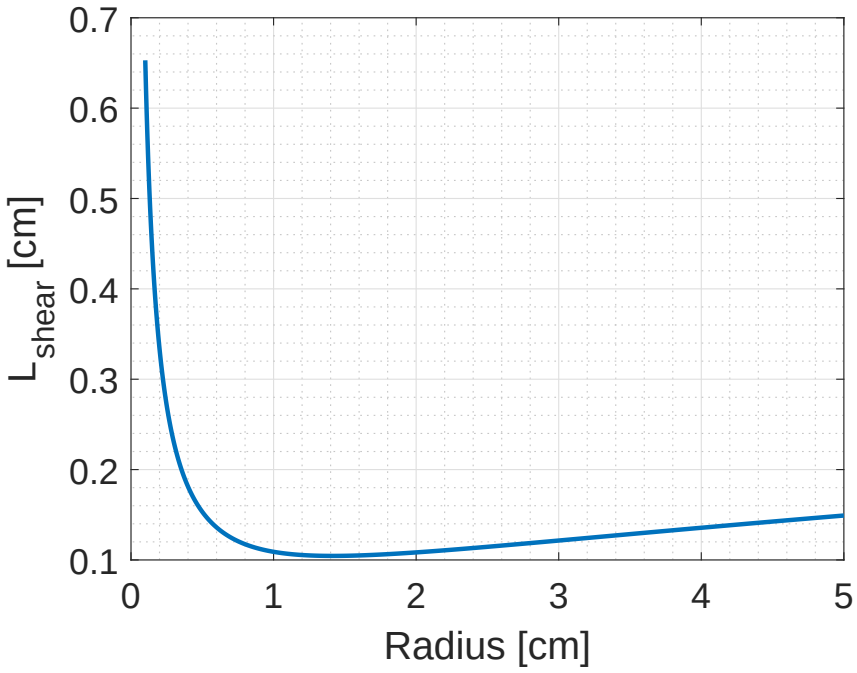

Figure 3.13: Shear scale length L_{shear} at $L_z = 25$ cm for a Z pinch with a 1 cm radius and a 200 kA plasma current. The expected shear from viscosity is much smaller than the observed 2 cm for all radial locations larger than 0.2 cm.

3.3 The line integrated density as a background density measurement

Line integrated density is measured at $z = 15$ cm and is shown in Fig. 3.14. The line integrated density stays mostly constant throughout the time of the measurement even as a stagnation wave is shown to travel through that axial location at approximately 25 µs. This section explores the parameter space that could allow a constant line integrated density measurement even though the density n is shown to increase by 2.6 ± 0.3 from Eq. (3.2).

Using a sharp pinch model, it is found that the line integrated density measurement is not compatible with the adiabatic scaling of a sharp pinch. Then, using a Bennet profile, it is found that allowing for more plasma off-axis still cannot satisfy the Z-pinch adiabatic scaling across a shock while keeping a constant line integrated density. Lastly, the line integrated density measurement is shown to be mainly dominated by background plasma as its value is not correlated with the current centroid location.

3.3.1 Sharp pinch model

The sharp pinch model assumes that the pinch density n and temperature T are constant throughout the pinch radius and fall to zero at the pinch radius a. A schematic of the model is shown in Fig. 3.15 along an indication of the linear density and the line integrated density.

Leaving the area of surface 1 and surface 2 (S_1 and S_2) in Fig. 3.4 free to change through the shock thickness and using a sharp pinch model, the conservation of mass in the wave frame of reference traveling at v_w toward the nose cone gives

$$S_2 n_2 = \frac{S_1 n_1 (v_1 + v_w)}{v_w} \tag{3.19}$$

where $S = \pi a^2$ and a is the pinch radius. Defining the linear density $N = n\pi a^2$, Eq. (3.19) becomes

$$N_2 = \frac{N_1 (v_1 + v_w)}{v_w} \tag{3.20}$$

From Eq. (3.20), the downstream linear density N_2 is larger than the upstream linear density N_1 by the ratio of upstream to downstream velocities. Using the measured upstream plasma

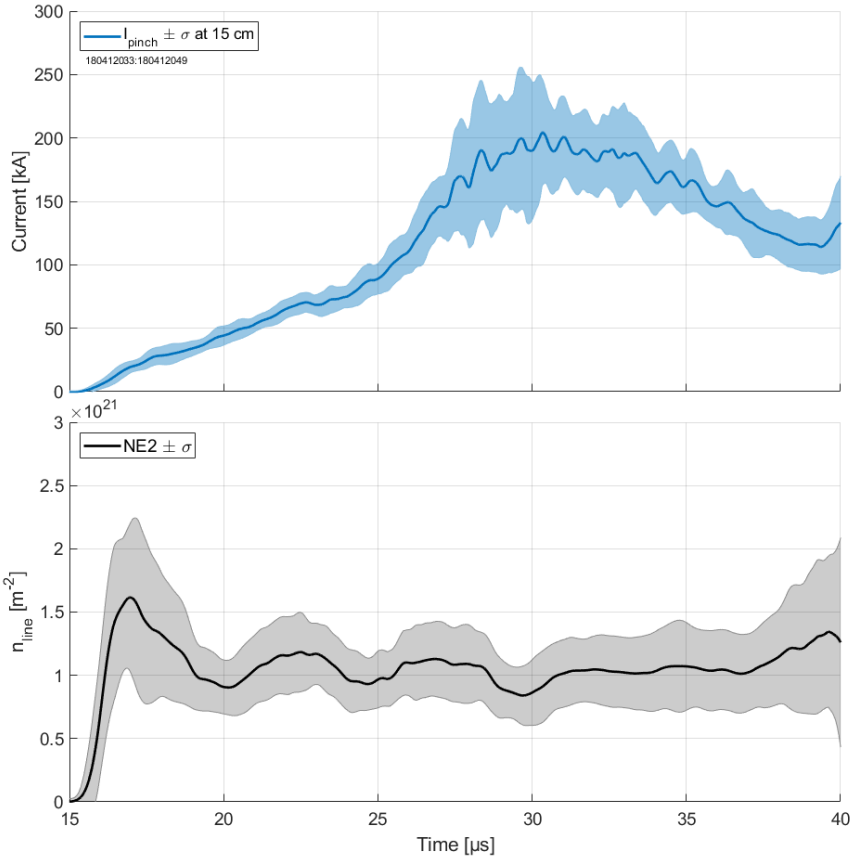

Figure 3.14: Plasma current and line integrated density measured 15 cm downstream of the nose cone. The line integrated density does not increase as the reflected plasma wave crosses the measurement location.

velocity ($v_p = 162 \pm 11\ km/s$) data from Fig. 3.1, assuming a downstream stagnated plasma, and using the wave velocity $v_w = 104 \pm 14$ km/s from Fig. 3.3, the downstream linear density (N_2) should be larger than the upstream linear density (N_1) by a factor of 2.6 ± 0.3.

This results seem to contradict the line integrated density shown in Fig. 3.14. The line integrated density remains unchanged even after the stagnation wave passes the location where the density is measured. However, the line integrated density shown in Fig. 3.14 is given by

$$n_{line} = 2na \tag{3.21}$$

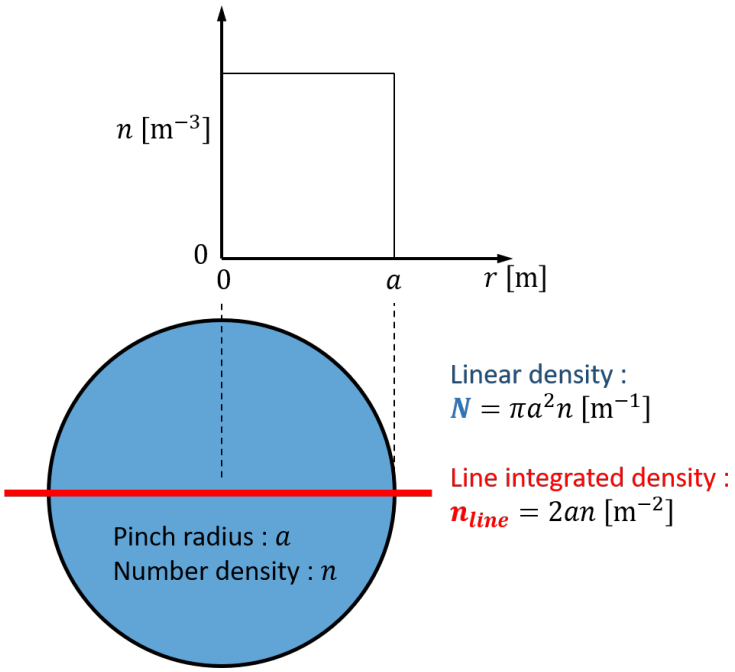

Figure 3.15: Density profile for the sharp pinch model and schematic of a cross section of a pinch with radius a and density n. The calculation of the linear density N and the line integrated density n_{line} from the pinch radius and number density are also shown. The laser path is represented in red while the cross section of the pinch is shown in blue.

where n_{line} is the line integrated density and n is the number density. An unchanged line integrated density across the shock ($n_{line,1} = n_{line,2}$) leads to

$$n_2 a_2 = n_1 a_1 \tag{3.22}$$

Using the definition of linear density for a sharp pinch, $N = n\pi a^2$, Eq. (3.22) becomes

$$\frac{N_2}{N_1} = \frac{a_2}{a_1} \tag{3.23}$$

The conservation of mass across the shock leads to an increase in linear density, as shown in Eq. (3.20). For this linear density increase to lead to a constant measured line integrated density $n_{line,1} = n_{line,2}$, the pinch radius has to increase by the same factor as the linear density N as shown in Eq. (3.23).

However, it was also shown in Sec. 1.1 from the adiabatic scaling of the sharp pinch that the pinch radius scales with

$$\frac{a_2}{a_1} = \left(\frac{I_1}{I_2}\right)^{\frac{1}{\gamma-1}} \left(\frac{N_2}{N_1}\right)^{\frac{\gamma}{2(\gamma-1)}} \tag{3.24}$$

where Eq. (1.14) is repeated here for convenience. With $\gamma = 5/3$, Eq. (1.14) becomes

$$\frac{a_2}{a_1} = \left(\frac{I_1}{I_2}\right)^{\frac{3}{2}} \left(\frac{N_2}{N_1}\right)^{\frac{5}{4}} \tag{3.25}$$

From Fig. 3.7, $I_2/I_1 = 2.2 \pm 0.6$. Figure 3.16 shows how the conditions of adiabatic Z-pinch scaling and constant linear densities cannot be both satisfied for the sharp pinch model using any density ratio.

3.3.2 Shock relations with a radial profile

The density profile is assumed to be a Lorentzian of the form

$$n(r) = n_0 \frac{a^2}{r^2 + a^2} \tag{3.26}$$

where a is the pinch radius and n_0 is the peak number density. This density profile corresponds to a Bennett equilibrium where the temperature and density follow the same profile.

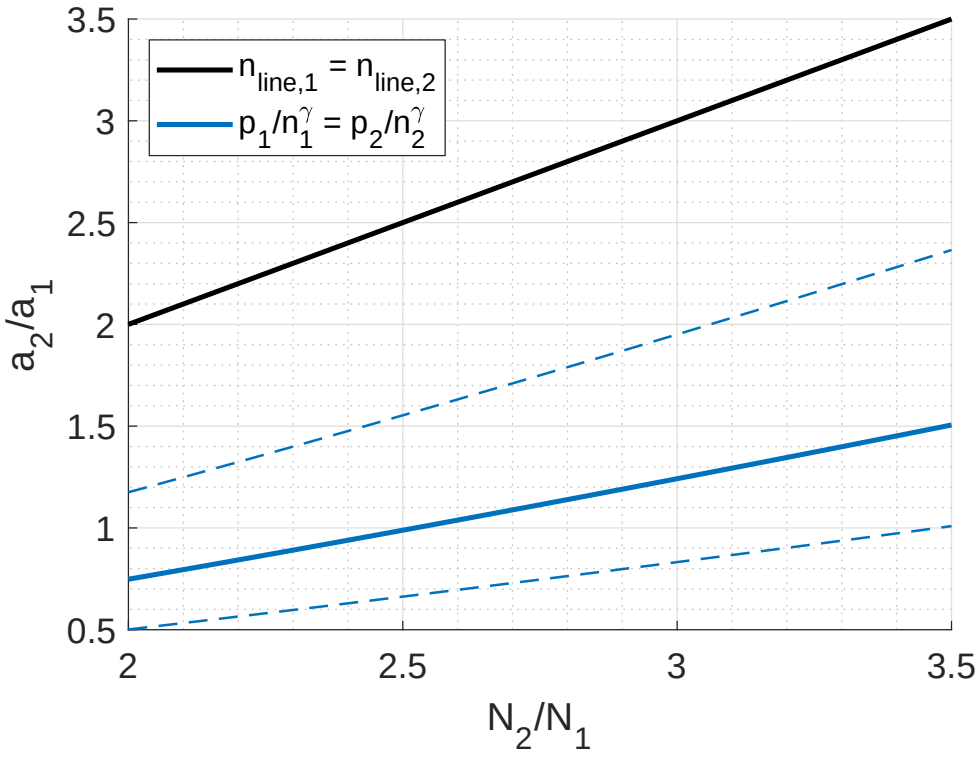

Figure 3.16: Ratio of pinch radius a_2/a_1 for the condition on constant linear density (black) and for the condition of pinch adiabatic scaling (blue) for a current ratio I_2/I_1 of 1.6 to 2.8 (dashed blue lines). The two curves never intersect, showing that the sharp pinch model cannot satisfy the observation of constant line integrated density across a jump as well as the pinch adiabatic scaling.

This radial Z-pinch equilibrium assumes a magnetic field with

$$B(r) = \frac{\mu_0 I}{2\pi} \frac{r}{r^2 + a^2} \tag{3.27}$$

where I is the pinch current. From the Z-pinch force balance, the pressure profile is

$$p(r) = \frac{\mu_0 I^2}{8\pi^2} \frac{a^2}{(r^2 + a^2)^2} \tag{3.28}$$

The conservation of mass equation becomes

$$\int_0^{2\pi} \int_0^{R_w} n_1(r)(v_p + v_w) r dr d\theta = \int_0^{2\pi} \int_0^{R_w} n_2(r) v_w r dr d\theta \tag{3.29}$$

$$(v_p + v_w)\, n_{0,1} a_1^2 \ln\left(\frac{R_w^2 + a_1^2}{a_1^2}\right) = (v_w)\, n_{0,2} a_2^2 \ln\left(\frac{R_w^2 + a_2^2}{a_2^2}\right) \tag{3.30}$$

where $n_{0,i}$ is the peak density at surface i and R_w is the outer electrode wall radius. The velocities are assumed to be radially uniform. The pinch linear density is

$$N = \int_0^{2\pi} \int_0^{R_w} n(r) r dr d\theta \tag{3.31}$$

$$= \pi n_0 a^2 \ln\left(\frac{R_w^2 + a^2}{a^2}\right) \tag{3.32}$$

such that Eq. (3.30) becomes

$$(v_p + v_w)\, N_1 = (v_w)\, N_2 \tag{3.33}$$

The line integrated density measured by the He-Ne interferometer is given by

$$n_{line} = 2 \int_0^{R_w} n(r)\, dr \tag{3.34}$$

$$n_{line} = 2 a n_0 \arctan\left(\frac{R_w}{a}\right) \tag{3.35}$$

Using 3.32 and Eq. (3.35):

$$n_{line} = \frac{2N \arctan(R_w/a)}{\pi a \ln(R_w^2/a^2 + 1)} \tag{3.36}$$

For an unchanged line integrated density across a shock, Eq. (3.36) becomes

$$\frac{2N_1 \arctan(R_w/a_1)}{\pi a_1 \ln(R_w^2/a_1^2 + 1)} = \frac{2N_2 \arctan(R_w/a_2)}{\pi a_2 \ln(R_w^2/a_2^2 + 1)} \tag{3.37}$$

The Z-pinch radial force balance between the state (1) and state (2) is used to relate how the radius a scales with a known change in pinch current I and density ratio n_2/n_1. The pinch is assumed to evolve adiabatically throughout the stagnation wave, such that

$$\frac{\mathrm{d}}{\mathrm{dt}}\left(\frac{p}{n^{\gamma}}\right)=0 \tag{3.38}$$

integrating Eq. (3.38) over a constant volume to get

$$\iiint_V \frac{\mathrm{d}}{\mathrm{dt}}\left(\frac{p}{n^{\gamma}}\right) dV = 0 \tag{3.39}$$

If the integration volume V is constant in time, Eq. (3.39) becomes

$$\frac{\mathrm{d}}{\mathrm{dt}}\left(\iiint_V \frac{p}{n^{\gamma}} dV\right)=0 \tag{3.40}$$

$$\frac{\mathrm{d}}{\mathrm{dt}}\left(\int_L^{L+\Delta L}\int_0^{2\pi}\int_0^{R_w} \frac{p}{n^{\gamma}}\, dz\, d\theta\, dr\right)=0 \tag{3.41}$$

where L and ΔL are arbitrary and constant axial distances. The pressure p is obtained from the Z-pinch radial force balance using a Bennett profile, shown in Eq. (3.28). Performing the integration at state (1) and state (2) and using the pressure profile of Eq. (3.28) and the density from Eq. (3.26), the adiabatic relation between state (1) and (2) becomes

$$\frac{I_1^2}{n_{0,1}^{\gamma}}\left(a_1^{2(1-\gamma)}\left(R_w^2+a_1^2\right)^{\gamma-1}-1\right)=\frac{I_2^2}{n_{0,2}^{\gamma}}\left(a_2^{2(1-\gamma)}\left(R_w^2+a_2^2\right)^{\gamma-1}-1\right) \tag{3.42}$$

$$\frac{I_1^2}{n_{0,1}^{\gamma}}\left(\left(\frac{R_w^2}{a_1^2}+1\right)^{\gamma-1}-1\right)=\frac{I_2^2}{n_{0,2}^{\gamma}}\left(\left(\frac{R_w^2}{a_2^2}+1\right)^{\gamma-1}-1\right) \tag{3.43}$$

Using Eq. (3.32),

$$\frac{I_1^2}{N_1^{\gamma}}\left(\left(\frac{R_w^2}{a_1^2}+1\right)^{\gamma-1}-1\right)a_1^2\ln\left(\frac{R_w^2}{a_1^2}+1\right)=\frac{I_2^2}{N_2^{\gamma}}\left(\left(\frac{R_w^2}{a_2^2}+1\right)^{\gamma-1}-1\right)a_2^2\ln\left(\frac{R_w^2}{a_2^2}+1\right) \tag{3.44}$$

The results from Eq. (3.44) and Eq. (3.37) are shown in Fig. 3.17 along with the sharp pinch model. While the Bennett profile relaxes the adiabatic radius scaling for small radius values ($a < 5$), it simultaneously increases the scaling from the constant linear density condition.

Steeper density profiles eventually converge to the sharp pinch model while more gradual density profiles give similar results to the Bennett case. In summary, neither the Bennett Z-pinch equilibrium profile or the sharp pinch profile can both satisfy the requirement of the adiabatic scaling and the constant linear density.

3.3.3 Radial dependence of measured density

This section shows that the measured density is not correlated with pinch location, meaning that the line integrated density is measuring mostly the background density. This removes the requirement that the calculated radius must follow an adiabatic Z-pinch radial pressure equilibrium evolution. Figure 3.18 shows the line integrated density measurement and the vertical location of the current centroid calculated from the normalized mode data with

$$\Delta y = \frac{1}{2} R_w \sin\phi \frac{m_1}{m_0} \tag{3.45}$$

where R_w is the wall radius, ϕ is the angular location of the magnetic field centroid given by m_1, and m_0 is the average value of the magnetic field. The line integrated density measurement is obtained from a laser oriented perpendicular to the yz plane of the experiment. Assuming that the plasma is continuous in the z axis and that the peak plasma density is at the current centroid, the density should be at its maximum when the centroid of the pinch is coincident with the laser path. That is, the density is maximized for $\Delta y = 0$.

Figure 3.18 shows that there is no apparent correlation between the average vertical position and the average line integrated density measurement. From this data set, Fig. 3.19 shows the density measurement against the vertical position for each pulse at each digitization point. There appears to be a slight correlation with vertical position. That is, when the vertical displacement is small, higher line integrated density is measured. The same data set is plotted in a histogram form for all vertical displacement values less than 1 cm in Fig. 3.20a and all vertical displacement values greater than 1 cm in Fig. 3.20b. The 1 cm limit is chosen as the laser beam diameter is on the order of a few millimeters.

Figure 3.20 shows that while there are a few instances of high density recorded when

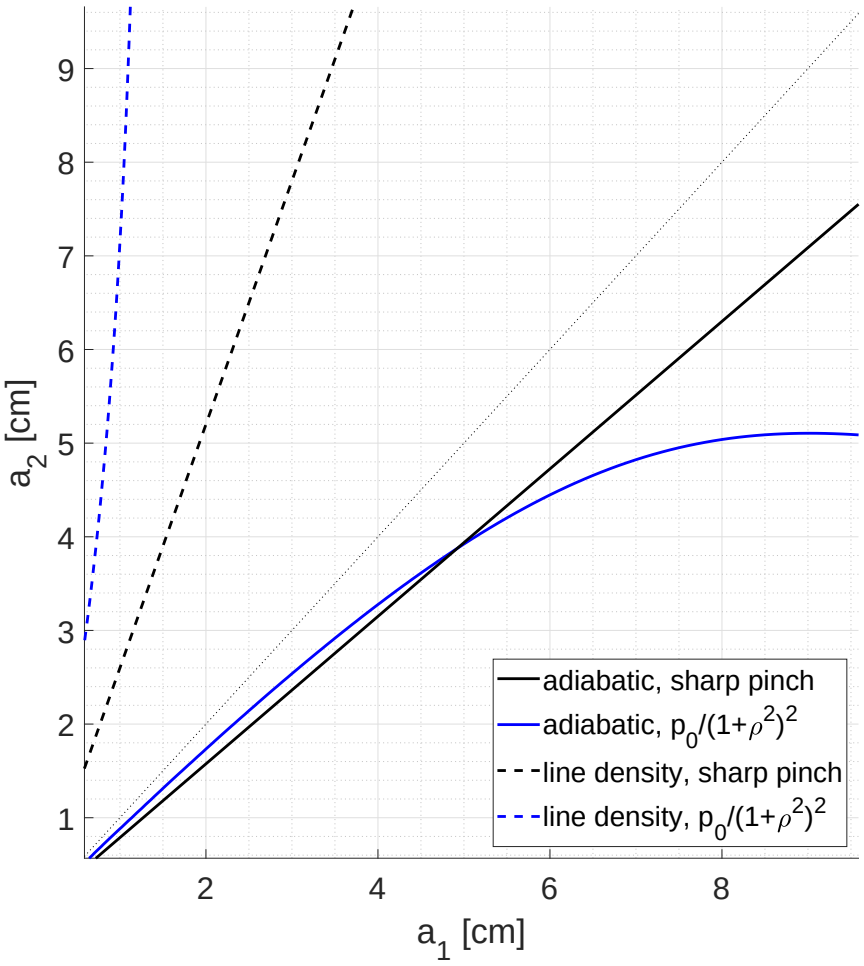

Figure 3.17: Required post shock radius a_2 as a function of pre-shock radius a_1 for the sharp pinch profile (black) and the more gradual Bennett profile (blue). The combination of radii required to satisfy both the constant line integrated density (dashed lines) and the adiabatic scaling of the pinch (full lines) would be indicated by the intersection of these curves. These curves never intersect, showing that the condition of Z-pinch adiabatic scaling based on force balance is in contradiction with the observed constant line integrated density.

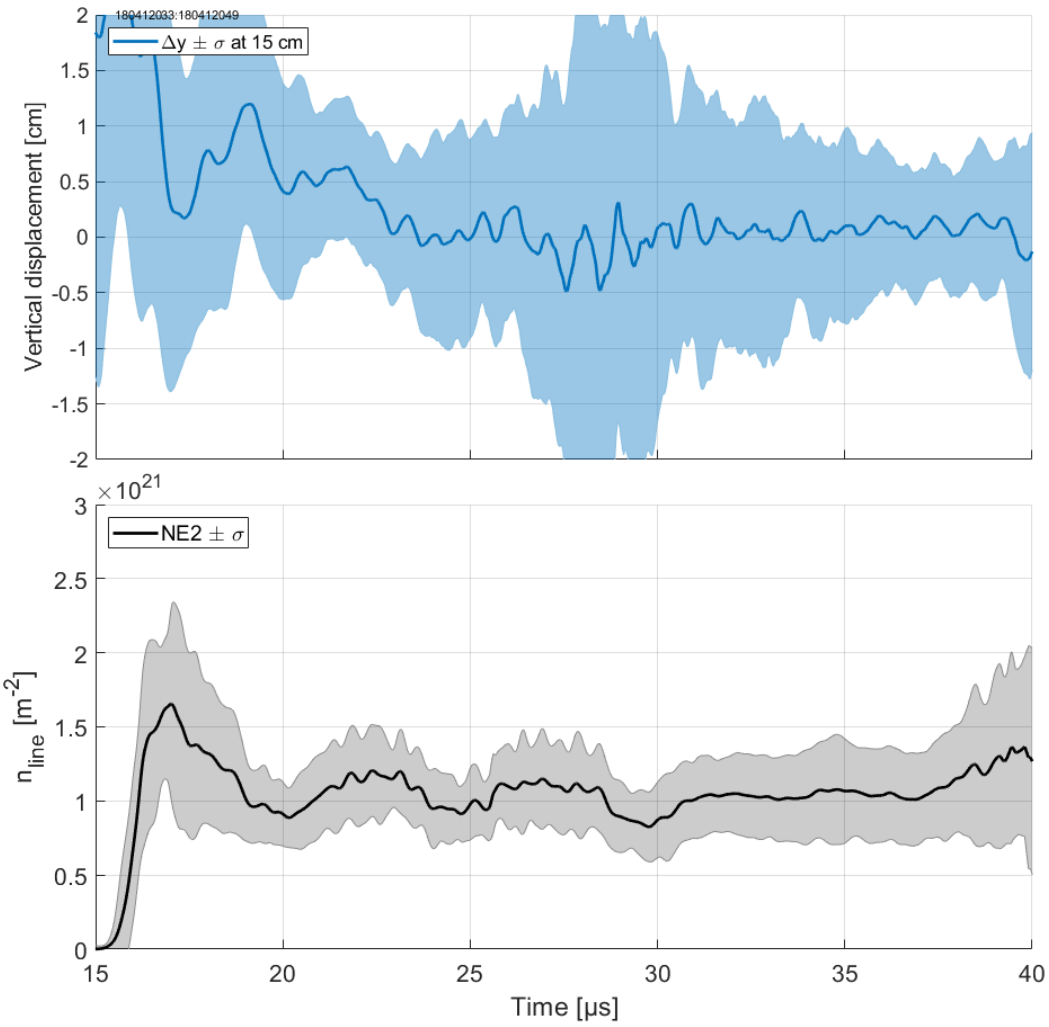

Figure 3.18: Pinch vertical position (top) and line integrated density (bottom) at $z = 15$ cm. The shaded area indicates the standard deviation of the signal obtained from multiple pulses.

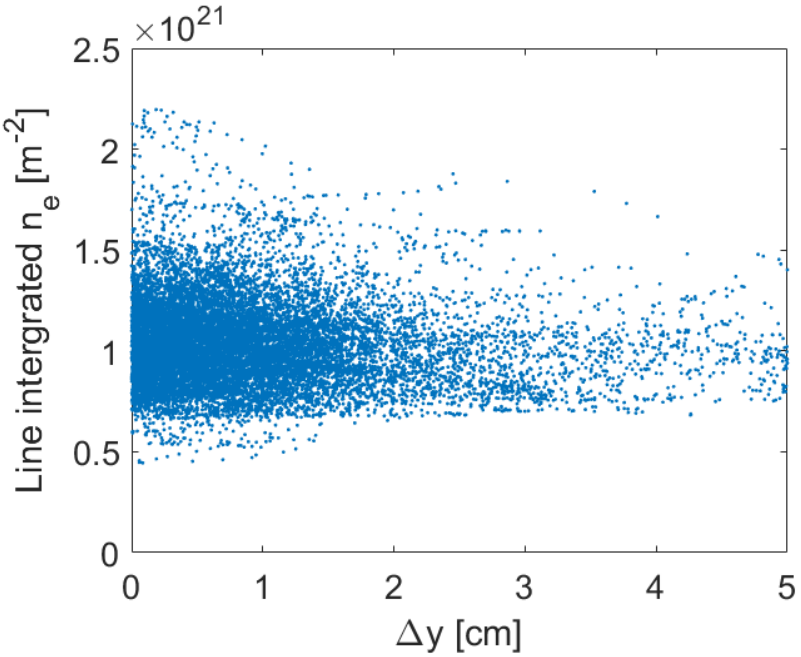

Figure 3.19: All recorded line integrated density data points and pinch vertical position between 18 µs and 35 µs. The small number of higher line integrated density measurements are seen only when the vertical pinch displacement is small.

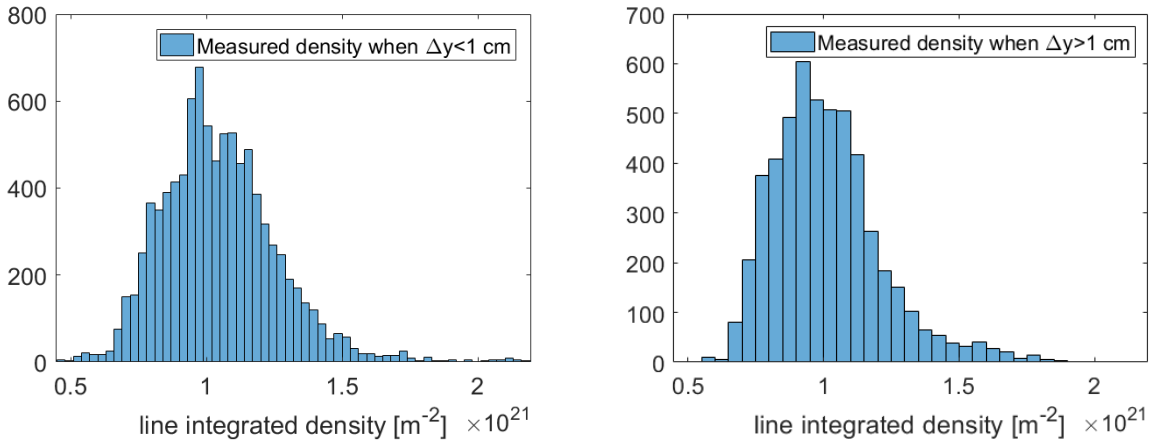

(a) (b)

Figure 3.20: Total number of data points at a specific line integrated density for (a) $y < 1$ cm and (b) $y > 2$ cm. If the dense pinch core is measured by the line integrated density measurement, the curve is expected to be shifted to the right for the case where the pinch is captured through the laser path (a) while the line integrated density should be shifted to the left when it is not (b). The average value of all line integrated density measurements when $y < 1$ cm is $1.05 \times 10^{21}\mathrm{m}^{-2}$ while the average of the line integrated density when $y > 1$ cm is $1.01 \times 10^{21}\mathrm{m}^{-2}$.

the displacement is small, the majority of density measurements are not influenced by the position of the pinch centroid. In other words, the density at the center of the pinch does not influence the line integrated density measurement.

This could happen if the pinch diameter is small and rarely exactly in the path of the laser beam. In that case, the laser measures mostly the background plasma density. The background plasma density can be force free if it is uniform and no axial current flows through it. In that case, the constant line integrated density is explained by the background density having a characteristic radius $a_1 < a_2$. That is, the background density fills a greater radial extent of the assembly region after the stagnation shock. This satisfies the black curve in Fig. 3.16.

3.4 Conclusion

This chapter showed that the assembly region background density stagnates through a collisional shock, increasing its density and consequently inducing axial currents in the Z pinch in order to keep the magnetic flux constant in the stagnated background plasma.

First, waves propagating opposite to the plasma fluid flow are observed in the magnetic field and through high speed camera images. The CIII impurity velocity is observed to go to zero as the backward wave reaches the measurement location. Analysis using the Rankine-Hugoniot relations shows that this behavior is consistent with a stagnation wave which could be caused by the plasma's inability to completely exhaust through the end wall. The stagnation shock is found to be collisional.

The observed transition of the velocity shear profiles from hollow to peaked could be related to the stagnating plasma. However, viscosity is ruled out as the driving mechanism for the formation of the peaked sheared flow profile. Finally, it is shown that the line integrated density measurements depend on the background plasma density.

Chapter 4

NEUTRON SCALING WITH PINCH CURRENT

Neutron generation is an unambiguous sign of the presence of nuclear fusion reactions in a plasma. Knowing how the yield increases with plasma parameters is important in order to find a viable path toward an energy-producing reactor concept. For example, dense plasma foci (DPF) are used as a neutron source. It was found that the yield scales as $\propto I^4$ [21]. This scaling is much lower than the ideal adiabatic scaling of I^{11} assuming a constant linear density. As such, DPF generate neutrons mainly from a beam acceleration process [22] that does not scale to net gain conditions [55].

The Z-pinch pathway toward an energy producing nuclear fusion reactor core depends on its scaling with pinch current [56]. In this chapter, the neutron yield is investigated as it is a direct measurement of the nuclear fusion events in the Z pinch.

Neutrons were measured on FuZE [42]. The emission time of 5 µs, the absence of instabilities, the scaling of yield with deuterium density, and the consistency of the measured yield with the pinch density, temperature, and radius showed that the neutrons were likely of thermonuclear origin. Subsequently, the emission volume was found to be consistent with a uniform 30 cm line source [36], supporting that the neutrons were emitted throughout the Z-pinch volume, consistent with a thermonuclear reaction.

In this chapter, the neutron yield scaling is investigated. The yield (Y) is directly proportional to the neutron counts (C), $Y \propto C$, obtained from the Eljen EJ-204 plastic scintillator coupled with a photomultiplier tube [36]. The yield is compared to the Z-pinch axial current using a binning method that takes advantage of the time resolved nature of the neutron measurements. The neutron yield is found to be proportional to approximately I^7. This scaling could be consistent with an adiabatic evolution of the Z pinch only if the pinch

current increases with the linear density.

4.1 Theoretical yield scaling from the adiabatic Z-pinch force balance

The neutron scaling relationship for a sharp pinch is developed. The scaling relations derived in Sec. 1.1 are used. These relationships are derived from the MHD radial equilibrium, assuming a sharp pinch model, and assuming an adiabatic evolution.

The neutron yield is given by the following equation for the D-D fusion reaction

$$Y = \frac{l\tau}{2} \int_0^{R_{wall}} n_D^2(r) \langle \sigma v \rangle \, 2\pi r dr \tag{4.1}$$

where R_w is the outer electrode radius, n_D is the deuterium density, l is the emission length, τ is the emission time, and $\langle \sigma v \rangle$ is the reaction rate for $\mathrm{D}\,(d,n)\,^3\mathrm{He}$ fusion. The emission length is the axial extent over which thermonuclear reactions are taking place in the Z pinch. The emission time is the measured time over which neutrons are emitted from the pinch.

For the sharp pinch model, the yield equation simplifies to

$$Y = l\tau\pi a^2 n_D^2 \langle \sigma v \rangle \tag{4.2}$$

where a is the pinch radius. Between the range of 1 to 3 keV, the DD fusion reaction rate is approximately proportional to T^4, that is $\langle \sigma v \rangle \propto T^4$ as shown in Fig, 4.1. This can further simplify the reaction rate term. Using the equations for temperature T, density n, and radius a scaling (Eqs. (1.10), (1.13), (1.14)) with the equation for the neutron yield of the D-D reaction (Eq. (4.2)), a scaling relationship for the yield that depends only on the pinch current I and the linear density N is obtained.

$$Y \propto l\tau \frac{I^{11}}{N^{4.5}} \tag{4.3}$$

For a constant linear density N, the thermonuclear neutron yield is proportional to I^{11}. The following section compares the neutron counts, which are directly proportional to the neutron yield, with the plasma axial current.

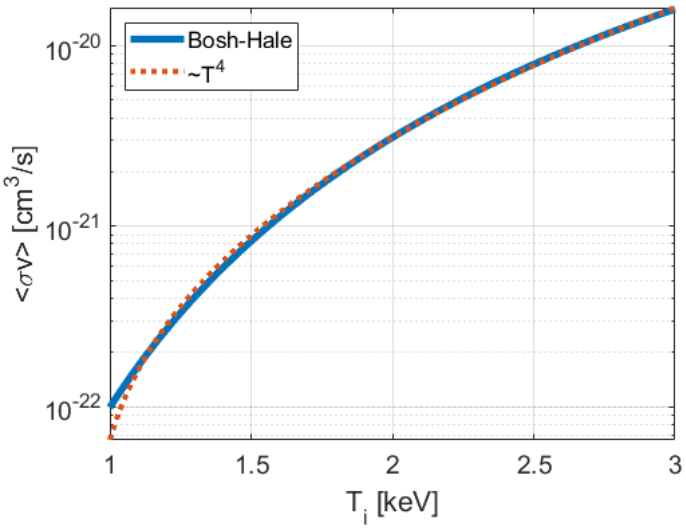

Figure 4.1: Reaction rate for a plasma with an ion temperature between 1 and 3 keV obtained from [57] (blue line) and reaction rate fit with $\langle \sigma v \rangle \propto T^4$ (red dotted line).

4.2 Instantaneous neutron scaling

The pulse counting method presented in [36] is time resolved. This characteristic is used to compare the neutron yield with the current measured at the same time as the yield.

Figure 4.2 shows the neutron detector signal from neutron detector 8 (ND8) and neutron detector 4 (ND4) located respectively at 40 and 80 cm from the Z-pinch axis. The solid angle Ω scales between $\Omega \propto R^2$ for a point source and $\Omega \propto R$ for an infinite line source, where R is the distance from the Z-pinch axis. As such, the counts are expected to be between two and four times larger for ND8 compared to ND4. Each local maximum is counted as one neutron. The counts are binned over a fixed bin time and the sum of all maxima (voltage peaks) in each time bin is represented by the gray bars in Fig. 4.3 and 4.4.

Figure 4.3 shows the average Z-pinch current and neutron count calculated over 70 pulses compared with the current and neutron count from one of the pulses. The current of each pulse oscillates at a higher frequency than the average value computed using all the pulses. Also, the neutrons are not emitted uniformly throughout the elevated current period between

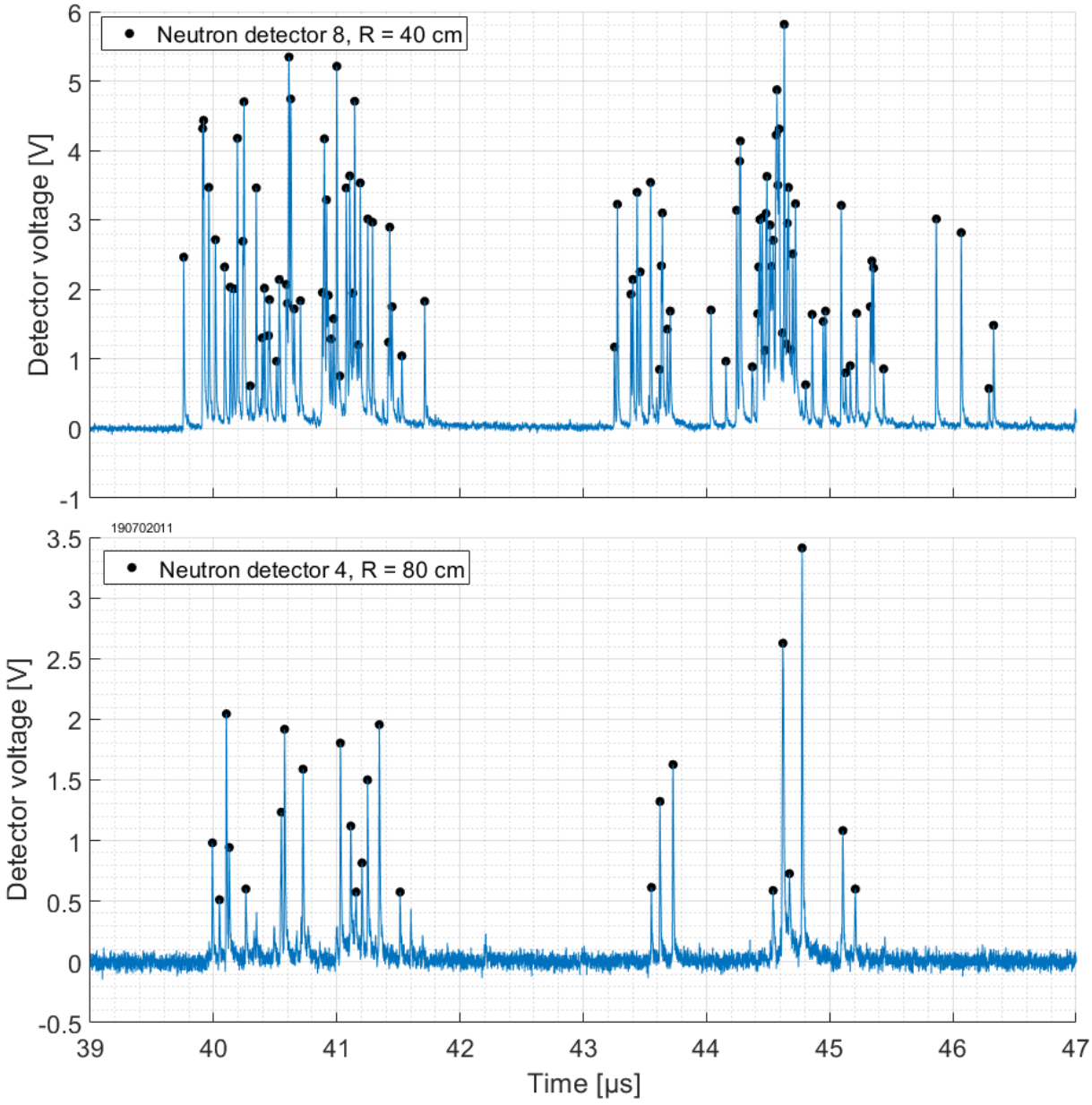

Figure 4.2: Neutron detector signal for the neutron detector 8 (ND8) located 40 cm from the axis and neutron detector 4 (ND4) located 80 cm from the axis. Each voltage peak is recorded as a count and is identified by black dots. Only the peaks above 0.5 V are recorded, in accordance with the detector calibration described in [36].

40 and 45 µs.

In this section, the neutron signal is compared with the instantaneous current. In particular, the behavior of the neutron yield scaling to the bin width and the current chosen for comparison are investigated.

Each pulse is divided in time bins. At each time bin, the average current and the total neutron counts are calculated. Figure 4.4 shows a representation of the binning process for one pulse using 1 µs bins. This method creates multiple data points from one pulse. For example, the pulse shown in Figure 4.4 would only lead to a single yield value with a single average current value if time resolved measurement were not available. Using the time resolved neutron signal, a single pulse leads to 10 values of currents and 10 values of yield between the 40 and 50 µs time window.

This method is limited by the neutron detector resolution and operational limitations. A small binning time is preferable as it creates more current data points to investigate the scaling. However, the neutron detectors have a maximum counting rate limited by two effects: detector shutoff, and pulse pileup.

The shutoff effect is suspected of being linked to the depletion of charges in the photomultiplier tube of the neutron detectors where a high neutron flux leads to the output signal shutting off. Pileup is observed when the neutron fluence increases to the point where a voltage peak is recorded before the signal from the previous peak has time to decay, leading to counting error. The decay time of each peak is approximately 20 ns, limiting the counts to 50 counts/µs to avoid pileup.

As a consequence, the neutron detectors have to be placed sufficiently far from the Z-pinch to be used. As the neutron emission rate varies greatly during the emission time, the bin time needs to be large enough to obtain a sufficient dynamic range. As the bin size increases, the neutron counts dynamic range increases, but the current accuracy and time localization decrease. At the limit of small bin sizes, the neutron signal delay from the different cable lengths as well as the time of flight becomes important when compared with the measured current. The following analysis calculates the scaling for different bin sizes.

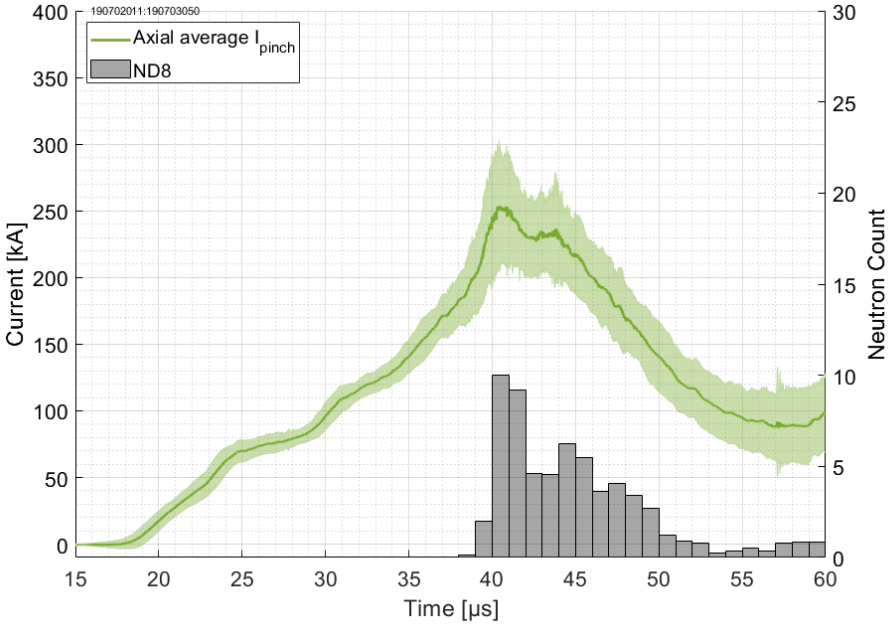

(a)

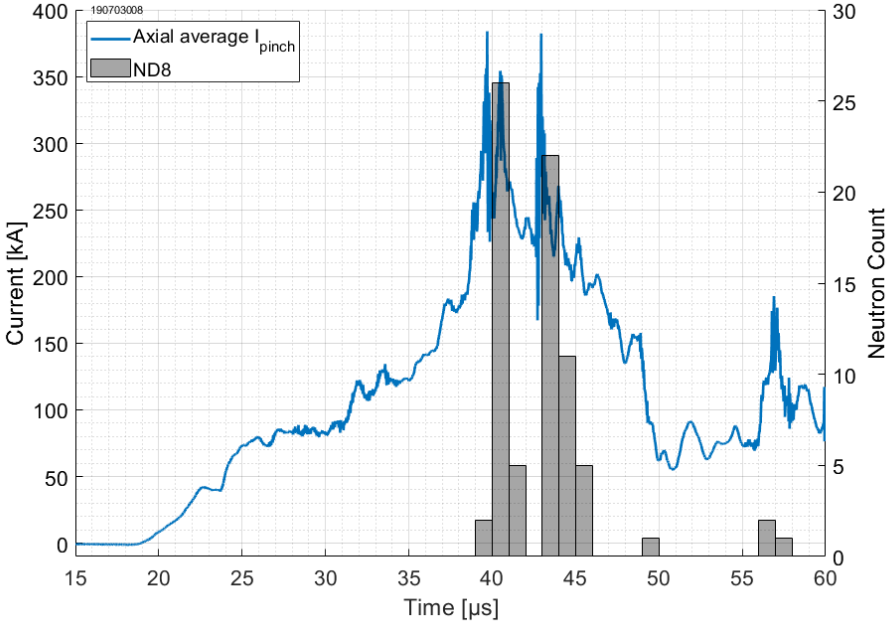

(b)

Figure 4.3: (a) Average Z-pinch current between 0 and 30 cm for 70 plasma pulses with corresponding average counts on neutron detector 8 (ND8) placed 40 cm from the Z-pinch axis. (b) Pinch current and counts for one of the 70 pulses used in (a). The neutron emission is not uniform and tends to be concentrated in groups between 40 and 45 μs.

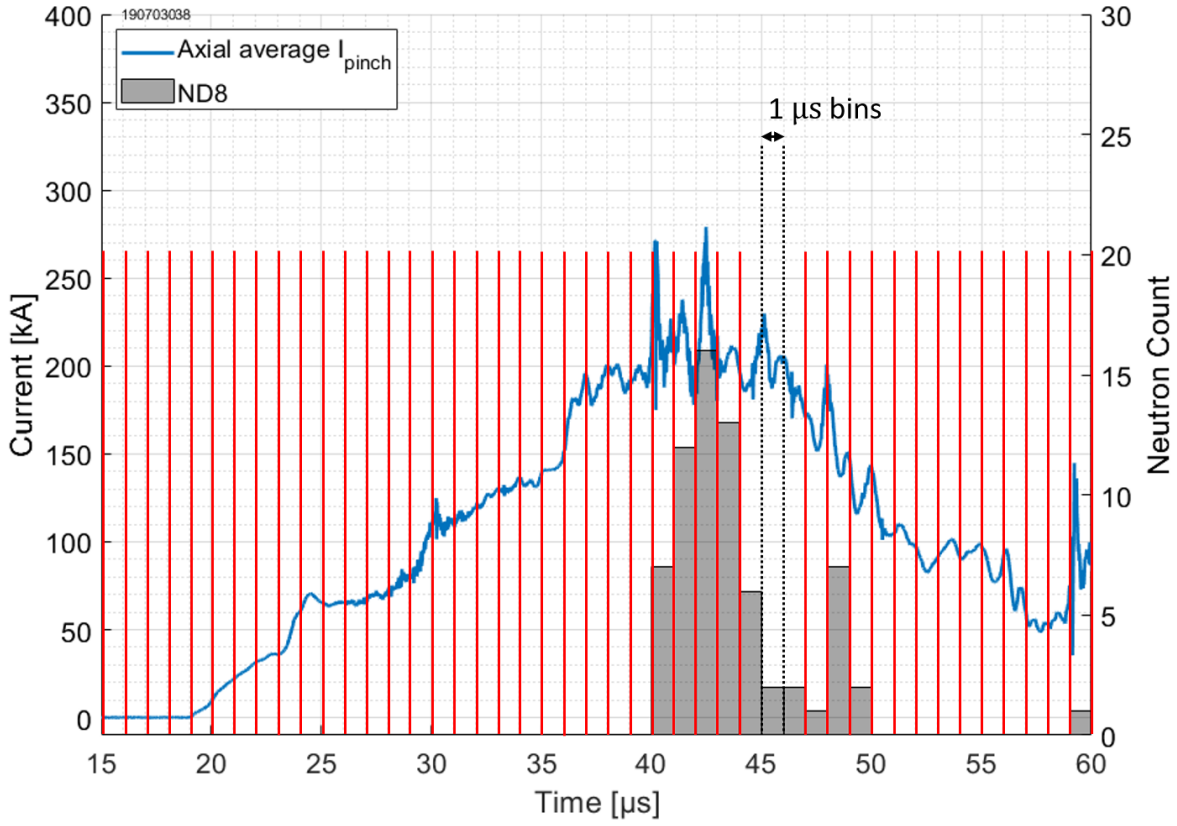

Figure 4.4: Plasma current at 15 cm and neutron counts for one plasma pulse with representative 1 µs bins.

4.3 Scaling of yield with measured instantaneous Z-pinch current

The scaling of neutron counts with current is obtained from a Deming regression [58] of the logarithm of the neutron count plotted against the logarithm of the average current for each bin. The slope of a linear regression is the scaling exponent n in the relationship $y = x^n + K$, where K is a constant.

A Deming regression is used with a coefficient $\lambda = \sigma_y^2/\sigma_x^2$ set to unity. This coefficient relates the variance of the y measurements (σ_y^2), neutron counts, to the variance of x measurements (σ_x^2), the pinch current. When $\lambda = 1$, the Deming regression is equivalent to an orthogonal regression, minimizing the perpendicular distance to a linear fit.

The Deming regression is used because uncertainties are present in the measurements of both the x axis quantities and the y axis quantities. Setting $\lambda = 1$ assumes that the errors of both measurements are equal. A more accurate treatment would take into account the error at each data point, which would require a more complex fitting algorithm.

The data shown in Fig. 4.5 are from a set of 70 pulses at 5 kV using all 9 gas valves. Each pulse is subdivided in 1 µs bin. The neutron counts from ND8 are used. The current is an axial average of the current signal obtained at each 5 cm between 0 and 30 cm. This average current is based on the finding in [36] that the neutrons are emitted over a cylindrical volume spanning 30 cm and centered at 15 cm.

The fitting shown in Fig. 4.5 is repeated for ND4 placed at 80 cm and for bin widths of 0.5, 1, 2, 5, and 10 µs. The results are shown in Fig. 4.6. The fitting is also performed using the current at each axial location instead of an axial average. The resulting scaling is shown for a bin size of 0.5 and 5 µs in Fig. 4.7.

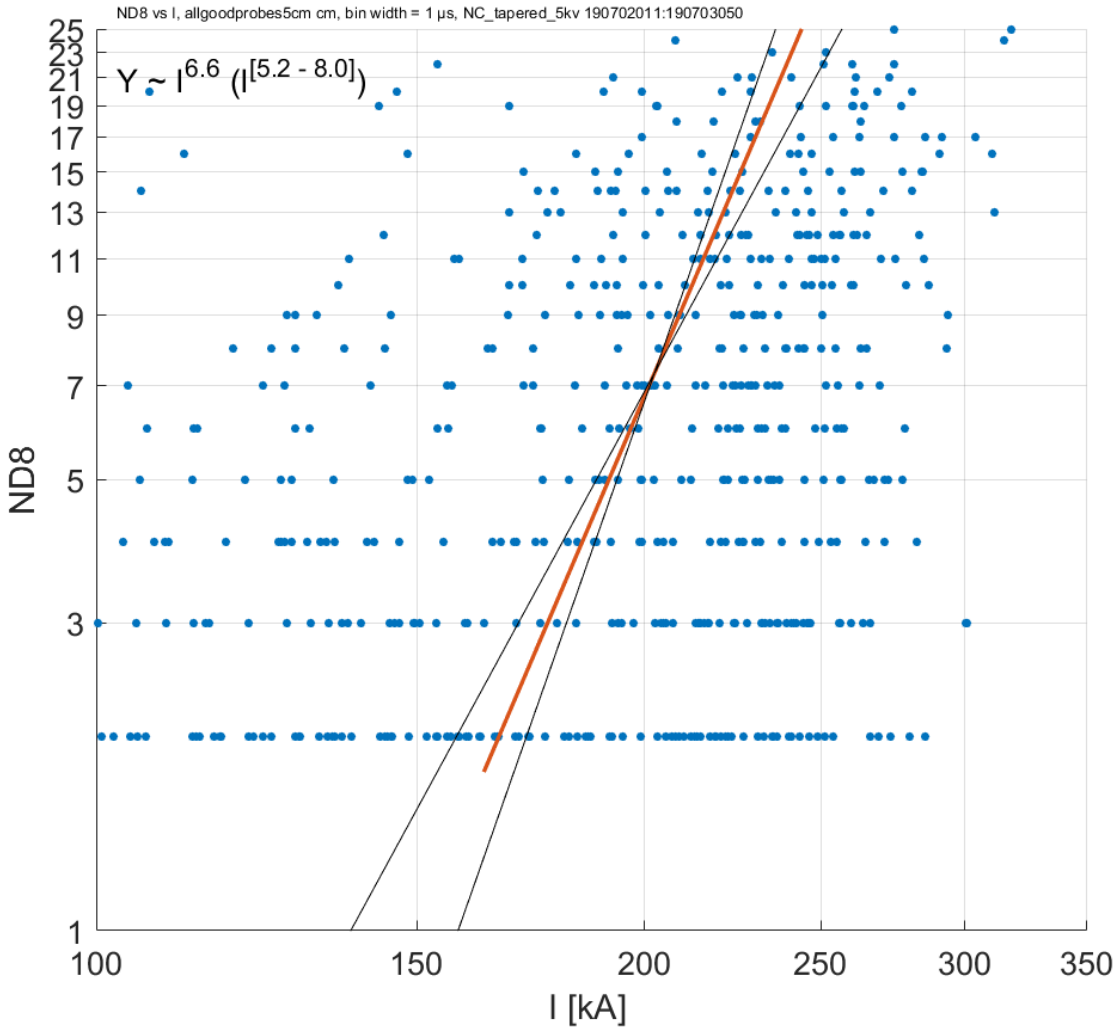

Figure 4.5: Neutron detector signal for the neutron detector 8 (ND8) located 40 cm from the axis and the axial averaged current between 0 and 30 cm. A time bin of 1 µs is used. The 95% confidence intervals for the slope are shown. The scaling shows $Y \propto I^{6.6}$ with a 95% confidence interval of $Y \propto I^{5.2}$ to $Y \propto I^{8.0}$.

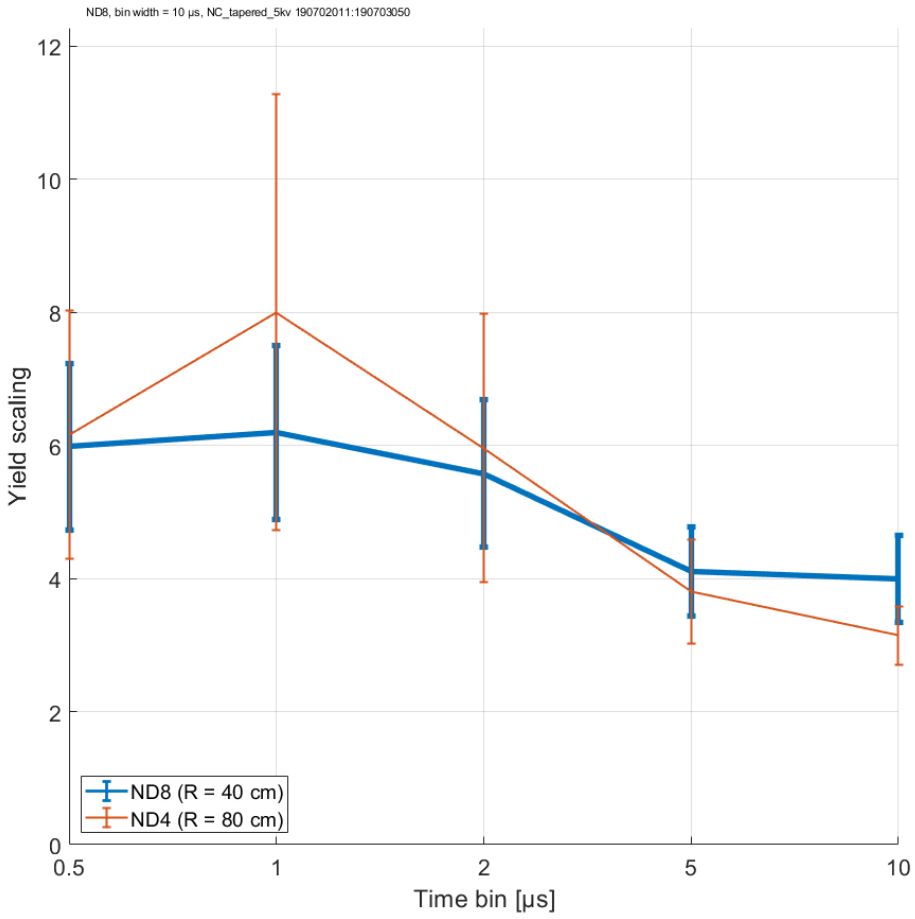

Figure 4.6: Exponent n from $Y \propto I^n$ evolution for different time bins. The error bars indicate a 95% confidence interval on the slope of the linear regression. The exponents calculated from detector ND8 and ND4 located at 40 cm and 80 cm are in agreement. The scaling is found to decrease with increasing bin size, indicating that the current local maxima play a role in the neutron generation.

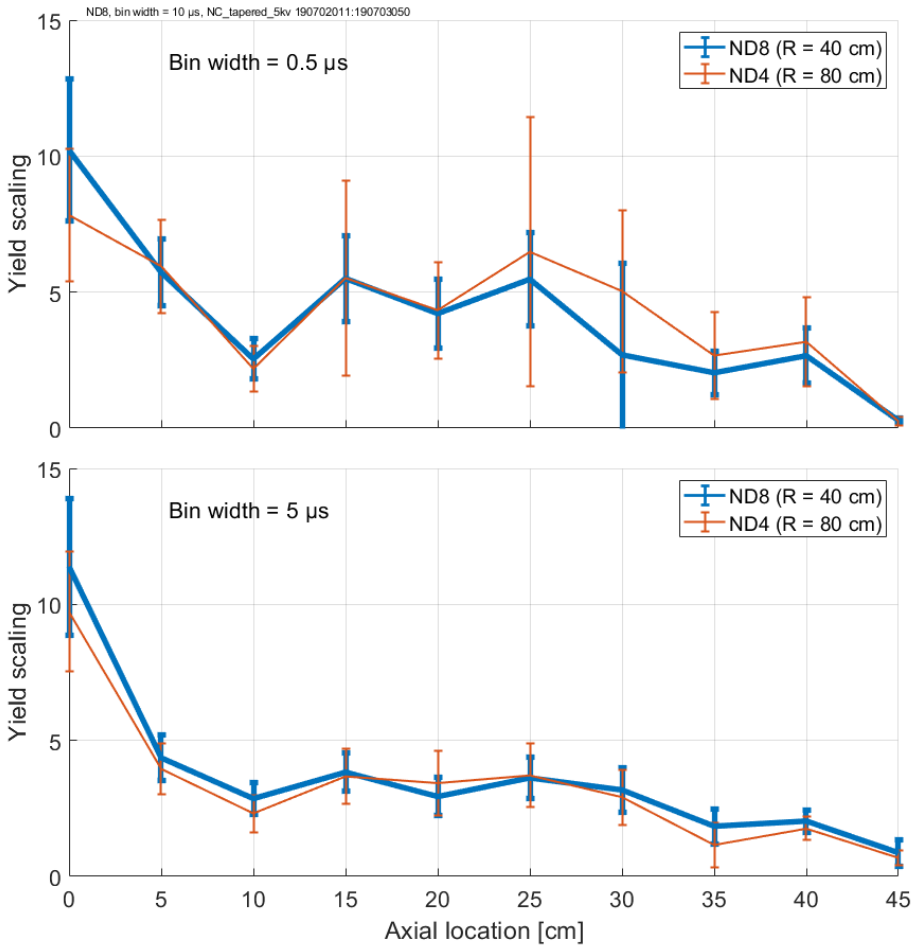

Figure 4.7: Exponent n from $Y \propto I^n$ evolution for different current axial locations. The error bars indicate a 95% confidence interval on the slope of the Deming linear regression. A bin width of 0.5 µs is used for the top plot and a bin width of 5 µs is used for the bottom plot. The scaling is found to decrease with axial location and increasing bin size.

4.4 Analysis

Figure 4.5 shows a scaling of $Y \propto I^{6.6\pm1.4}$. Chapter 3 showed that plasma is piling up against the end wall, creating a stagnation shock that increases the linear density. Moreover, following the frozen-in flux condition, that shock increases the magnetic field, and therefore the plasma current, by the same factor as the stagnating background density. This stagnating plasma could increase the pinch linear density. For example, for a linear density increasing proportionally with the axial current ($N \propto I$), Eq. (4.3) becomes

$$Y \propto l\tau I^{6.5} \tag{4.4}$$

This adiabatic scaling relation agrees with the measured scaling relation for the average current and is consistent with the finding from Chap. 3 that the magnetic field and the average plasma density increase across the stagnation shock.

Figure 4.6 shows the yield scaling as a function of the width of the time bin. First, the scaling exponents calculated from the neutron detector at 40 cm and the neutron detector at 80 cm are in agreement. The error bars from the detector located at a smaller radius are smaller as it uses a larger dynamic range, leading to a better fit. This agreement suggests that the closer detector did not experience counting error due to pulse pileup or detector shutoff.

Second, the scaling is shown to decrease as the bin size increases. A large bin size smooths the current peaks, where high current could potentially be associated with a large time-localized yield. If the current maxima did not play a role in the neutron yield, the large bin scaling would agree with the small bin scaling relationship. The observed disagreement suggests that neutrons are generated during current maxima.

Figure 4.7 shows the yield scaling using current at each axial location instead of the average current used for Fig. 4.6 for a bin width of 0.5 µs and 1 µs. The scaling is steeper when compared to the current closer to the nose cone ($z = 0$ cm) and decreases when compared with current downstream. The current near the nose cone has a disproportionately large effect on the total yield compared to the current downstream. The scaling calculated from

the current measured at 0 cm seems to follow the I^{11} relationship expected for an adiabatic Z-pinch evolution with a constant linear density.

Moreover, the neutron yield scaling has a net decrease downstream of 30 cm. This increased scaling with locally measured current could be related to the neutron axial origin. The decrease after 30 cm would be in agreement with [36] where the neutron source was found to be extending from the nose cone to approximately $z = 30$ cm, assuming a uniform line source.

4.5 Conclusion

This chapter showed that it was possible to obtain a scaling of the yield with current by using the time-resolved neutron measurements in combination with the time-resolved current measurements. A scaling of approximately I^7 is obtained, in agreement with a pinch adiabatic scaling where the current increases at the same rate as the linear density.

This result could be linked with the results from Chap. 3 where it was shown that the plasma stagnation increased the linear density. In the case of FuZE and its scaling to a net gain configuration, this implies that achieving higher current through the flux compression of the stagnation wave reduces the yield scaling.

This chapter also showed that the neutrons were associated with the peak currents. In a configuration where the current varies from pulse to pulse, this implies that the yield of a plasma pulse is strongly dependent on the time evolution of its pinch current, where high currents achieved over a small period of time can have a disproportionate effect on the neutron yield. This high current can also be limited to one axial location. Therefore, the neutron yield could be both localized to a small axial location and a small time period associated with elevated currents.

Chapter 5

PLASMA ACCELERATION TERMINATION

The coaxial accelerator ionizes and accelerates plasma which ultimately forms the Z pinch. This chapter shows that the termination of the deflagration mode could be consistent with a blow-by instability. First, the coaxial accelerator line integrated density measurements are shown. The accelerator is divided in an outer and inner region and it is shown that the calculated inner density is depleted as a fast current sheet passes the measurement location. Then, this inner depletion and the corresponding increase in outer density is shown to be consistent with a blow-by event, moving plasma from the inner to the outer electrode until radial force balance is reached.

5.1 Plasma acceleration processes

The coaxial accelerator accelerates plasma through its radial currents. The presence of radial currents are seen from the gradient in the axial current contours shown in Fig. 5.1. The FuZE experiment initially accelerates plasma through a snowplow process which then transitions to a deflagration mode [9]. This transition process is observed in other plasma coaxial accelerators [49, 59] and is governed by the Rankine-Hugoniot relations [48]. This differentiates the FuZE experiment from dense plasma foci (DPF) [19] where the coaxial phase of Z-pinch formation for neutron or X-ray production relies on the transient snowplow process. The ideal acceleration mechanism for FuZE relies on a quasi-steady state process of deflagration [17], process more akin to magnetoplasmadynamic thrusters [60].

At present, the FuZE acceleration lifetime is limited by two factors: the finite length of the current impulse and the finite amount of neutral gas that can be injected. By tracking the location of the radial current sheet, it is possible to identify the different modes of acceleration

present throughout the pinch lifetime. An example of spatiotemporal measurement of radial current is shown in Fig. 5.1.

The blow-by instability can occur in a coaxial accelerator when the current sheet near the inner electrode overtakes the current sheet at higher radius, near the outer electrode. When such an event occurs, the current density develops a large axial component, J_z, that accelerates plasma with $J_z B_\theta \ \hat{r}$. If this effect is sufficiently strong, the radial acceleration of plasma further depletes the density near the inner electrode, increasing the speed of the inner portion of the current sheet and leading to a runaway effect.

The inner portion of the current sheet eventually overtakes the outer portion due to the $1/r$ dependence of both the current sheet current density and the magnetic field in a coaxial system, leading to an axial acceleration force $F_z \propto 1/r^2$.

A previous study [61] found that increasing the mass near the inner electrode with $\rho = Cr^{-n}$ for $n > 2$ helped to delay the blow-by instability, where ρ is the plasma density and C is a constant. This effectively amounts to a density profile peaked at the inner electrode. The focus of this study was on the occurrence of blow-by during the snowplow portion of the acceleration. In FuZE, the blow-by could be triggered at the end of the deflagration period. Moreover, the Hall effect on FuZE is helping to maintain a finite inner density. From the generalized Ohm's law with zero resistivity, zero electric field, and zero pressure gradient, the radial velocity created by the Hall effect is given by

$$\vec{v} \times \vec{B} = \frac{\vec{J} \times \vec{B}}{ne} \tag{5.1}$$

$$v_r B_\theta = \frac{J_r B_\theta}{ne} \hat{r} \tag{5.2}$$

$$v_r = \frac{J_r}{ne} \hat{r} \tag{5.3}$$

assuming that J_r is purely radial. The direction of the radial velocity is the same as the current density, which in the case of a cathode inner electrode, is toward the inner electrode. This effect will contribute in creating a density profile peaked toward the inner electrode, contributing in delaying or preventing the blow-by phenomenon in the first part of the acceleration.

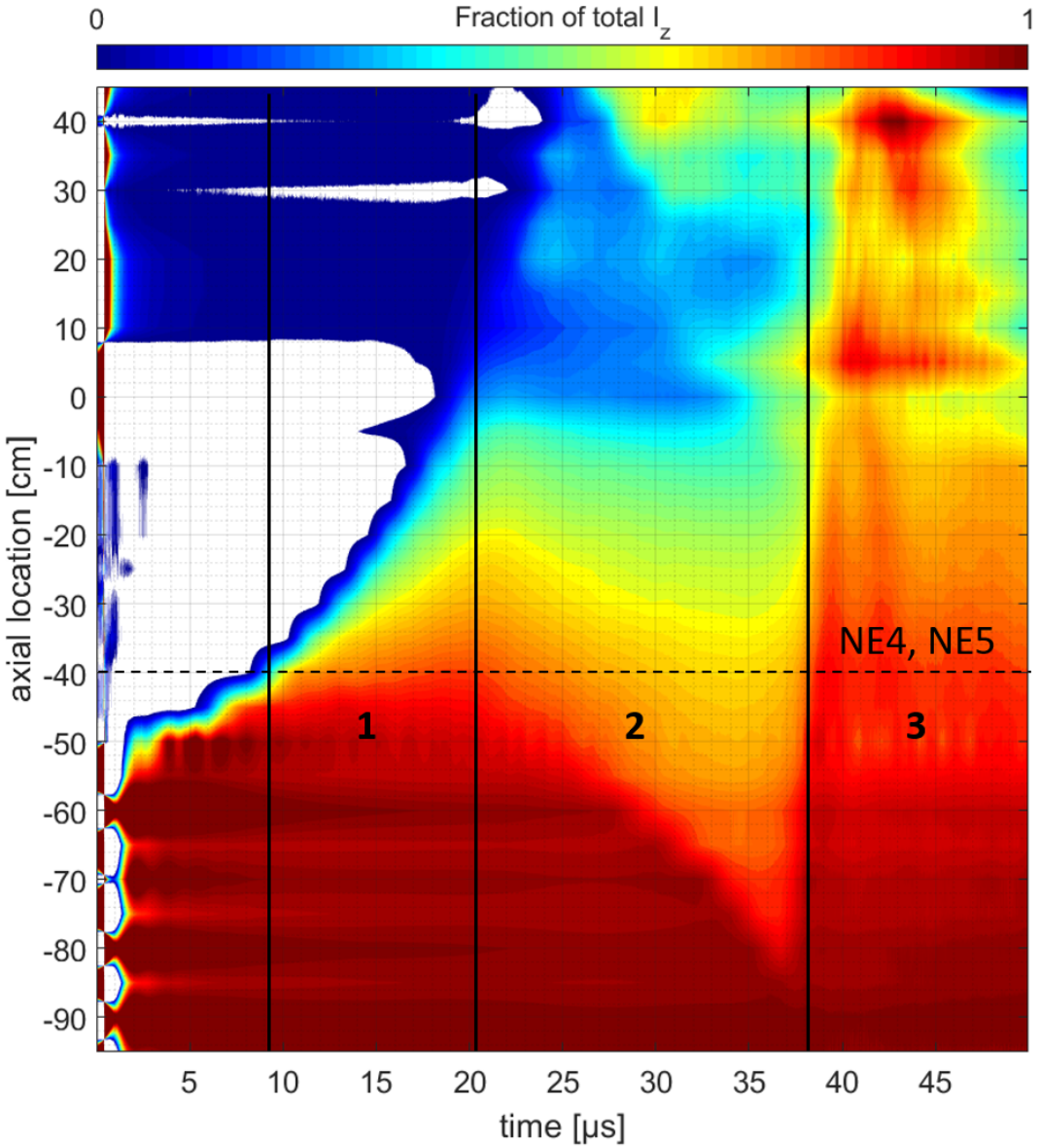

Figure 5.1: Average contours of axial current in the FuZE experiment generated by the process summarized by Fig. 1.8. The gradients in axial current are the radial currents that determines the coaxial acceleration mechanism. Three regions are identified: (1) initial snowplow acceleration process and stationary deflagration, (2) deflagration with radial current front moving towards the breech end of the coaxial accelerator, and (3) acceleration termination.

The blow-by instability has also been studied in the context of compact toroid acceleration [62]. In that context, the instability takes place when the magnetic field pushing the toroid becomes greater than the toroid internal pressure [63]. Contrary to the compact toroid case, no externally applied field is present in the FuZE acceleration region. The plasma internal pressure is therefore not directly controllable and is initially much smaller than the applied magnetic pressure.

5.2 Accelerator density and radial current measurements

Two density chords record line integrated density in the coaxial accelerator region at $z = -40$ cm. A cross section schematic of the density chord "NE4" and "NE5" is shown in Fig. 5.2. The chords are placed at two different heights, allowing to distinguish between an inner density region and an outer density region.

The average number density data is shown in Fig. 5.3 for NE4 and in Fig. 5.4 for NE5. The Lissajous radius is shown for each signal. This radius is a measure of the signal quality obtained from the digitized phase information from the interferometer. The digitized signals are $A\cos(\theta)$ and $A\sin(\theta)$, where θ is the phase difference between the reference beam and the scene beam and A is the signal amplitude. The Lissajous radius is defined as the signal amplitude, which is the radius of the circle defined by the two signals.

$$R_{Lissajous} = \sqrt{A^2\cos^2\theta + A^2\sin^2\theta} = A. \tag{5.4}$$

At a repeatable time, the radius of the Lissajous goes near zero and the density data is no longer physical. That time is indicated by a black dashed line, followed by a gray region. In the case of NE5, the radius goes to zero, recovers, then ultimately shuts down.

The snowplow is indicated by the initial peak in density, corresponding to the leading edge of the current sheet at approximately 9 µs. After the initial snowplow, a deflagration period sets in as the current sheet widens (region 1). As the current sheet starts moving back (region 2), the density rises to about twice its previous value.

As the current sheet starts moving back, the velocity at $z = -40$ cm, u_{n40}, is expected

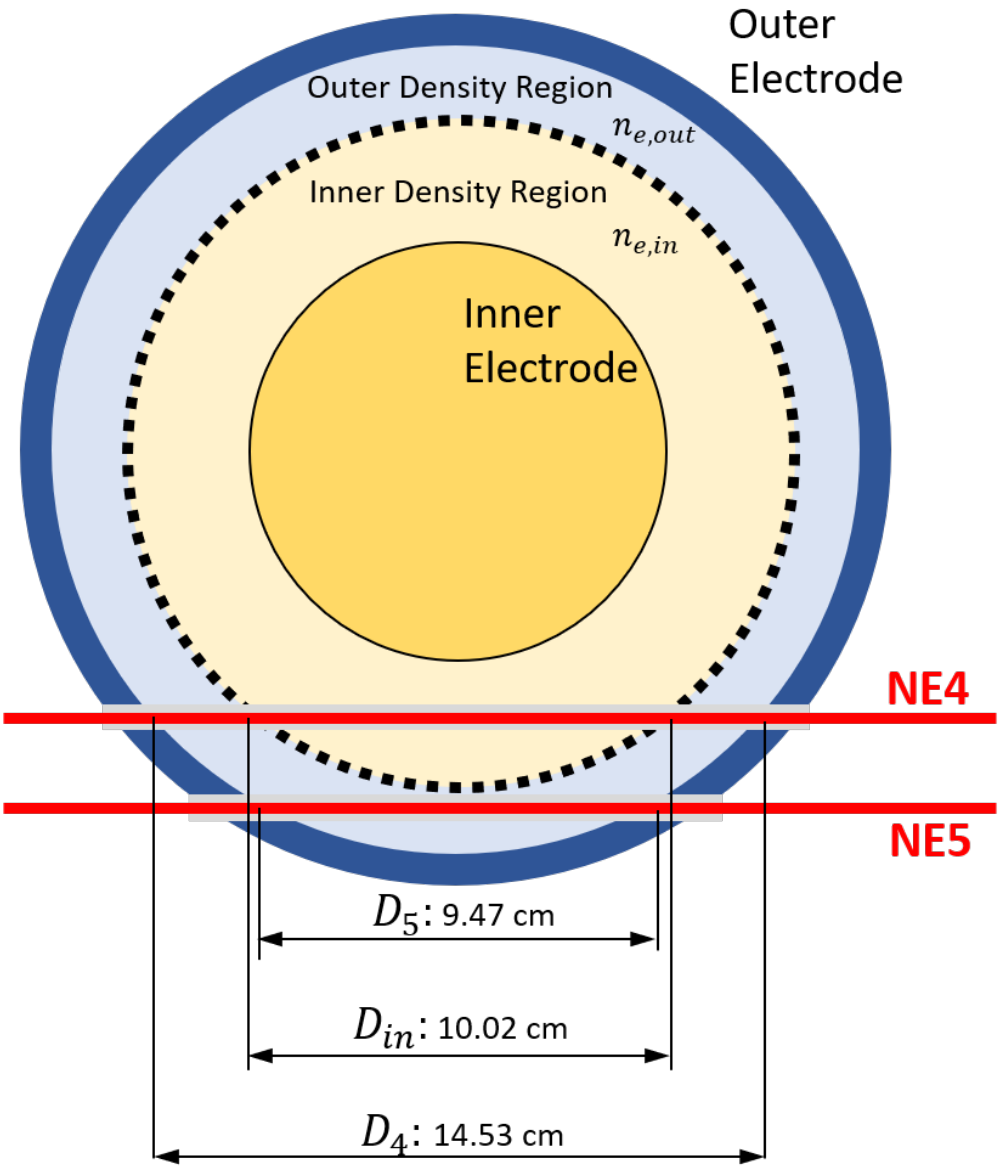

Figure 5.2: Cross section of the accelerator region at $z = -40$ cm. The path of the two interferometry chords, NE4 and NE5, are identified in red. From the two chords, an inner density is obtained while the outer density is given directly by NE5. The different path lengths used for the calculation of the inner density are identified.

to increase as it is now further downstream from the start of the deflagration process. Both the density ρ_{n40} and the plasma axial velocity u_{n40} increase at the same time, therefore the accelerator mass flow $\dot{m}_{n40} = \rho_{n40} u_{n40}$ must increase during the deflagration period. This mass flow increase should also be accompanied by an increase of neutral gas ionization. For a uniform gas fill in the accelerator, the increased ionization rate is visible by the steepening of the backward traveling deflagration front in Fig. 5.1.

From chords 4 and 5, the density of the inner portion of the accelerator is obtained. Chord 4 goes through both the inner and outer regions, as identified in Fig. 5.2. Chord 5 only travels through the outer region, defining an average outer density as

$$n_{e,out} = \frac{NE_5}{D_5} \tag{5.5}$$

where NE_5 is the measured line-integrated density and D_5 is the path length through the accelerator traveled by chord 5. The inner density can then be calculated by removing the contribution of the outer density from chord 4

$$n_{e,in} = \frac{NE_4 - NE_{4,out}}{D_{in}} \tag{5.6}$$

$$= \frac{NE_4 - n_{e,out}\left(D_4 - D_{in}\right)}{D_{in}} \tag{5.7}$$

where the lengths D_i are given in Fig. 5.2 and $NE_{4,out}$ is the contribution to NE4 from the outer density. The calculated inner density is shown in Fig. 5.5.

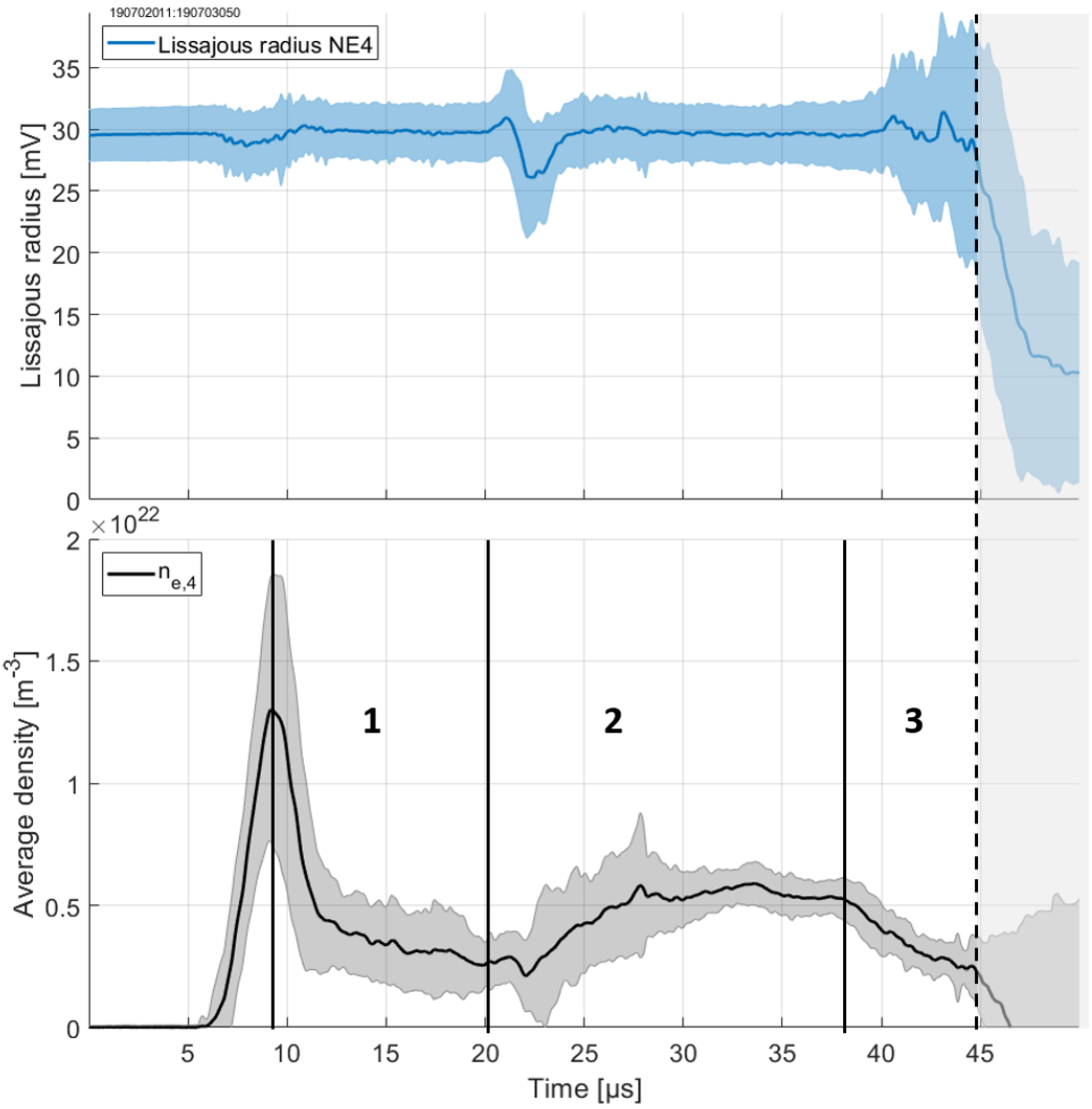

Figure 5.3: Lissajous radius of the interferometer chord 4 (NE4) and average accelerator density. The three regions of Fig. 5.1 are identified: (1) initial snowplow and stationary deflagration, (2) deflagration with radial current front moving towards the breech end of the coaxial accelerator, and (3) acceleration termination. A grayed region starting at the dashed line highlights the time span where the Lissajous radius decreases to a small value and where the signal analysis algorithm fails.

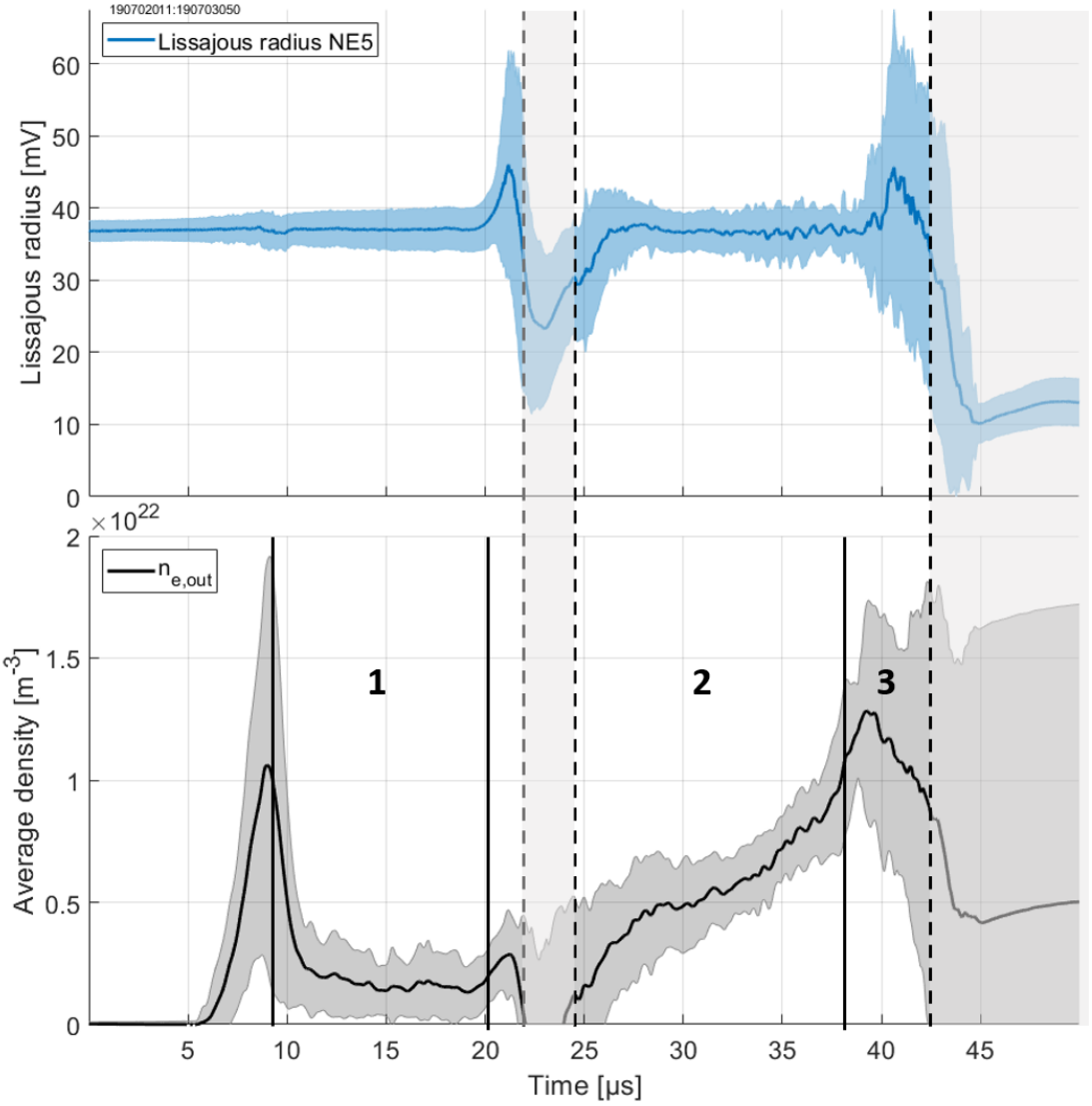

Figure 5.4: Lissajous radius of the interferometer chord 5 (NE5) and average accelerator outer density. The three regions of Fig. 5.1 are identified: (1) initial snowplow and stationary deflagration, (2) deflagration with radial current front moving towards the breech end of the coaxial accelerator, and (3) acceleration termination. Two grayed regions delimited by the vertical dashed lines highlight the time spans where the Lissajous radius decrease to a small value and where the signal analysis algorithm fails.

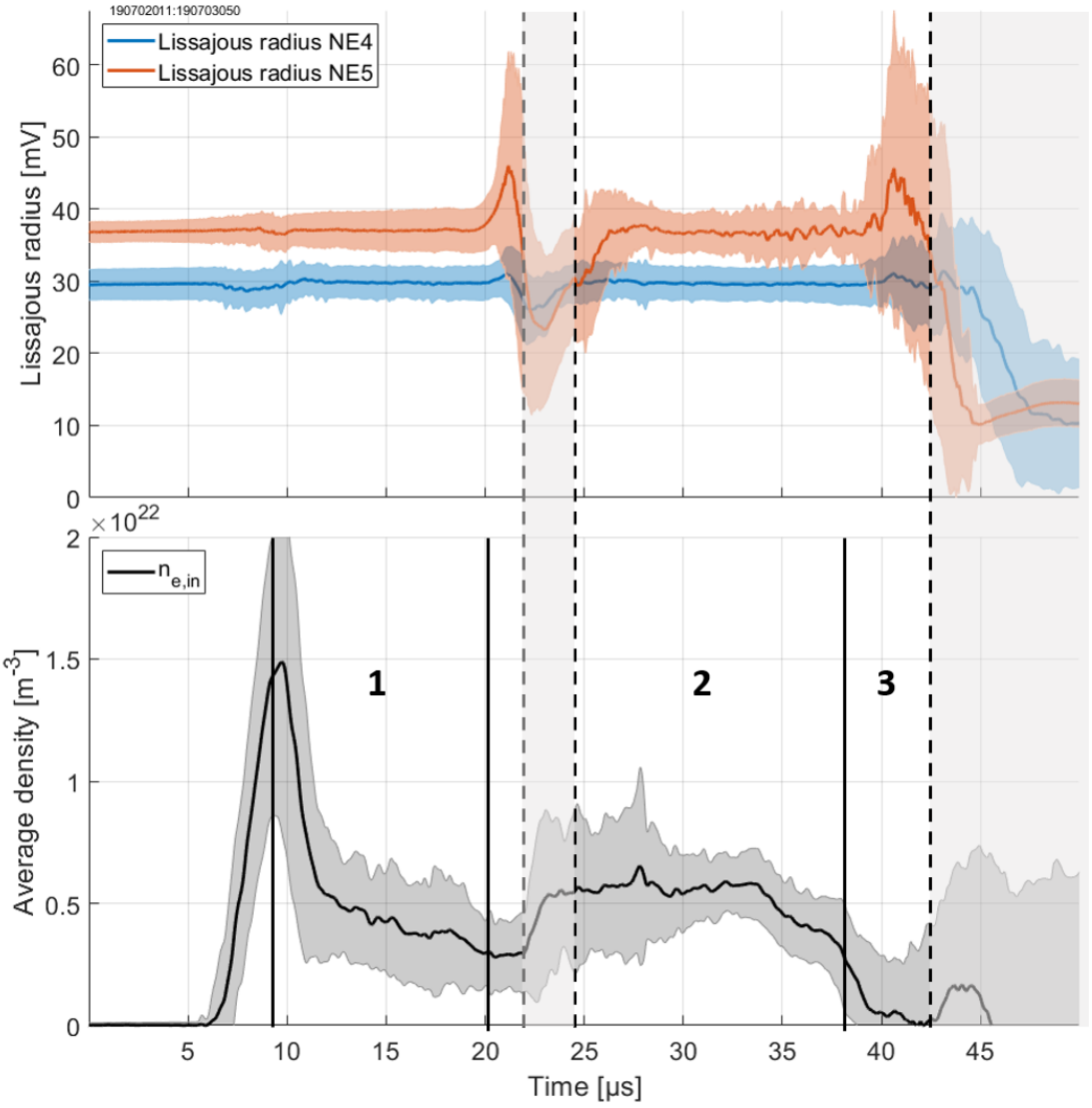

Figure 5.5: Lissajous radius of the interferometer chord 4 and 5 (NE4 and NE5) and average accelerator inner density calculated from Eq. (5.7). The three regions of Fig. 5.1 are identified: (1) initial snowplow and stationary deflagration, (2) deflagration with radial current front moving towards the breech end of the coaxial accelerator, and (3) acceleration termination. Two grayed regions delimited by the vertical dashed lines highlight the time spans where the Lissajous radius decrease to a small value and where the signal analysis algorithm fails.

5.3 Evidence of a blow-by process

Figure 5.5 shows the density signal in the inner portion of the accelerator. Its temporal evolution is similar to chord 4 up to region 3 where the average signal decreases to nearly zero. This depletion of inner density is coincident with the passing of the fast forward-moving current wave seen in Fig. 5.1 and defining region 3. Moreover, a simultaneous increase of outer density is seen in Fig. 5.4. A current wave traveling at high velocity and depleting the density near the inner electrode to transfer it at higher radius is consistent with a blow-by instability.

According to Fig. 5.1, the most upstream location reached by the deflagration current sheet is approximately $z = -85$ cm. The coaxial accelerator has an alumina insulator encasing the inner electrode and extending to $z = -87$ cm. Disassembly of the accelerator after operating the experiment for thousands of pulses showed substantial electrode erosion at the junction of the insulator and inner electrode, shown in Fig. 5.6.

There is likely to be a reservoir of neutral gas upstream of the insulator-inner electrode junction. However, as soon as the current sheet reaches the alumina insulator, it can no longer move back at the inner electrode attachment point. This creates a stationary current contact that quickly depletes the neutral gas at the inner electrode. The outer electrode current sheet can still move further upstream where neutral gas is available to ionize and a conducting surface can serve as a contact point. The localized erosion shown in Fig. 5.6 could be the sign of a stationary current sheet at the inner electrode insulator junction.

The stationary current contact at the inner electrode creates a depleted plasma region and conductivity can only be maintained by moving downstream. Meanwhile, the outer electrode current contact is maintained and can even continue ionizing neutral gas, moving toward the breech end of the accelerator. A consequence of the localized neutral gas depletion could be that the inner current contact point quickly overtakes the outer contact point, triggering a blow-by instability.

A model of a blow-by event is developed. A schematic of the model is presented in

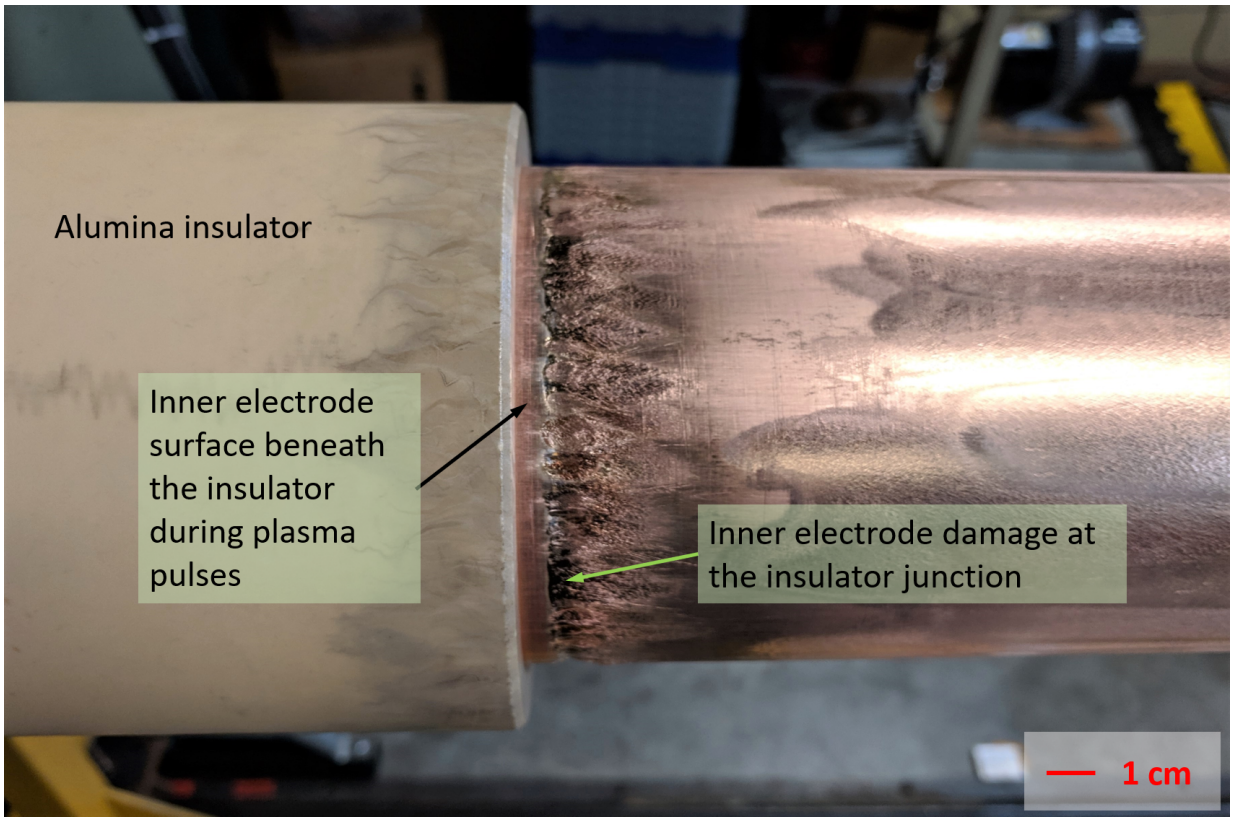

Figure 5.6: Photograph of the location of the junction between the inner electrode and the beginning of the alumina insulator at the breech end of the coaxial accelerator. The insulator is moved back by a few millimeters, revealing the pristine copper previously covered (black arrow). The location of the junction is clearly marked by darker copper damage at the junction of the insulator and inner electrode (green arrow). The copper is damaged by pits that are a few mm deep and could be an indication of a stationary radial current contact, leading to a blow-by process from the localized depletion of neutral gas at the inner electrode.

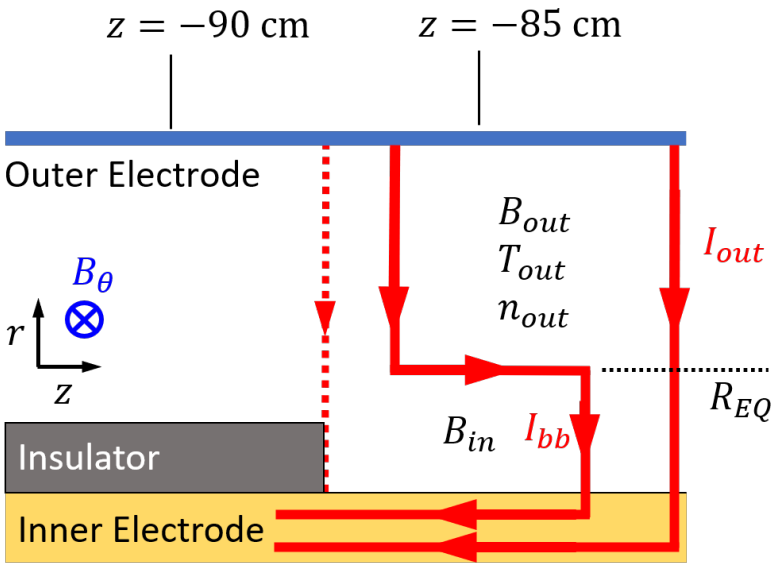

Figure 5.7: Currents near the insulator at the onset of the blow-by instability. The current sheet with I_{bb} current pushes the plasma away from the inner electrode up to a radius R_{EQ} where the plasma magnetic and thermal pressures, $B_{out}^2/2\mu_0 + n_{out}k_BT_{out}$ balance the pressure from the blow-by current sheet, $B_{in}^2/2\mu_0$. As the plasma density goes to zero, a fixed blow-by current I_{bb} would expand and connect to the outer electrode, joining I_{out}.

Fig. 5.7. Assuming that the density near the inner electrode is zero, an equilibrium radius, R_{EQ}, calculated. This radius indicates the radial location at which an infinitely thin blow-by current sheet would push the accelerator density, separating an empty inner region and an outer region containing plasma. At this radius, the pressure between the plasma pushed against the outer electrode is equal to the pressure from the blow-by current sheet,

$$\frac{B_{out}^2}{2\mu_0} + n_{out}k_BT_{out} = \frac{B_{in}^2}{2\mu_0} \tag{5.8}$$

where the subscript "out" indicates the properties of the outer plasma and the subscript "in" indicates the properties of the evacuated region, near the inner electrode. The magnetic

fields at the equilibrium radius are given by Ampère's law

$$B_{out} = \frac{\mu_0 I_{out}}{2\pi R_{EQ}} \tag{5.9}$$

$$B_{in} = \frac{\mu_0 \left(I_{out} + I_{bb}\right)}{2\pi R_{EQ}} \tag{5.10}$$

where I_{bb} is the current in the blow-by current sheet and R_{EQ} is the equilibrium radius. An equation for R_{EQ} is obtained using Eqs. 5.8, 5.9, and 5.10.

$$R_{EQ} = \frac{\mu_0}{8\pi^2 e} \frac{I_{bb}^2 + I_{bb} I_{out}}{n_{out} T_{out}} \tag{5.11}$$

where e is the elementary charge and T_{out} is in eV. The blow-by current I_{bb} at $z = -40$ cm is taken to be the current jump at the beginning of region 3 while the current I_{out} is the taken just before the jump, shown in Fig. 5.8. The density n_{out} is taken from the average peak measurement in Fig. 5.4 at the start of region 3. The equilibrium radius is calculated with Eq. (5.11) using a range of temperature T_{out} and is shown in Fig. 5.9.

The equilibrium radius shows that the compressed plasma temperature is between 35 and 50 eV in region 3. This temperature corresponds to an adiabatic expansion to 20 to 28 eV when the plasma fills the complete accelerator area.

For the blow-by process to be completely suppressed, the plasma density and temperature need to be sufficiently high to force the equilibrium radius to be less than the inner electrode radius. With the inner electrode radius of 5.08 cm, and a plasma temperature of 20 eV, the required accelerator density to suppress the blow-by instability according to Eq. (5.11) is $6 \times 10^{22} \mathrm{m}^{-3}$, which is approximately one order of magnitude higher than the average accelerator density given by Fig. 5.3. This approach is analogous to the acceleration of compact toroids where the internal energy of the plasma was increased by applied magnetic fields [63] instead of increased particle density in order to prevent the blow-by instability. In the case of FuZE, the internal energy is the sum of the embedded magnetic field and the thermal pressure.

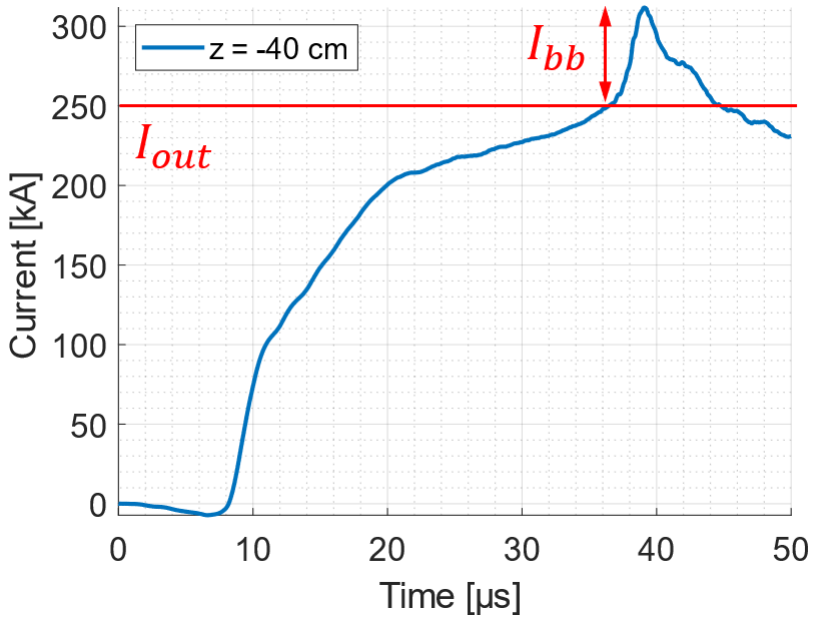

Figure 5.8: Axial current at $z = -40$ cm where the values of I_{bb} and I_{out} are measured.

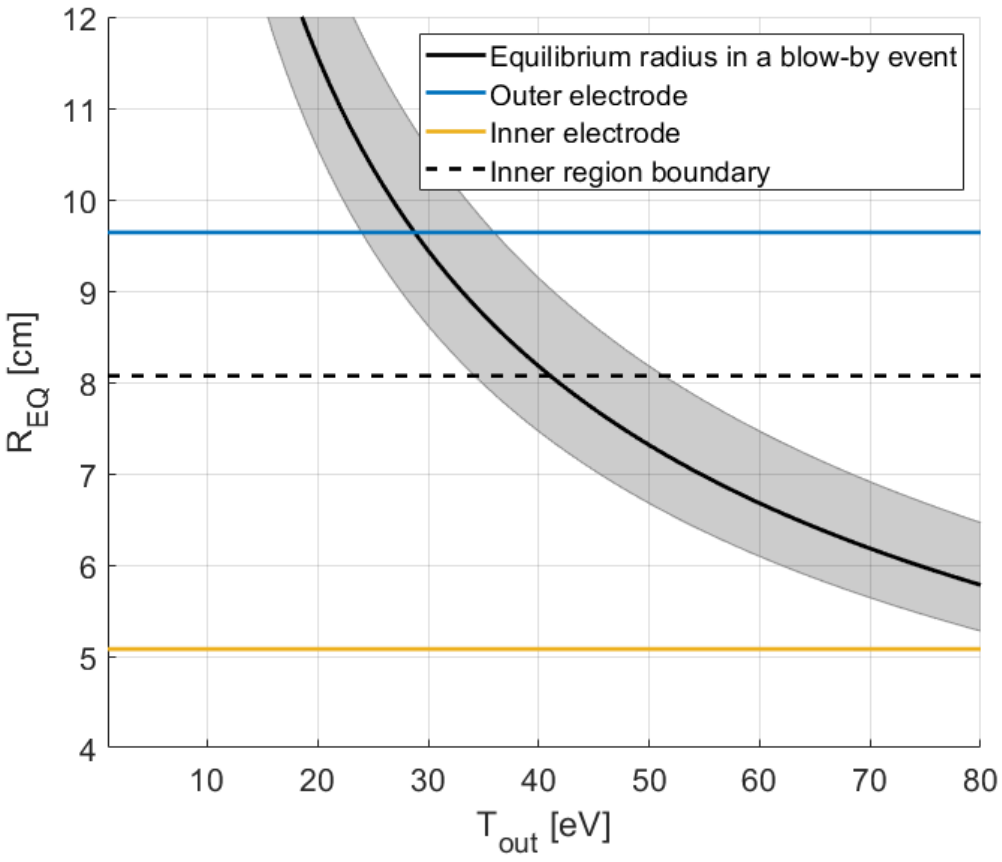

Figure 5.9: Equilibrium radius calculated from Eq. (5.11) using density from Fig. 5.4 and currents from Fig. 5.8. The location of the inner electrode and outer electrode is shown by the yellow line and blue line, respectively. The inner region boundary separating the inner and outer densities, shown in Fig. 5.2, is shown by a dashed line. A plasma compressed against the outer electrode by a blow-by event needs a temperature between 35 and 50 eV to achieve an equilibrium with the outward radial pressure of the blow-by current sheet at a radius equal to the inner region boundary.

5.4 Conclusion

This chapter showed that the fast current sheet coincident with an inner density depletion and an outer density increase could be consistent with a blow-by instability. A blow-by instability could occur when the inner current sheet reaches the inner insulator. A radial equilibrium model shows that the radius reached by a blow-by current sheet is consistent with an average accelerator temperature of 20 to 28 eV.

The end of the plasma acceleration, potentially explained by the presence of a blow-by event, can be avoided by providing a sufficient neutral gas supply matching the ionization rate of the deflagration wave. In that configuration, the current sheet would never reach the inner insulator. In the FuZE device, the depletion of neutral gas in the accelerator is responsible for the rapid change in the current path and the termination of the plasma source which eventually lead to the Z-pinch current interruption.

Chapter 6

CONCLUSION

The spatiotemporal evolution of the magnetic field presented in Fig. 1.8 showed traveling structures along the length of the coaxial accelerator to the end of the assembly region, both traveling against and with the direction of the plasma flow. This detail motivated the investigation of the axial evolution of the FuZE plasma as the structures were found to be coincident with important pinch phenomena, such as velocity shear direction change, plasma current magnitude increase, and plasma acceleration process termination. The investigation presented here elucidated a causal dependence of several processes that explain the magnetic field signature seen in the contour plots.

First, plasma is ionized in the coaxial accelerator. A deflagration wave forms, which then continuously ionizes and accelerates plasma downstream in the Z-pinch region. The accelerated plasma eventually reaches the end of the outer electrode, capped by a conductive end wall. The Z-pinch current connects to the end wall and returns through the outer electrode, encapsulating the magnetic flux inside the assembly region. The assembly region plasma is hot enough and the axial velocities are high enough that the magnetic field diffuses much more slowly out of the plasma than the plasma moves, linking the movement of the plasma to the magnetic field.

The plasma initially accelerated by the coaxial accelerator impacts the end wall with a force proportional to the sum of its ram, thermal, and magnetic pressures. However, as the plasma expands through the end wall gaps, the magnetic field forms a radius of curvature limited by the spokes, unable to diffuse fast enough through them. Large ram and thermal pressures compared to the magnetic field pressure allow plasma to pass through the end wall and expand beyond its downstream face, where the radius of curvature is no longer

limited by any obstacle and where reconnections, diffusion, or demagnetization can take place. However, if the ram and thermal pressures are low enough, an axial equilibrium is formed and plasma is axially confined, unable to exit the Z-pinch assembly region in large quantity.

As a consequence, plasma starts to stagnate against the end wall, piling up and moving the stagnation front against the plasma flow, as plasma is still accelerated from the plasma gun. This forms a perpendicular shock in the background plasma, increasing the linear density while also increasing the axial current, as the frozen in flux condition is still satisfied. This stagnation wave, however, is only present in the background density. The hot Z pinch continuously flows and eventually interacts with the end wall.

The hot, flowing, Z-pinch core is gradually slowed down at larger radii where the velocity meets the background stagnated plasma. The interaction of the Z pinch with the end wall and the background plasma changes the sheared flow profile from hollow to peaked. However, this interaction is not solely due to viscous diffusion between the flowing and stagnated plasma populations.

Thanks in part to the current induced through the stagnation shock, the Z pinch is now compressed to a high enough temperature and density such that some collisions between deuterium ions lead to neutron emitting D-D nuclear fusion reactions. The scaling indicates that the neutron emission is proportional to an adiabatic Z-pinch compression where the linear density increases proportionally with the current.

The pinch can stay in this neutron generating state as long as sheared flow is present, and as long as the pinch plasma is replenished by the coaxial accelerator. While this succession of plasma axial stagnation and radial compression takes place in the assembly region, the deflagration wave approaches the breech end of the coaxial accelerator, ionizing and accelerating the neutral gas previously injected.

The inner portion of the deflagration current sheet reaches the insulator wrapped around the inner electrode, where it depletes the supply of neutral gas. This depletion leads to the termination of the continuous acceleration of plasma, which could be explained by a blow-by

instability.

In summary, the FuZE device axial evolution generates a reflected plasma wave that increases the linear plasma density, potentially reducing the yield scaling with pinch current. The Z pinch is disrupted when insufficient plasma is present in the assembly region, or when it becomes unstable due to insufficient sheared-flow stabilization. These disruptions could be due to the coaxial accelerator injecting too little plasma in the assembly region, a process started when the current sheet reaches the inner alumina insulator, potentially triggering a blow-by instability.

These results are in no way an immovable roadblock to the scaling of the sheared-flow-stabilized Z pinch to a net gain fusion reactor core. The stagnation shock could be a way to achieve higher axial pinch current than expected, at the cost of increased linear density. However, the stagnation shock can be avoided altogether by changing the end wall design such that larger openings are present, limiting the minimum magnetic curvature to a large value unable to contain the plasma inside the assembly region.

Moreover, the termination of the plasma acceleration can also be avoided by continuously injecting enough neutral gas at the breech end of the accelerator such that the deflagration wave stays at one axial location. Moving the alumina insulator along the outer electrode could also delay the formation of a blow-by instability.

The axial evolution of the sheared-flow-stabilized Z pinch will only get more important as new constraints related to a fusion reactor application are considered, such as plasma material interaction. Crucially, an eventual space propulsion engine would need to allow a complete plasma axial exhaust to achieve the maximum thrust and efficiency.

Chapter 7

FUTURE WORK

The end wall results showed how changing the geometry only subtly changed the plasma parameters. Two extreme cases could be tested to better understand the role of the end wall: a completely opaque end wall, and no end wall at all. First, the comparison with the completely plain end wall would inform us on how much plasma is being exhausted from the spoked end wall. Then, pulses without an end wall could show how much of the pinch property evolution is due to the plasma stagnation wave.

Moreover, plasma stagnating through the assembly region can also expand and exhaust through the azimuthal diagnostic slots. These slots were fitted with a copper mesh and a comparison of plasma stagnation with and without the mesh could be done. In particular, there might be a visible line integrated density increase with the mesh present as the background plasma would be prevented from expanding at radii greater than the outer electrode radius.

The assembly region plasma stagnation could be better understood if time-resolved measurements of the assembly region density profiles were available. This would help understand how much the Z-pinch core linear density is increasing compared to the background density. Then, with a known density profile time evolution and with the current measurements, the neutron scaling could be measured and the hypothesis proposed in Chap. 4 about the increasing linear density in the pinch could be fully tested.

The neutron scaling analysis presented in this thesis could be improved by simultaneously using detectors placed with a large radius difference between them. This would increase the total range of measurable yield, decreasing the uncertainty in the neutron scaling analysis. Moreover, the scaling analysis showed a possible link between current location and yield.

It would be possible to calculate a time resolved neutron centroid using multiple detectors placed in close proximity to the machine axis. This analysis would show if the centroid moves during the neutron emission period and if it is correlated with the location of the peak currents.

Lastly, the results from the nose cone study presented in the appendix could be expanded. A correlation study between the measured temperature and measured yield could lead to a better understanding on the location of the neutron emissions. A large variation of measured velocities and temperatures through ion Doppler spectroscopy was found. Knowing that variability, repeated exposures at fewer different time points would allow a better understanding of the plasma pulse to pulse variability and the relations between the temperature, neutron yield, and current in FuZE.

BIBLIOGRAPHY

[1] M. G. Haines. Fifty years of controlled fusion research. *Plasma Physics and Controlled Fusion*, 38(5):643–656, 1996.

[2] R. Carruthers and P. A. Davenport. Observations of the instability of constricted gaseous discharges. *Proceedings of the Physical Society. Section B*, 70(1):49, 1957.

[3] M. D. Kruskal and M. Schwarzschild. Some instabilities of a completely ionized plasma. *Proceedings of the Royal Society of London. Series A. Mathematical and Physical Sciences*, 223(1154):348–360, 1954.

[4] F. Wagner, G. Becker, K. Behringer, D. Campbell, A. Eberhagen, W. Engelhardt, G. Fussmann, O. Gehre, J. Gernhardt, G. v. Gierke, et al. Regime of improved confinement and high beta in neutral-beam-heated divertor discharges of the ASDEX tokamak. *Physical Review Letters*, 49(19):1408, 1982.

[5] U. Shumlak and C. W. Hartman. Sheared flow stabilization of the m= 1 kink mode in Z pinches. *Physical Review Letters*, 75(18):3285, 1995.

[6] U. Shumlak, R. P. Golingo, B. A. Nelson, and D. J. Den Hartog. Evidence of stabilization in the Z-pinch. *Physical Review Letters*, 87(20):205005, 2001.

[7] U. Shumlak et al. The sheared-flow stabilized Z-pinch. *Fusion Science and Technology*, 61(1T):119–124, 2012.

[8] U. Shumlak, B. A. Nelson, E. L. Claveau, E. G. Forbes, R. P. Golingo, M. C. Hughes, R. J. Oberto, M. P. Ross, and T. R. Weber. Increasing plasma parameters using sheared flow stabilization of a Z-pinch. *Physics of Plasmas*, 24(5):055702, 2017.

[9] R. P. Golingo, U. Shumlak, and B. A. Nelson. Formation of a sheared flow Z pinch. *Physics of Plasmas*, 12(6):062505, 2005.

[10] E. G. Forbes, U. Shumlak, H. S. McLean, B. A. Nelson, E. L. Claveau, R. P. Golingo, D. P. Higginson, J. M. Mitrani, A. D. Stepanov, K. K. Tummel, et al. Progress toward a compact fusion reactor using the sheared-flow-stabilized Z-pinch. *Fusion Science and Technology*, 75(7):599–607, 2019.

[11] W. H. Bennett. Magnetically self-focussing streams. *Physical Review*, 45(12):890, 1934.

[12] J. P. Freidberg. Ideal magnetohydrodynamic theory of magnetic fusion systems. *Reviews of Modern Physics*, 54(3):801, 1982.

[13] P. M. Bellan, S. You, and S. C. Hsu. Simulating astrophysical jets in laboratory experiments. *Astrophysics and Space Science*, 298(1):203–209, 2005.

[14] E. B. Hooper, R. H. Bulmer, B. I. Cohen, D. N. Hill, C. T. Holcomb, B. Hudson, H. S. McLean, L. D. Pearlstein, C. A. Romero-Talamás, C. R. Sovinec, et al. Sustained spheromak physics experiment (SSPX): design and physics results. *Plasma Physics and Controlled Fusion*, 54(11):113001, 2012.

[15] J. Marshall. Performance of a hydromagnetic plasma gun. *Physics of Fluids (US)*, 3, 1960.

[16] J. Marshall. Hydromagnetic plasma gun. *Plasma Acceleration*, page 60, 1960.

[17] A. I. Morozov. Principles of coaxial (quasi) stationary plasma accelerators. *Fizika plazmy*, 16(2):131–146, 1990.

[18] F. D. Witherspoon, A. Case, S. J. Messer, R. Bomgardner, M. W. Phillips, S. Brockington, and R. Elton. A contoured gap coaxial plasma gun with injected plasma armature. *Review of Scientific Instruments*, 80(8):083506, 2009.

[19] J. W. Mather. Formation of a high-density deuterium plasma focus. *The Physics of Fluids*, 8(2):366–377, 1965.

[20] N. V. Filippov, T. I. Filippova, and V. P. Vinogradov. Dense high-temperature plasma in a non-cylindrical Z-pinch compression. *Nucl. Fusion, Suppl.*, 1962.

[21] M. G. Haines. A review of the dense Z-pinch. *Plasma Physics and Controlled Fusion*, 53(9):093001, 2011.

[22] A. Schmidt, V. Tang, and D. Welch. Fully kinetic simulations of dense plasma focus Z-pinch devices. *Physical Review Letters*, 109(20):205003, 2012.

[23] T. Zhang, R. S. Rawat, S. M. Hassan, J. J. Lin, S. Mahmood, T. L. Tan, S. V. Springham, V. A. Gribkov, P. Lee, and S. Lee. Drive parameter as a design consideration for Mather and Filippov types of plasma focus. *IEEE Transactions on Plasma Science*, 34(5):2356–2362, 2006.

[24] M. A. Mohammadi, S. Sobhanian, C. S. Wong, S. Lee, P. Lee, and R. S. Rawat. The effect of anode shape on neon soft x-ray emissions and current sheath configuration in plasma focus device. *Journal of Physics D: Applied Physics*, 42(4):045203, 2009.

[25] M. Zakaullah, I. Ahmad, A. Omar, G. Murtaza, and M. M. Beg. Effects of anode shape on plasma focus operation with argon. *Plasma Sources Science and Technology*, 5(3):544, 1996.

[26] H. Bhuyan, S. R. Mohanty, N. K. Neog, S. Bujarbarua, and R. K. Rout. Comparative study of soft x-ray emission characteristics in a low energy dense plasma focus device. *Journal of Applied Physics*, 95(6):2975–2981, 2004.

[27] E. Y. Choueiri and J. K. Ziemer. Quasi-steady magnetoplasmadynamic thruster performance database. *Journal of Propulsion and Power*, 17(5):967–976, 2001.

[28] M. Winter, C. Boie, M. Auweter-Kurtz, and L. Kurtz. Experimental and numerical investigation of steady state MPD thrusters. In *European Spacecraft Propulsion Conference*, volume 398, page 431, 1997.

[29] C. M. Xisto, J. C. Páscoa, and P. J. Oliveira. Numerical analysis of real gas MHD flow on two-dimensional self-field MPD thrusters. *Acta Astronautica*, 112:89–101, 2015.

[30] P. C. Sleziona, M. Auweter-Kurtz, and H. O. Schrade. Numerical calculation of a cylindrical MPD thruster. In *Proceeding of International Electric Propulsion Conference, Seattle, USA*, pages 609–617, 1993.

[31] M. R. LaPointe. Numerical simulation of self-field MPD thrusters. In *27th Joint Propulsion Conference*, page 2341, 1991.

[32] U. Shumlak, C. S. Adams, J. M. Blakely, B.-J. Chan, R. P. Golingo, S. D. Knecht, B. A. Nelson, R. J. Oberto, M. R. Sybouts, and G. V. Vogman. Equilibrium, flow shear and stability measurements in the z-pinch. *Nuclear Fusion*, 49(7):075039, 2009.

[33] U. Fantz. Basics of plasma spectroscopy. *Plasma Sources Science and Technology*, 15(4):S137, 2006.

[34] G. V. Vogman and U. Shumlak. Deconvolution of stark broadened spectra for multipoint density measurements in a flow z-pinch. *Review of scientific instruments*, 82(10):103504, 2011.

[35] C. J. Buchenauer and A. R. Jacobson. Quadrature interferometer for plasma density measurements. *Review of Scientific Instruments*, 48(7):769–774, 1977.

[36] J. M. Mitrani, D. P. Higginson, Z. T. Draper, J. Morrell, L. A. Bernstein, E. L. Claveau, C. M. Cooper, E. G. Forbes, R. P. Golingo, B. A. Nelson, et al. Measurements of temporally-and spatially-resolved neutron production in a sheared-flow stabilized Z-pinch. *Nuclear Instruments and Methods in Physics Research Section A: Accelerators, Spectrometers, Detectors and Associated Equipment*, 947:162764, 2019.

[37] J. P. Freidberg. *Ideal MHD*. Cambridge University Press, 2014.

[38] R. W. Moses Jr, R. A. Gerwin, and K. F. Schoenberg. Resistive plasma detachment in nozzle based coaxial thrusters. In *AIP Conference Proceedings*, volume 246, pages 1293–1303. AIP, 1992.

[39] J. M. Little and E. Y. Choueiri. Electron demagnetization in a magnetically expanding plasma. *Physical Review Letters*, 123(14):145001, 2019.

[40] E. Ahedo and M. Merino. Two-dimensional plasma expansion in a magnetic nozzle: Separation due to electron inertia. *Physics of Plasmas*, 19(8):083501, 2012.

[41] D. Biskamp. Magnetic reconnection in plasmas. *Astrophysics and Space Science*, 242(1-2):165–207, 1996.

[42] Y. Zhang, U. Shumlak, B. A. Nelson, R. P. Golingo, T. R. Weber, A. D. Stepanov, E. L. Claveau, E. G. Forbes, Z. T. Draper, J. M. Mitrani, H. S. McLean, K. K. Tummel, D. P. Higginson, and C. M. Cooper. Sustained neutron production from a sheared-flow stabilized Z pinch. *Phys. Rev. Lett.*, 122:135001, Apr 2019.

[43] D. J. Den Hartog and R. P. Golingo. Telecentric viewing system for light collection from a Z-pinch plasma. *Review of Scientific Instruments*, 72(4):2224–2225, 2001.

[44] L. Spitzer. *Physics of Fully Ionized Gases*. Courier Corporation, 2006.

[45] P. G. Carolan and V. A. Piotrowicz. The behaviour of impurities out of coronal equilibrium. *Plasma Physics*, 25(10):1065, 1983.

[46] L. J. Dursi and C. Pfrommer. Draping of cluster magnetic fields over bullets and bubbles—morphology and dynamic effects. *The Astrophysical Journal*, 677(2):993, 2008.

[47] G. C. Burdiak, S. V. Lebedev, S. N. Bland, T. Clayson, J. Hare, L. Suttle, F. Suzuki-Vidal, D. C. Garcia, J. P. Chittenden, S. Bott-Suzuki, et al. The structure of bow

shocks formed by the interaction of pulsed-power driven magnetised plasma flows with conducting obstacles. *Physics of Plasmas*, 24(7):072713, 2017.

[48] D. Y. Cheng. Plasma deflagration and the properties of a coaxial plasma deflagration gun. *Nuclear Fusion*, 10(3):305, 1970.

[49] K. T. K. Loebner, T. C. Underwood, and M. A. Cappelli. Evidence of branching phenomena in current-driven ionization waves. *Physical Review Letters*, 115(17):175001, 2015.

[50] C. T. Chang. Shock wave phenomena in coaxial plasma guns. *The Physics of Fluids*, 4(9):1085–1096, 1961.

[51] D. Burgess. Collisionless shocks. *Introduction to Space Physics*, pages 129–163, 1995.

[52] R. G. Stone and B. T. Tsurutani. Collisionless shocks in the heliosphere: A tutorial review. 1985.

[53] A. L. Velikovich and M. A. Liberman. The structure of a transverse shock wave in a plasma. *Zhurnal Eksperimental'noi i Teoreticheskoi Fiziki*, 71:1390–1411, 1976.

[54] S. I. Braginskii and M. A. Leontovich. Reviews of plasma physics, 1965.

[55] W. M. Nevins. Feasibility of a colliding beam fusion reactor. *Science*, 281(5375):307–307, 1998.

[56] U. Shumlak. Z-pinch fusion. *Journal of Applied Physics*, 127(20):200901, 2020.

[57] H.-S. Bosch and G. M. Hale. Improved formulas for fusion cross-sections and thermal reactivities. *Nuclear Fusion*, 32(4):611, 1992.

[58] K. Linnet. Evaluation of regression procedures for methods comparison studies. *Clinical chemistry*, 39(3):424–432, 1993.

[59] D. M. Woodall and L. K. Len. Observation of current sheath transition from snowplow to deflagration. *Journal of Applied Physics*, 57(3):961–964, 1985.

[60] R. Myers, M. Lapointe, and M. Mantenieks. MPD thruster technology. In *Conference on Advanced SEI Technologies*, page 3568, 1991.

[61] J. T. Cassibry, Y. C. Thio, and S. T. Wu. Two-dimensional axisymmetric magneto-hydrodynamic analysis of blow-by in a coaxial plasma accelerator. *Physics of plasmas*, 13(5):053101, 2006.

[62] J. H. Hammer, J. L. Eddleman, C. W. Hartman, H. S. McLean, and A. W. Molvik. Experimental demonstration of compact torus compression and acceleration. *Physics of Fluids B: Plasma Physics*, 3(8):2236–2240, 1991.

[63] K. L. Baker, R. D. Horton, D. Q. Hwang, R. W. Evans, and S. Howard. Simulation of the "blowby" effect in an accelerating compact toroid. *IEEE Transactions on Plasma Science*, 30(1):48–49, 2002.

Appendix A

PLASMA PARAMETERS FROM NEUTRON YIELD

Plasma radius a and plasma density profiles $n(r)$ are challenging to accurately measure in the FuZE device. However, pinch current I, neutron yield Y, and ion temperature T_i are more reliably obtained. The pinch current is obtained from inductive probes and can be resolved both spatially, every 5 cm, and temporally at the digitization frequency. The yield is obtained from the counts measured on the neutron scintillators and is resolved temporally, but not spatially. Finally, ion temperature is obtained at one point in time from the Doppler broadening of an impurity line, usually CIII or CV. It is resolved spatially only in the transverse direction to the pinch. This appendix describes a method using force balance and the thermonuclear yield equation to calculate a pinch radius and density profile using the measured current, yield, and ion temperature.

One of the limitations of this approach comes from linking the nonlocal measurement of neutron yield with the local measurement of temperature. As such, the approach assumes a uniform axial distribution of plasma parameters.

The first assumption in the analysis will be that the magnetic field follows a Bennett profile given by

$$B(r) = \frac{\mu_0 I}{2\pi} \frac{r}{r^2 + a^2} \tag{A.1}$$

where I is the total pinch current and a is the plasma radius.

Then, using the radial force balance for a Z pinch, a relationship between the pinch current and the plasma pressure is obtained. The plasma pressure is assumed to have the following form:

$$P(r) = n_e(r) k_B T_e(r) + n_e(r) k_B T_i(r) \tag{A.2}$$

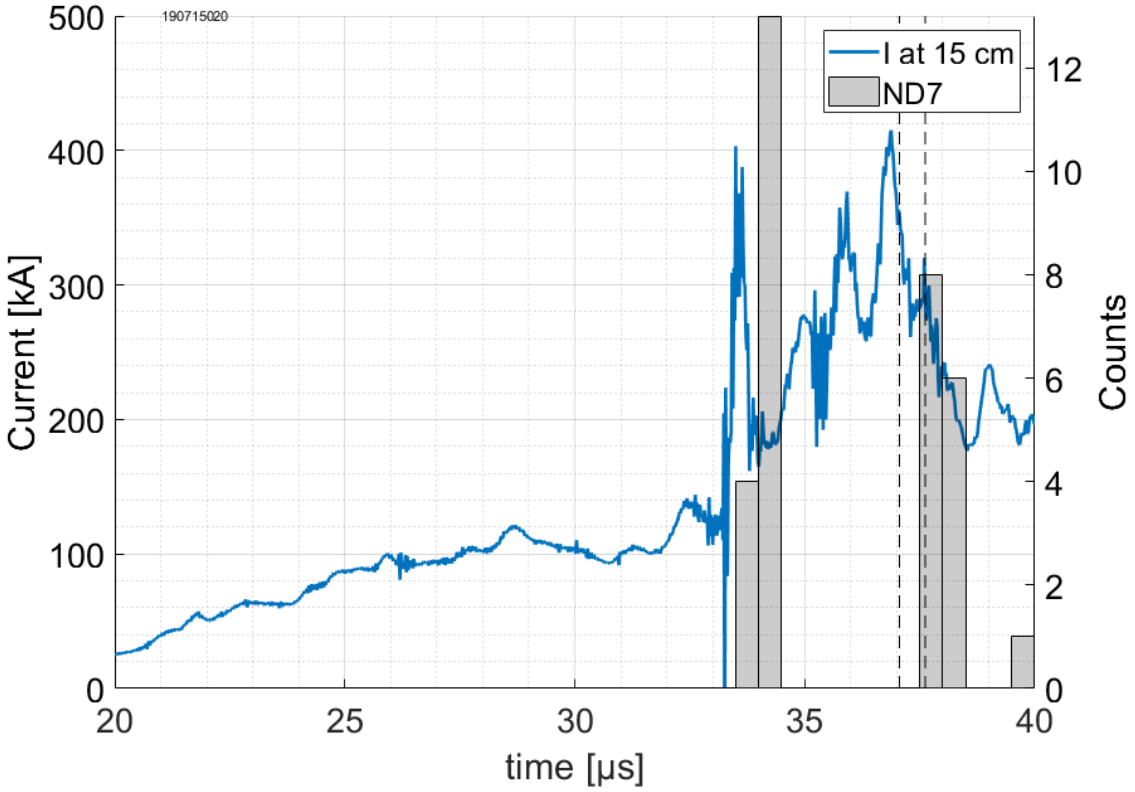

Figure A.1: Pinch current at $z = 15$ cm for one pulse and corresponding neutron counts on detector 7 (ND7) placed 2.2 m away from the Z-pinch axis binned over 0.5 µs. The ICCD exposure of the data presented in Fig. A.2 and Fig. A.3 is shown by the vertical dashed lines.

For a hydrogen or deuterium plasma with $T_i = T_e$, Eq. (A.2) becomes

$$P(r) = 2n(r)k_B T_i(r) \tag{A.3}$$

Finally, the equation for thermonuclear yield is employed

$$Y = \frac{l\tau}{2} \int_0^{R_{wall}} n_D^2(r) \langle \sigma v \rangle \, 2\pi r dr \tag{A.4}$$

Where n_D is the deuterium density, $\langle \sigma v \rangle$ is the thermonuclear fusion cross section obtained from Bosh-Hale[57], l is the emission length, and τ is the emission time. An example of calculated profiles is shown in Fig. A.4.

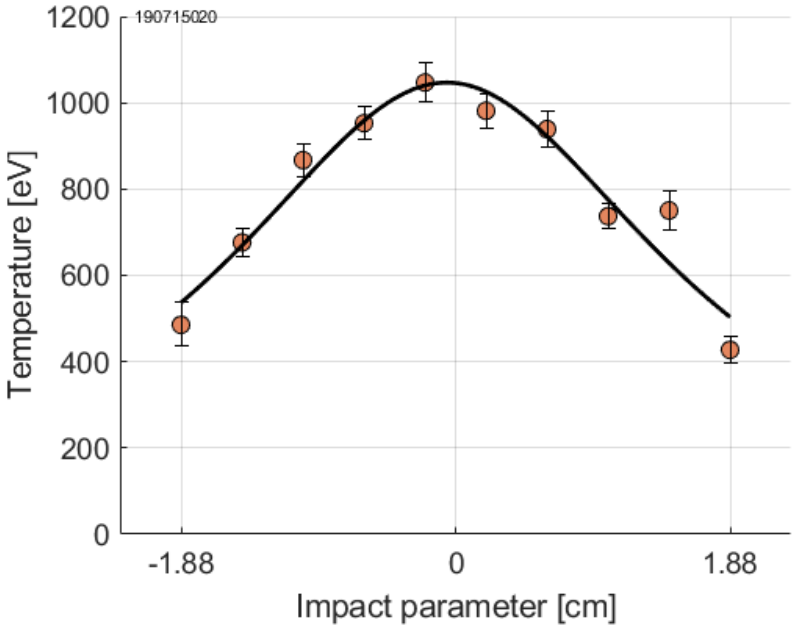

Figure A.2: Measured CV temperature from Doppler broadening for a telescope oriented at 90° to the plasma. The error bars are obtained from a 95% confidence interval of the Gaussian fitting algorithm. A Lorentzian is fit (overlaid black line) to the 10 chords and a radius $a = 2.0 \pm 0.2$ cm is obtained.

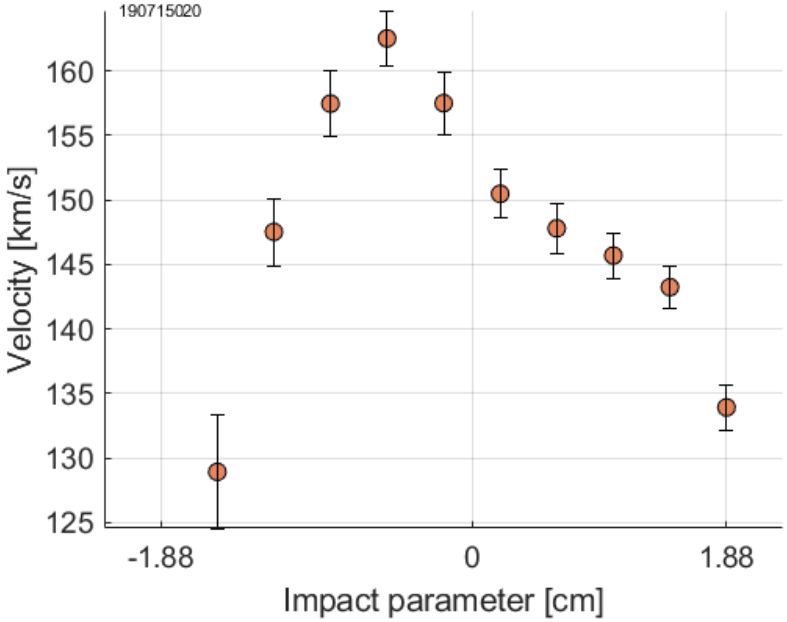

Figure A.3: Velocity profile from the Doppler shift of CV impurity obtained from a telescope oriented at 45° relative to the flow. The telescope images the same time and location of the same plasma pulse as Fig. A.2. The profile shows a peaked sheared velocity profile.

Figure A.4 shows calculated density n, magnetic field B, ion temperature T_i, and yield integrand for a 6 kV pulse with a 300 kA current and a 1 keV peak temperature obtained from Fig. A.1 and Fig. A.2 with $Y = 7 \times 10^4$, which corresponds to one count on ND7.

The neutrons emitted from the measured axial location have to be much lower to obtain an equilibrium radius equivalent to the radius of Fig. A.2. A yield of 3×10^3 is used to obtain a similar plasma radius as the recorded radius from the temperature measurement. This yield is below the detection level of ND7. The current at $z = 15$ cm is shown to decrease as 8 counts are recorded on ND7 just after the ICCD exposure. The measured radius and the calculated equilibrium conditions show that the neutrons are likely coming from another axial location in the Z pinch as the current is shown to decrease from a state where the calculated plasma profile would have emitted neutrons below the detection level. Therefore, the neutron emission in this plasma pulse is likely not axially uniform.

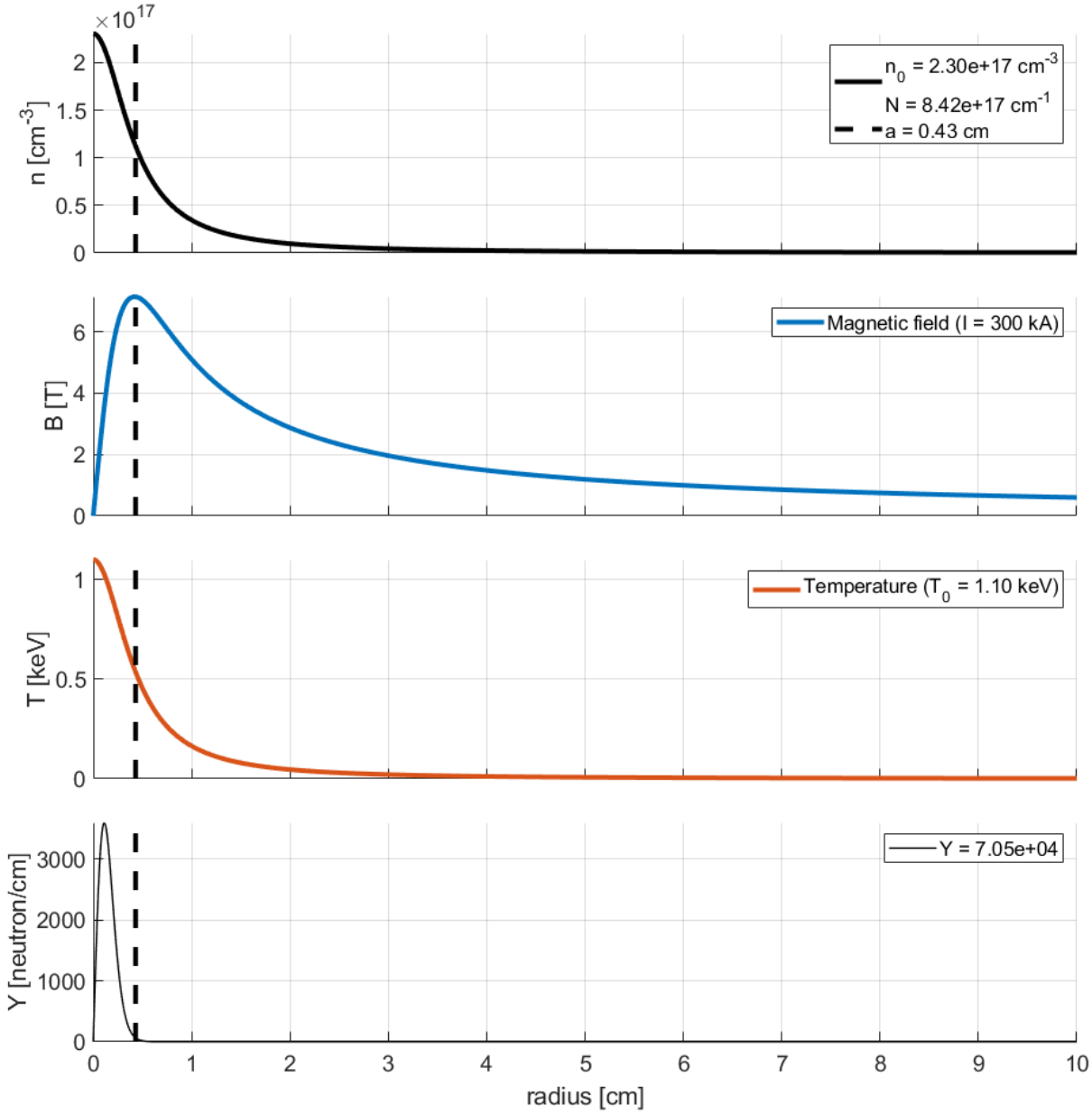

Figure A.4: Calculated density n, magnetic field B, temperature T_i, and yield integrand for a 6 kV pulse with a 300 kA current and a 1 keV peak temperature obtained from Fig. A.1 and Fig. A.2 with $Y = 7 \times 10^4$, which corresponds to one count on ND7. The yield coming from the measured axial location has to be much lower to obtain an equilibrium radius equivalent to the radius of Fig. A.2.

Appendix B

NOSE CONE GEOMETRY CHANGE

The nose cone was changed from a tapered design to a flat design to investigate the geometry effect on the Z-pinch behavior. This appendix analyzes the effect on the neutron production, the average pinch current, and the gap voltage. Then, the radial currents near the nose cone are shown along the axial velocity. The plasma radius from the light emission is shown for the location close to the nose cone. Finally, temperature and velocity data are shown for both nose cones. It is found that the gap voltage does not change drastically with the geometry change, but the neutron yield is reduced for the flat nose cone while its average pinch current increases compared to the tapered nose cone. Radial currents near the nose cone are enhanced for the flat nose cone and correspondingly lower axial velocities are found. Finally, a smaller characteristic light emission radius is found near the flat nose cone compared to the tapered nose cone.

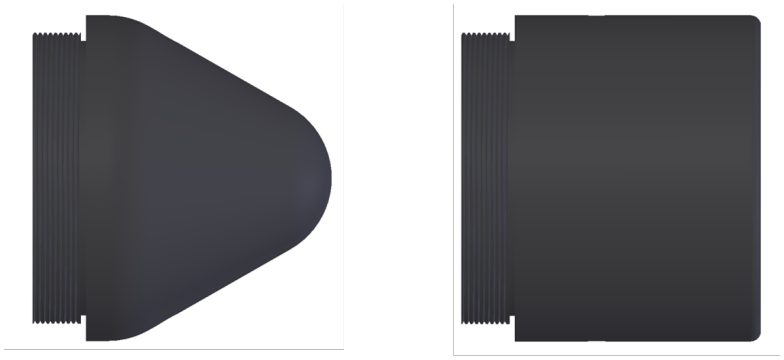

Figure B.1: Tapered nose cone (a) and flat nose cone (b) designs.

B.1 Neutron, average current, and gap voltage

The neutron emission and average pinch current are compared between the two geometries in Fig. B.2. The total yield is higher for the tapered nose cone pulses. The neutrons start being emitted earlier and are peaked toward the peak current at around 41 µs. The average current for the flat nose cone is higher. The higher currents are mainly concentrated near the nose cone, as shown in Fig. B.4. Figure B.3 shows that the measured gap voltage is similar between the two configurations.

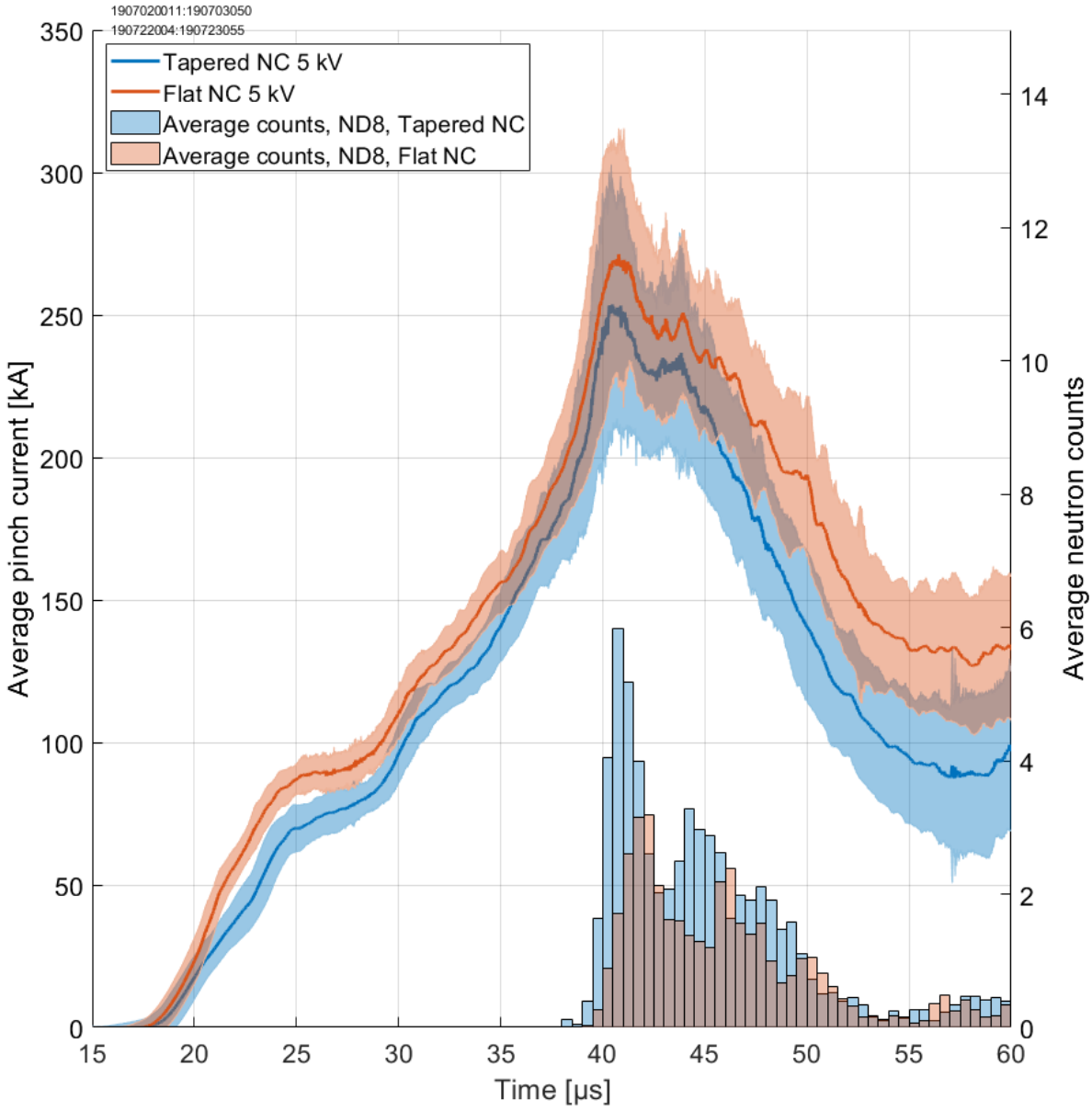

Figure B.2: Average current and average neutron counts for the tapered (blue) and flat (red) nose cones. The current is the average between $z = 0$ cm and $z = 30$ cm. The average current is higher for the flat nose cone, but the yield is higher for the tapered nose cone.

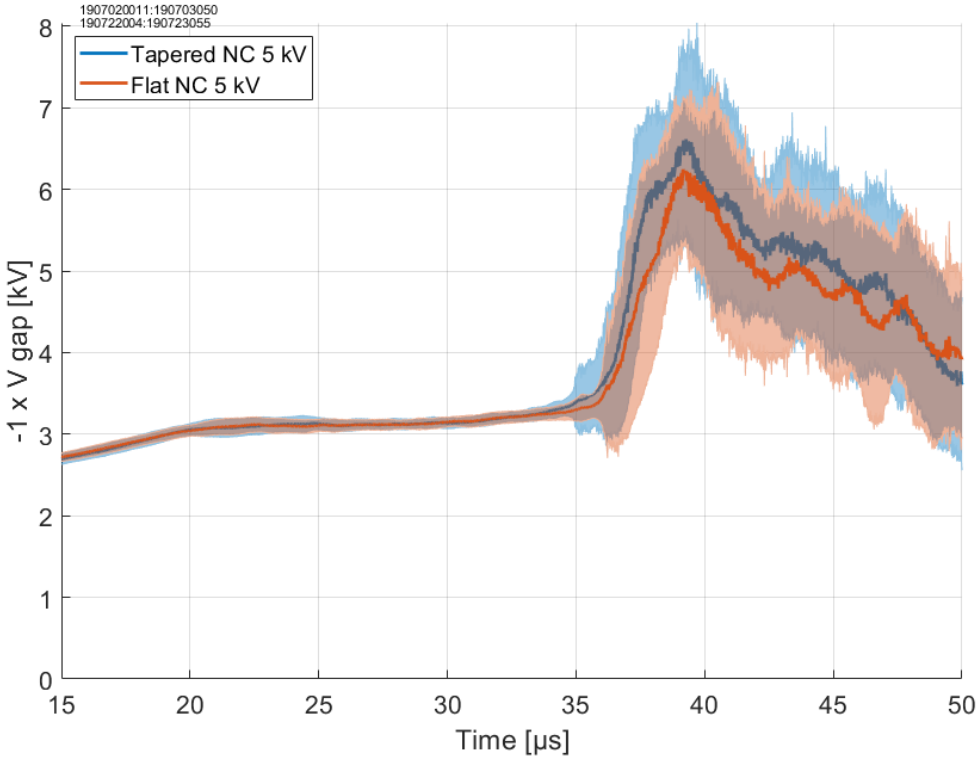

Figure B.3: Gap voltage for the tapered (blue) and flat (red) nose cones. The two measured gap voltages fall within their error bar region.

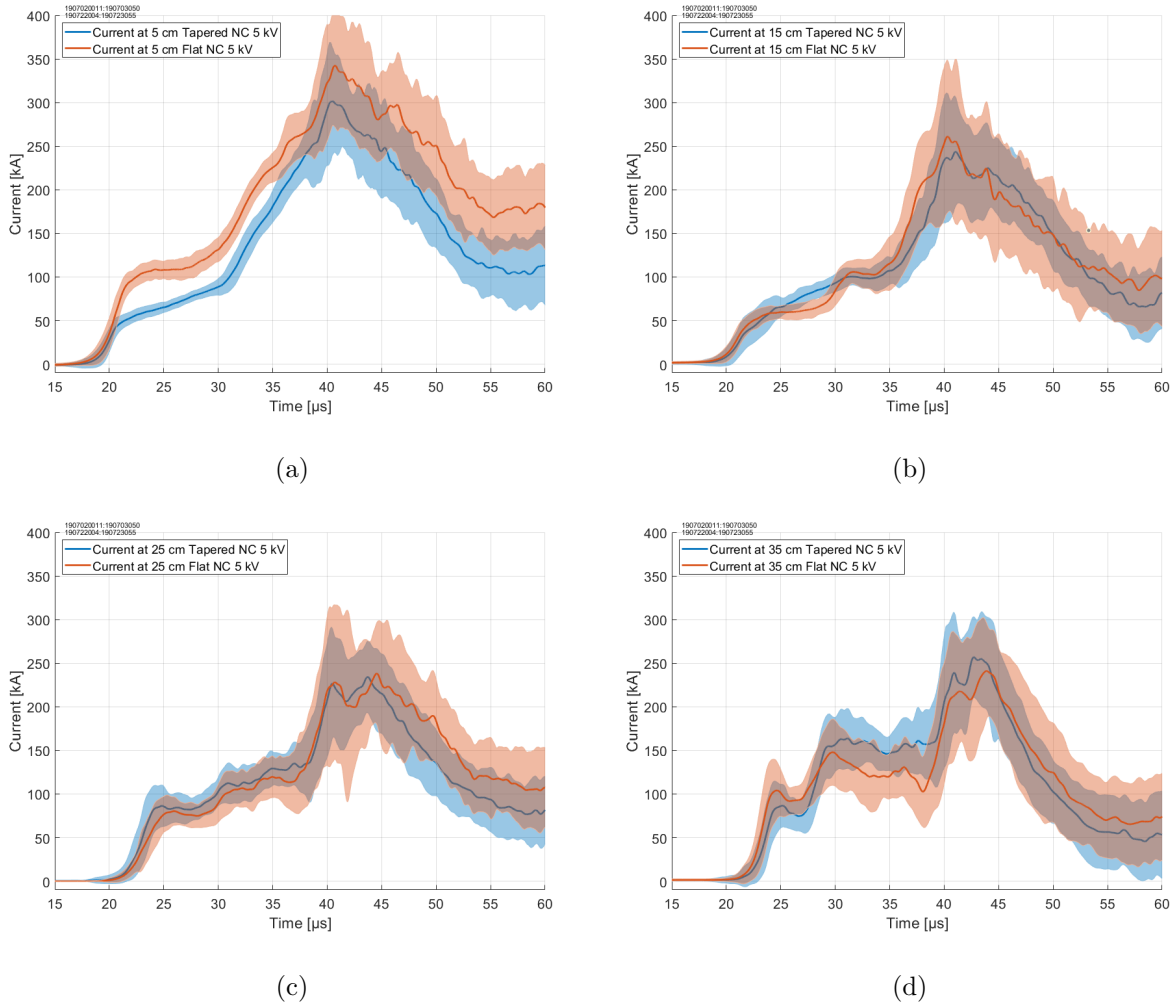

Figure B.4: Pinch axial current at (a) 5 cm, (b) 15 cm, (c) 25 cm, and (d) 35 cm. The increase in average pinch current for the flat geometry is mainly accounted for by the currents located upstream of 15 cm.

B.2 Radial current enhancement in the assembly region

Figure B.5 and Fig. B.6 show the total pinch current at $z = -5$, 5, and 15 cm. The tapered nose cone data set is shown in B.5 and the flat nose cone data set is shown in B.6. Because current is conserved, a difference in axial pinch current between two locations has to be accounted for by the presence of radial currents. The largest difference can be observed between the 5 and 15 cm locations. For the tapered nose cone conditions, the currents at 5 and 15 cm are almost identical for the period between 22 and 33 µs, showing that no radial current flows between those two locations. A difference of about 50 kA is observed between those two same locations for the flat nose cone.

The presence of radial current downstream of the nose cone means that plasma is still accelerated axially after exiting the acceleration region. This is indeed observed in the spectroscopy data presented in Fig. B.7 and Fig. B.8.

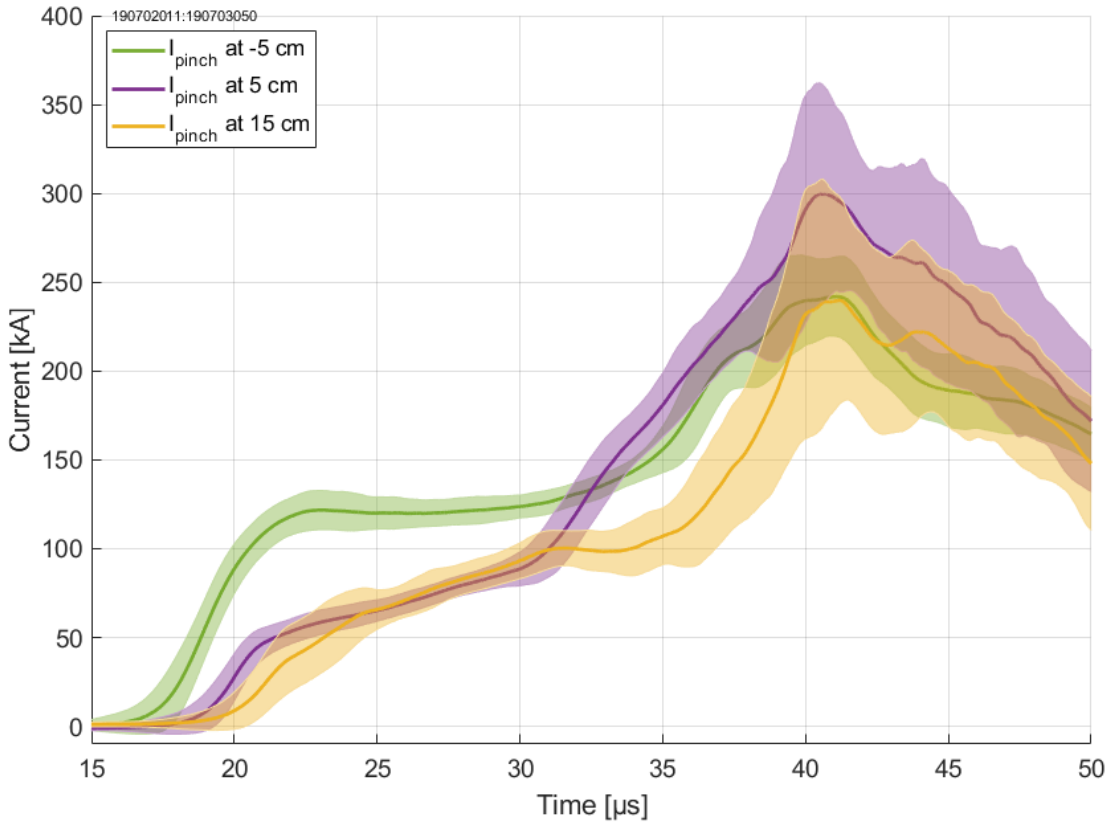

Figure B.5: Mean (line) and standard deviation (shaded area) of axial pinch current at -5 cm (green), 5 cm (purple), and 15 cm (yellow) from the tip of the tapered nose cone. The difference in axial current between the locations is accounted for by the presence of radial currents.

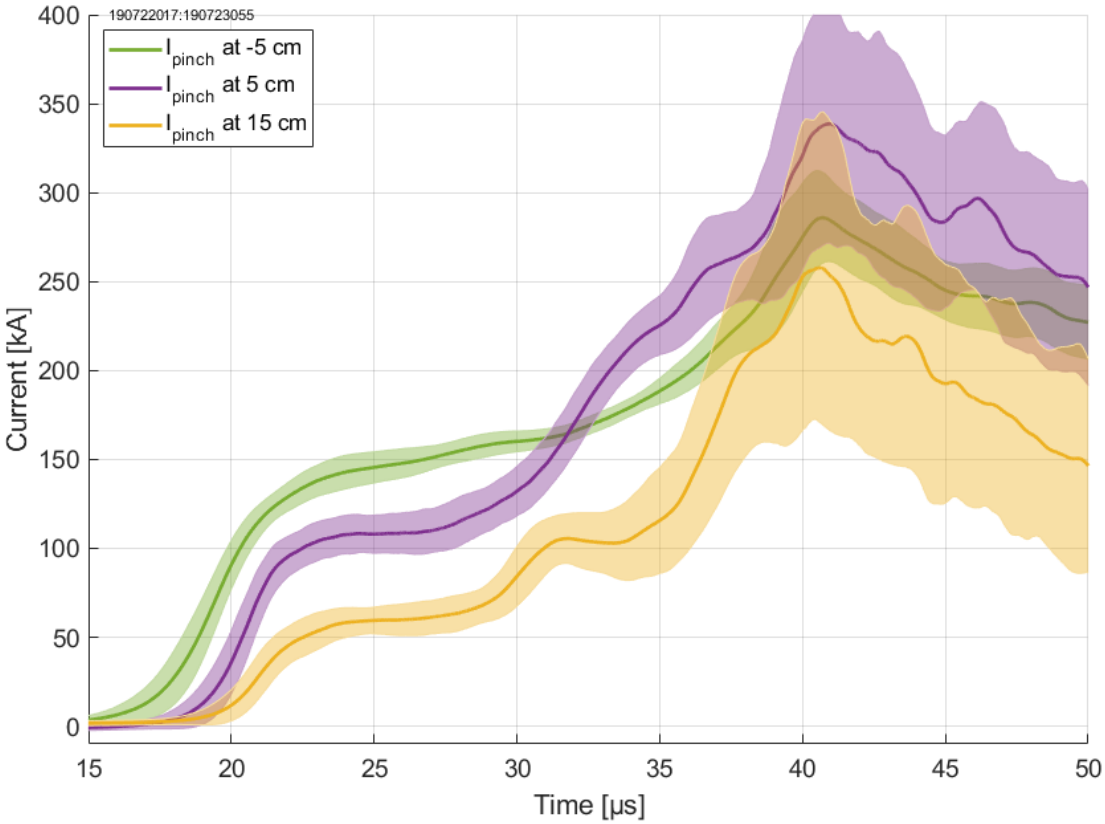

Figure B.6: Mean (line) and standard deviation (shaded area) of axial pinch current at -5 cm (green), 5 cm (purple), and 15 cm (yellow) from the tip of the flat nose cone. The difference in axial current between the locations is accounted for by the presence of radial currents.

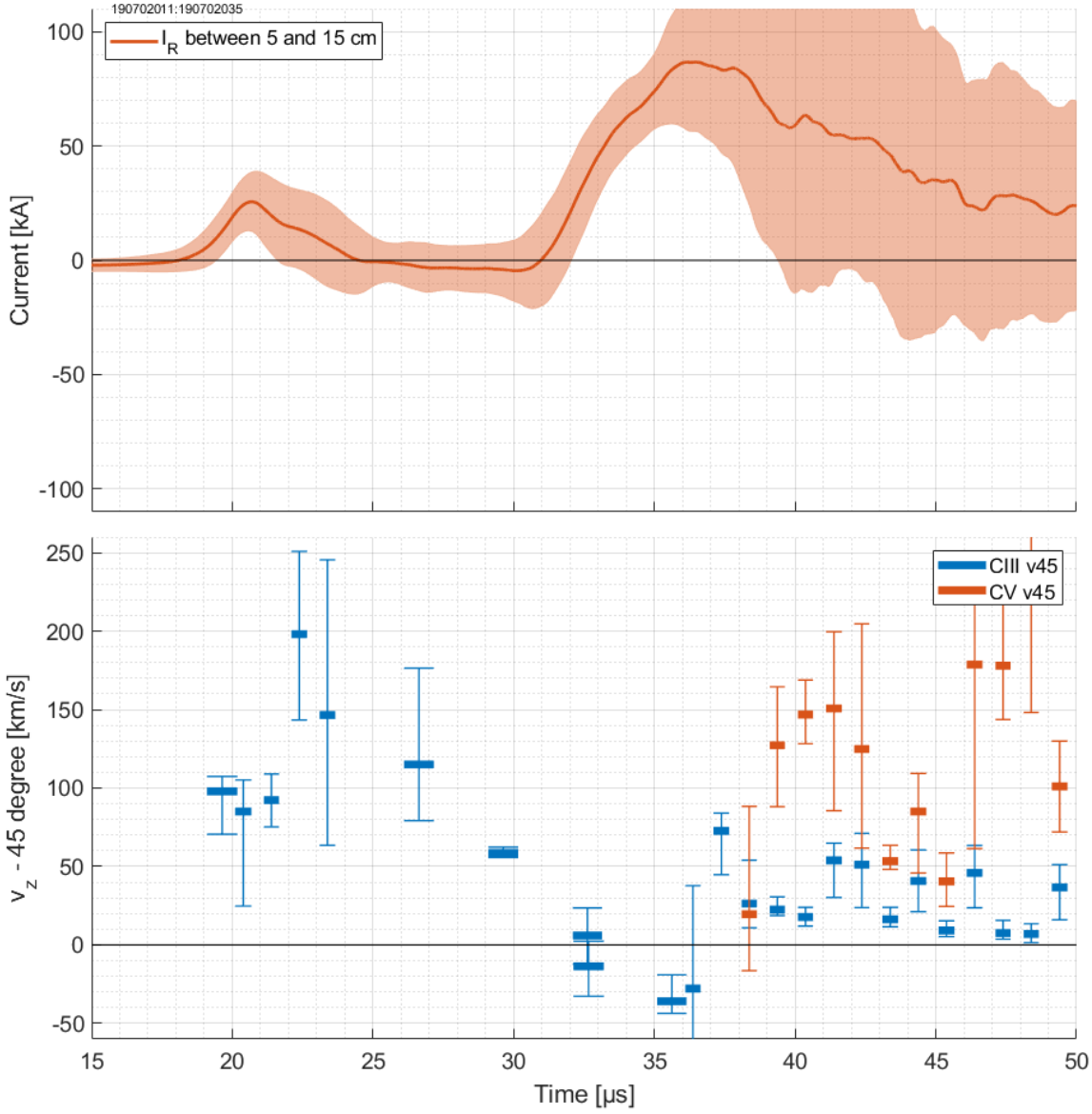

Figure B.7: Radial current between 5 and 15 cm of the tip of the tapered nose cone with axial velocity recorded at 7.1 cm downstream of the nose cone. The CIII velocity is the highest when the radial current is small.

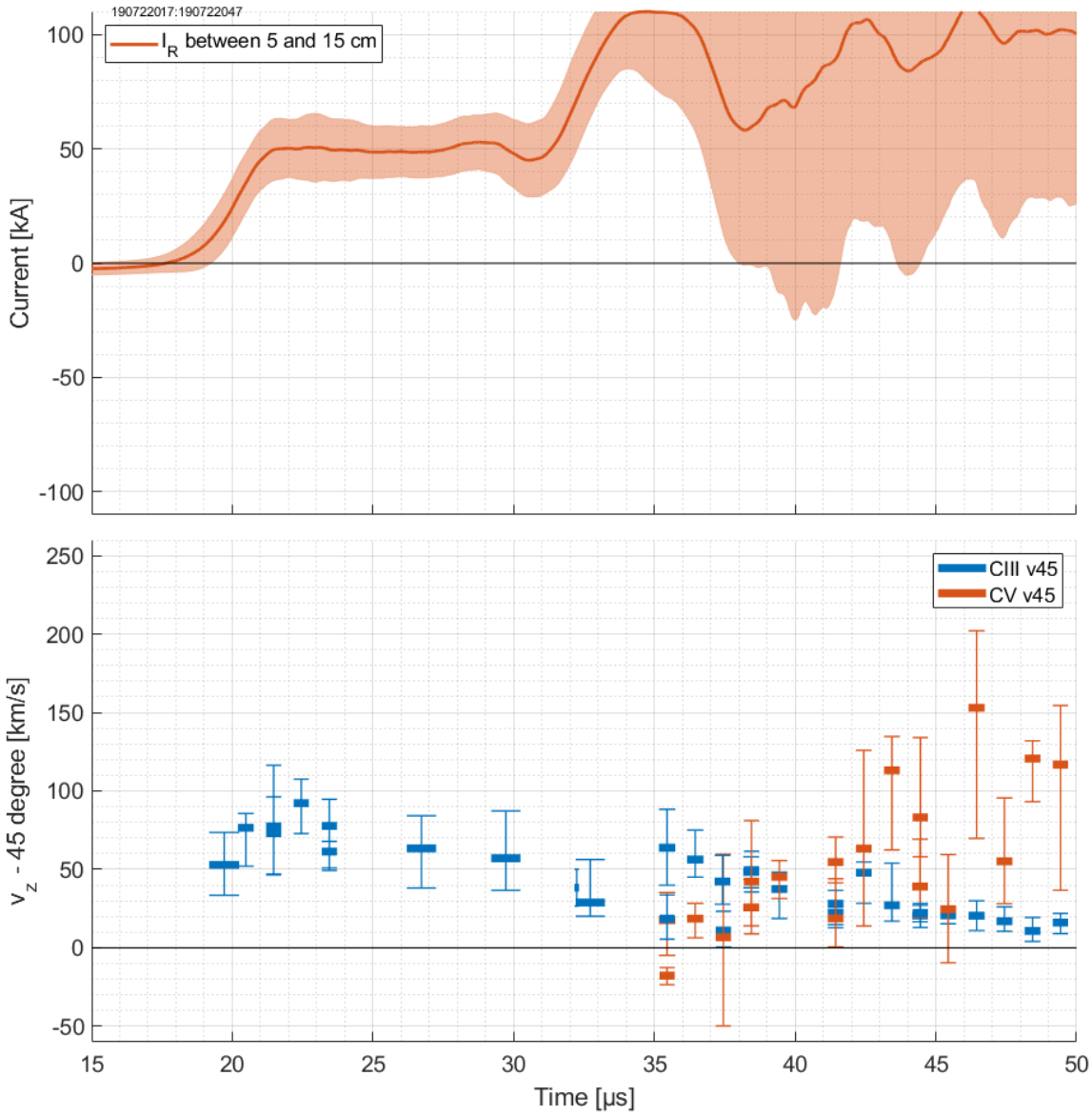

Figure B.8: Radial current between 5 and 15 cm of the tip of the flat nose cone with axial velocity recorded at 7.1 cm downstream of the nose cone. The average radial current never reaches a null value.

B.3 Collimated light emission near the nose cone

The light intensity profile is obtained by summing all the light recorded over a window encompassing the CIII or the CV line. Each profile is obtained independently for the CIII and the CV line. Assuming an optically thin plasma and a uniform emissivity, the light intensity is proportional to the plasma density. Therefore, the presence of a structure in the emitted light suggests the presence of a structure in the plasma density.

In particular, peaked profiles are evidence of centered and concentrated plasma on axis. A fitting algorithm calculates the best Lorentzian fit for the measured light emission profile. An example of the calculated fits is shown in Fig. B.9. The calculated radius is only displayed for the CIII fits because the profile as a peak located within the chord span of 3.76 cm. The CV signal does not display a peaked structure and is therefore assumed to be either a flat emission profile or peaked outside the chord field of view with a finite, but unknown, radius.

Each plasma pulse has the fitting routine shown in Fig. B.9 performed and the calculated radius is extracted. Only the profiles peaked within the chord span are recorded. The calculated radii for the 90-degree and 45-degree telescopes over 3 axial positions are summarized in Fig. B.10 for the tapered nose cone pulses and in Fig. B.11 for the flat nose cone.

There is an increase in the number of peaked and centered profiles calculated from the CIII emissions for the flat nose cone at $z = 5$ cm. This indicates a smaller pinch radius just downstream of the nose cone and could be related to the increase in radial currents described in the previous section.

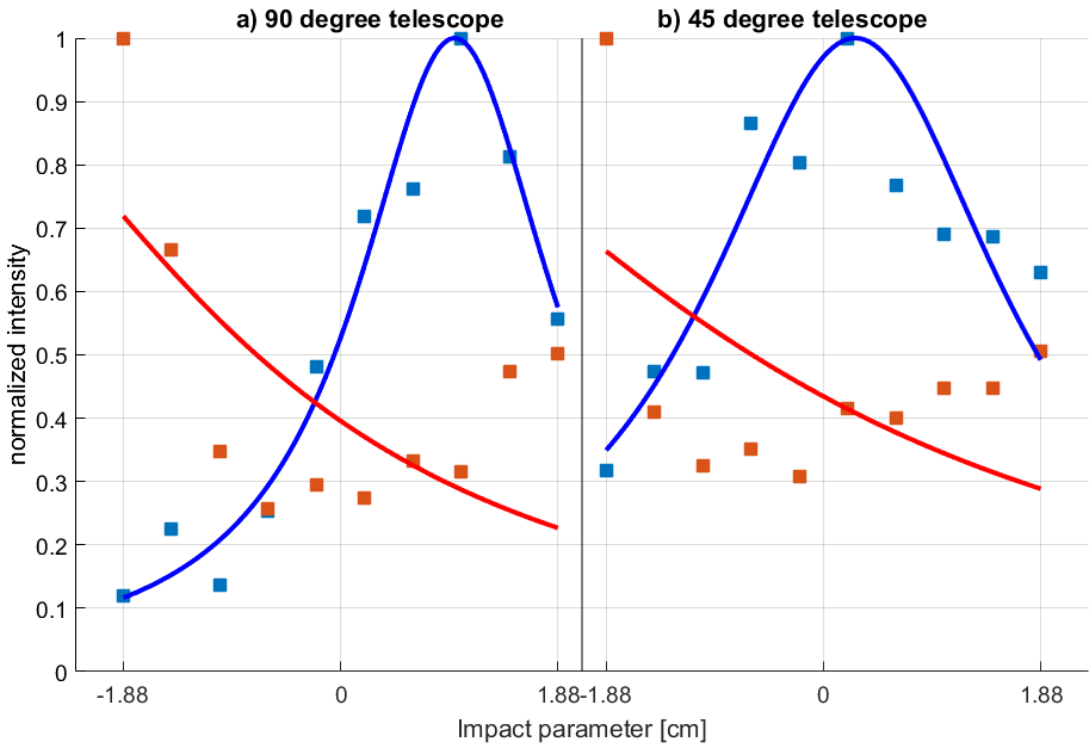

Figure B.9: Light emission from the 90-degree (a) and the 45-degree (b) telescopes. The light from CIII is shown in blue and the light from the CV lines is shown in red. Only the CIII signal would be used for the radius data of Fig. B.11 and B.10, as its Lorentzian function has a peak located within the chord span of 3.76 cm.

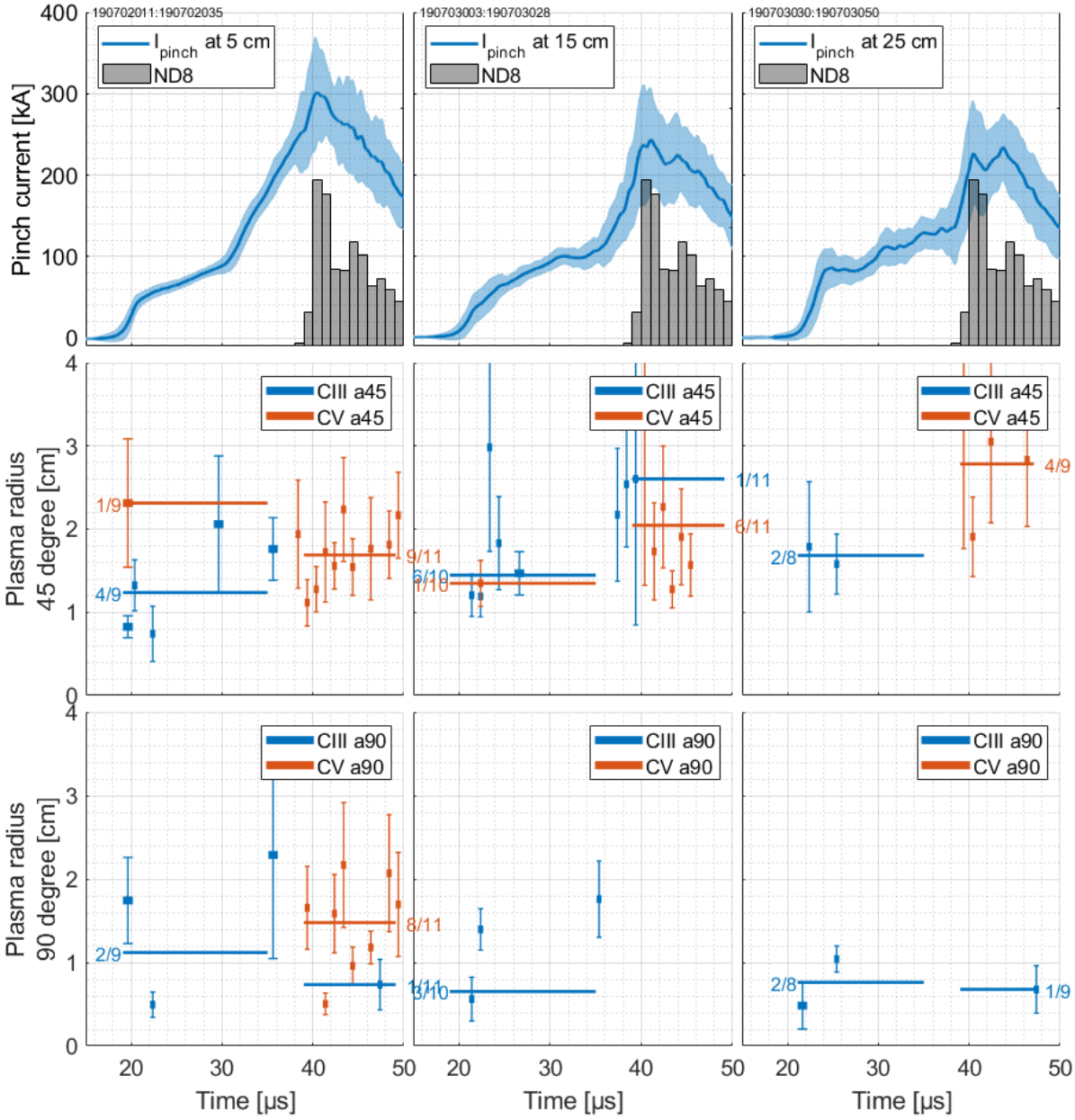

Figure B.10: Tapered nose cone plasma radii calculated from the light intensity at 5, 15 and 25 cm downstream of the nose cone for the 45 and 90-degree telescopes. The CIII data are represented in blue and the CV data are represented in red. Only the fitted profiles with a center within the telescope field of view are presented. The horizontal bars are the average radius while the fractional numbers next to the bars represent the number of centered fits over the total number of recorded profiles.

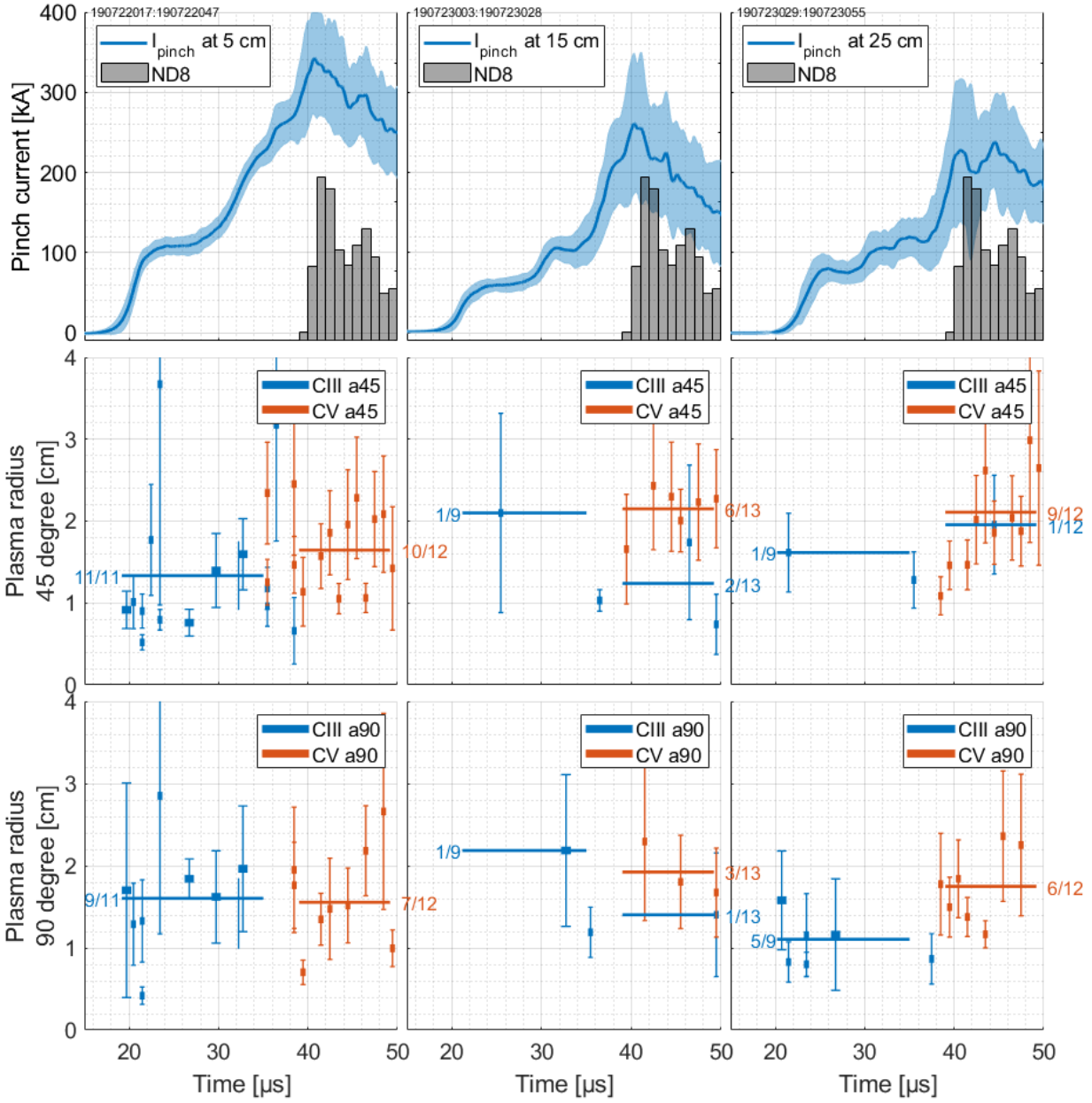

Figure B.11: Flat nose cone plasma radii calculated from the light intensity at 5, 15 and 25 cm downstream of the nose cone for the 45 and 90-degree telescopes. The CIII data are represented in blue and the CV data are represented in red. Only the fitted profiles with a center within the telescope field of view are presented. The horizontal bars are the average radius while the fractional numbers next to the bars represent the number of centered fits over the total number of recorded profiles.

B.4 Velocity and temperature measurements for the tapered and flat nose cones

This section shows the complete set of velocity and temperature measurements recorded for the nose cone investigation. For each pulse, a temperature and velocity profile are recorded for the 90-degree and 45-degree telescopes at one point in time. The average current at each telescope location is shown in the first row with the corresponding normalized neutron count in 1 µs bins. The second row shows the plasma properties calculated from the 45-degree telescope and the last row shows the same properties from the 90-degree telescope. The width of the data points in the second and third rows correspond to the ICCD exposure. The vertical error bars represent the total range of the property calculated over the 10 chords of each telescope. All properties calculated from the CIII emissions are indicated in blue while all properties from the CV emission are shown in red.

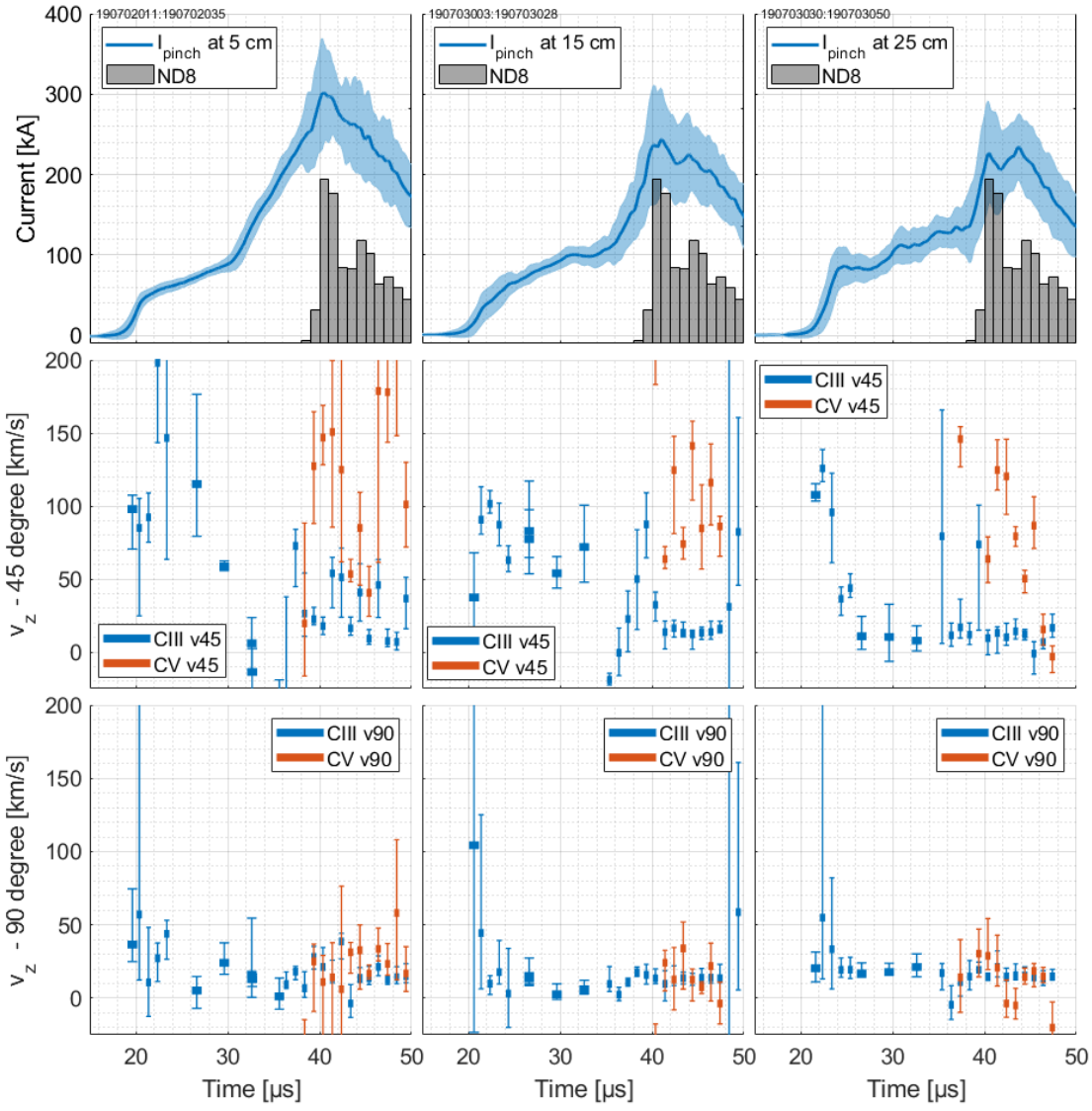

Figure B.12: Tapered nose cone plasma axial velocity at 5, 15 and 25 cm downstream of the nose cone for the 45 and 90-degree telescopes. The CIII data are represented in blue and the CV data are represented in red.

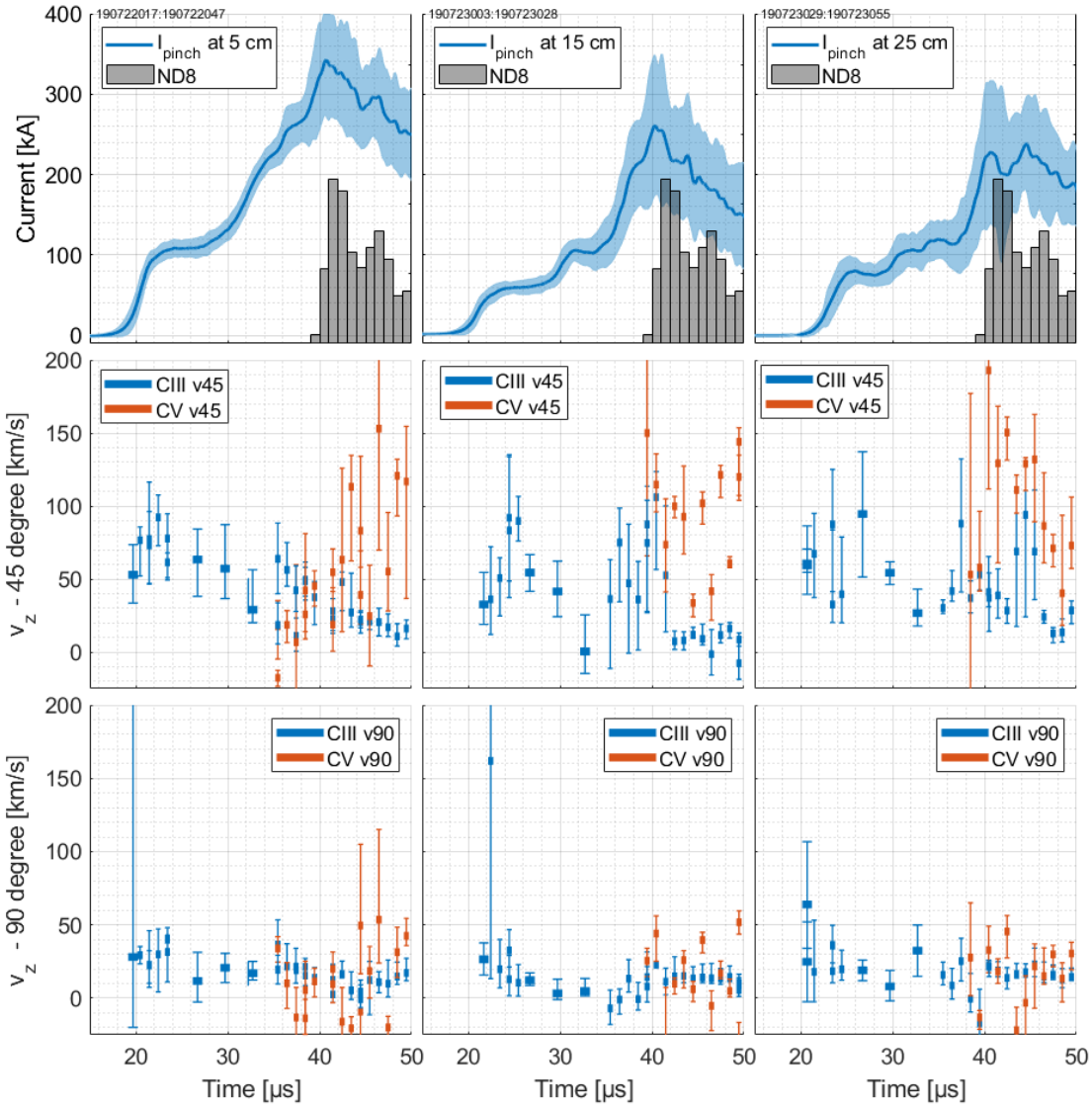

Figure B.13: Flat nose cone plasma axial velocity at 5, 15 and 25 cm downstream of the nose cone for the 45 and 90-degree telescopes. The CIII data are represented in blue and the CV data are represented in red.

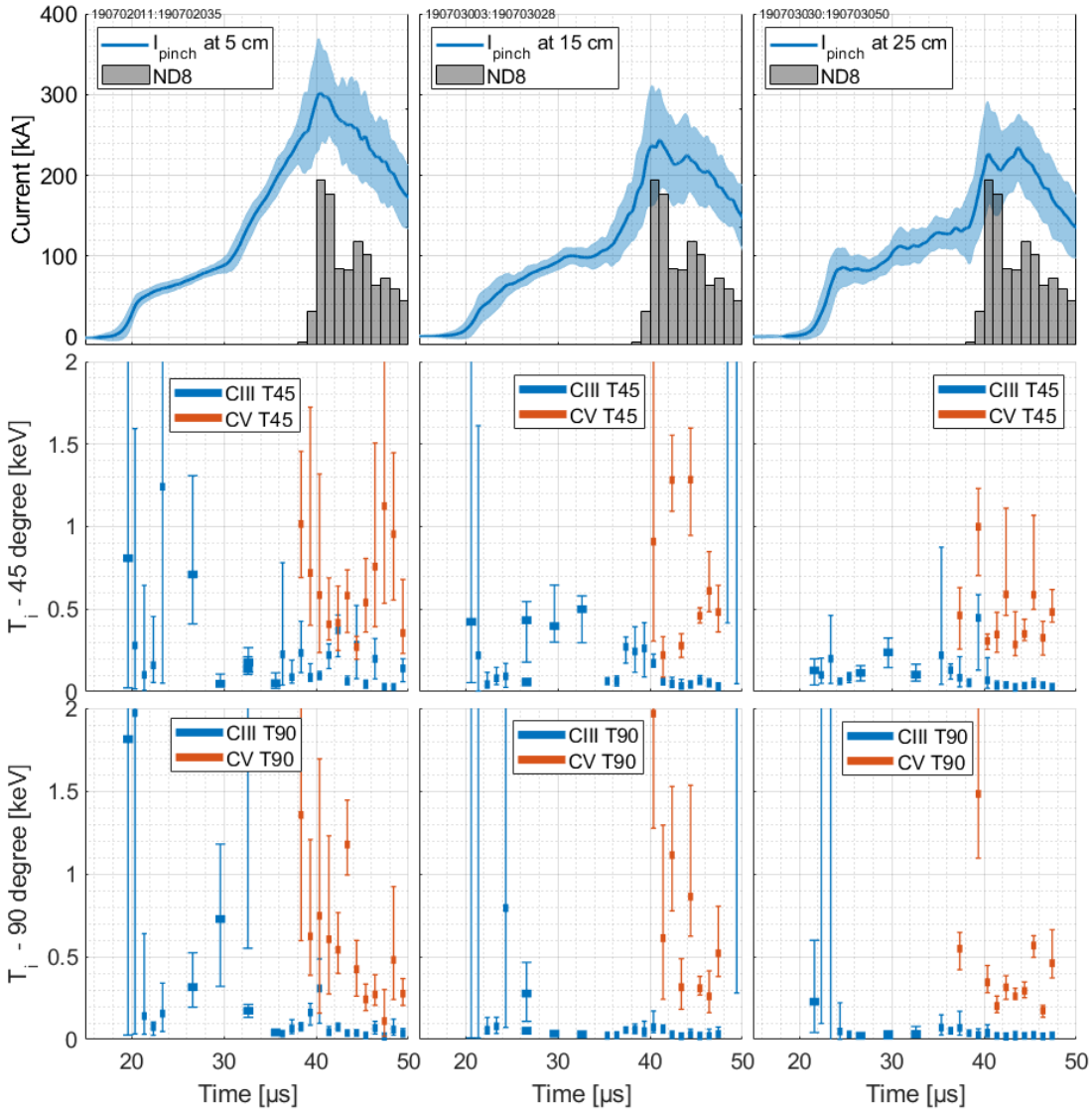

Figure B.14: Tapered nose cone plasma temperature at 5, 15 and 25 cm downstream of the nose cone for the 45 and 90-degree telescopes. The CIII data are represented in blue and the CV data are represented in red.

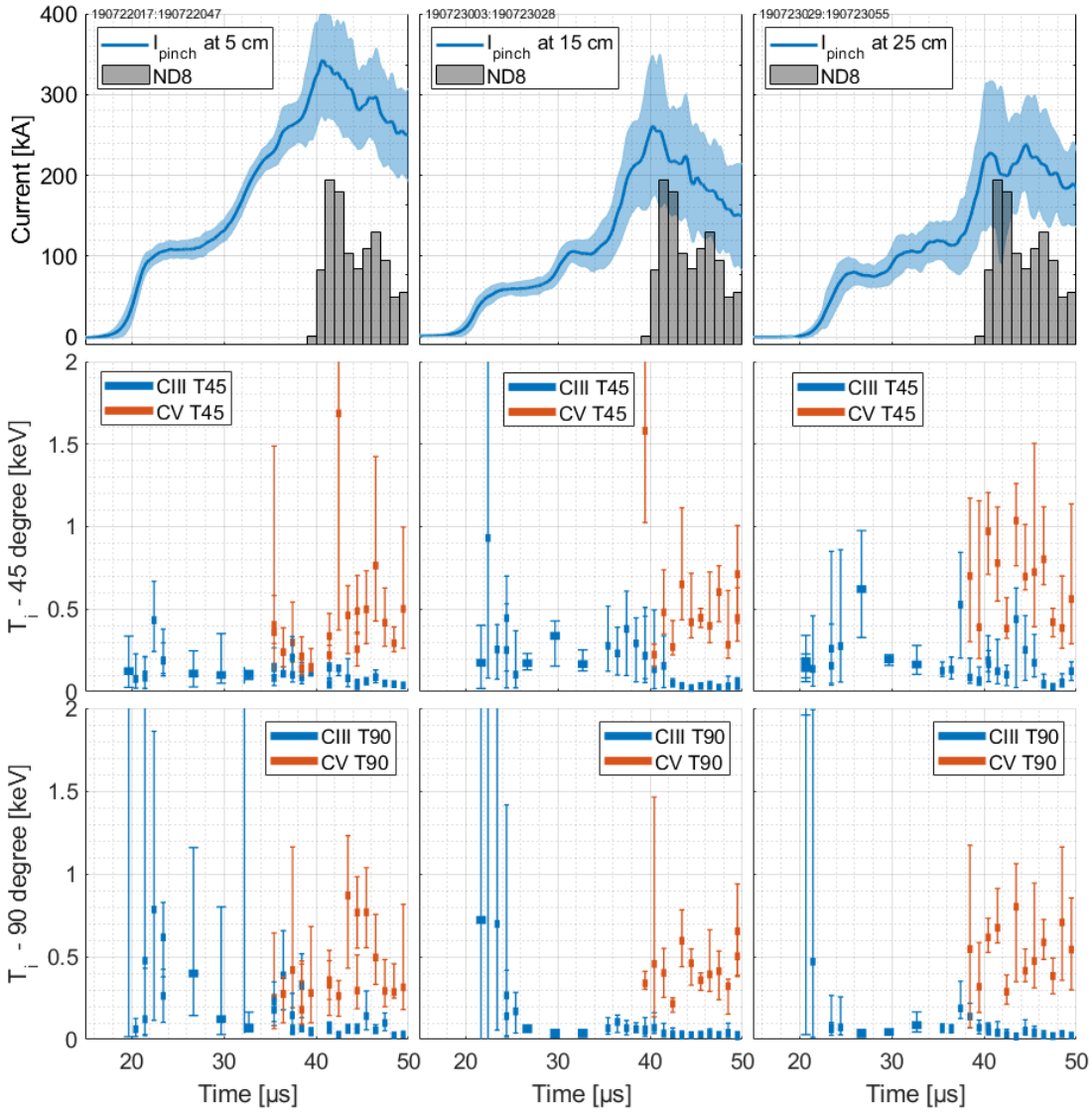

Figure B.15: Flat nose cone plasma temperature at 5, 15 and 25 cm downstream of the nose cone for the 45 and 90-degree telescopes. The CIII data are represented in blue and the CV data are represented in red.